Near-surface Characterization via Seismic Surface-wave Inversion

---

A Dissertation Presented to

the Department of Earth and Atmospheric Sciences

University of Houston

In Partial Fulfillment

of the Requirements for the Degree

Doctor of Philosophy

By

Soumya Roy

August 2013

Near-surface Characterization via Seismic Surface-wave Inversion

Soumya Roy

APPROVED:

Dr. Robert R. Stewart, Chairman
Department of Earth and Atmospheric Sciences

Dr. Aibing Li, Committee Member
Department of Earth and Atmospheric Sciences

Dr. Hua-Wei Zhou, Committee Member
Department of Earth and Atmospheric Sciences

Dr. Chris Krohn, Committee Member
ExxonMobil Upstream Research

Dean, College of Natural Sciences and Mathematics

ACKNOWLEDGEMENTS

There is a long list of people whose unconditional support made this dissertation possible. First and foremost, I am grateful to my advisor Dr. Robert R. Stewart for providing me with the opportunity to be a part of the Allied Geophysical Laboratories (AGL). Dr. Stewart has generously supported me with the financial and intellectual aids throughout last 4 years. Dr. Stewart's insightful and innovative technical advice and amiable nature made this journey an enjoyable learning experience. Apart from his geoscientific expertise, I learned a lot from him related to ethical, behavioral, and professional approaches which will be an asset for my future endeavors. I would like to thank my committee members – Dr. Aibing Li, Dr. Hua-Wei Zhou, and Dr. Chris Krohn for their valuable suggestions throughout this process which helped me immensely to arrange my dissertation work in a meaningful way. I also like to thank Dr. C. Liner for his SEG distinguished lecture and insightful tips related to my dissertation work. Thanks to faculty at the Department of Earth and Atmospheric Sciences for their admirable teaching expertise.

I thank my colleagues and friends from AGL (especially Mr. Bode Omoboya, Mr. Li Chang, Mr. Anoop William, Mr. Eray Kocel, and Dr. Nikolay Dyaur) for their assistance in acquiring the data and their analysis. Their jovial nature and friendly atmosphere at the office made things easier. I am also appreciative of Dr. D. A. Kring of the Lunar and Planetary Institute for helping coordinate the Meteor Crater surveys, along with the generous staff at the Meteor Crater Museum. I like to thank Dr. P.

Manning for providing me with the permission of using his forward modeling codes. Thanks to GeoKinetics and Anadarko for generously donating seismic datasets and well logs for the Bradford survey, Pennsylvania. I also acknowledge GEDCO and Paradigm Geophysical for their unconditional software support.

Finally, thanks to my biggest supports – my beloved wife Sayantika and my parents. Sayantika walked beside me patiently and supported me in all odds which made this dissertation happen. Her love and encouragement is my biggest asset. My parents' lifelong love and faith in me always gave me strength. It was their encouragement which moved me to pursue my Ph.D. study.

Near-surface Characterization via Seismic Surface-wave Inversion

---

An Abstract of a Dissertation

Presented to

the Department of Earth and Atmospheric Sciences

University of Houston

In Partial Fulfillment

of the Requirements for the Degree

Doctor of Philosophy

By

Soumya Roy

August 2013

ABSTRACT

Characterization of the near-surface is important in identifying shallow properties and structures. In this dissertation, special emphasis is placed on estimating near-surface shear (S)-wave velocities (V_S) which can be used for exploration seismology as well as geotechnical purposes; and even for planetary studies. A frequency-based surface-wave (Rayleigh-wave or ground-roll) inversion method (MASW: Multichannel Analysis of Surface Waves) has been used to estimate 1D and 2D S-wave velocities. The method has been applied on varied seismic datasets related to numerical modeling, physical modeling, and field surveys. The field seismic datasets are from different geological settings and geographical locations: 1) La Marque, Texas, 2) Barringer (Meteor) Crater, Arizona, 3) YBRA field camp, Montana, 4) Hockley fault survey, Texas, and 5) Bradford, Pennsylvania. Estimated S-wave velocities range from as low as 100-300 m/s (La Marque, Hockley) to as high as 3400-3500 m/s (physical model: blank glass block). For the Meteor Crater survey, an unconsolidated near-surface structure (ejecta-blanket) and its thinning thickness trend (thickness decreasing from 20 m to 5 m) has been successfully identified using 2D V_S structure (400-1200 m/s). The depths of investigation for S-wave velocities vary from only 10 m (Hockley survey) to 180 m (Bradford survey) depending on acquisition geometries and source types. Apart from the identification of geological structures; S-wave velocities have been used to calculate S-wave statics and predict densities. The long-wavelength S-wave statics have been calculated for Bradford and Meteor Crater surveys. The densities have been successfully predicted from V_S for modeling

experiments and field data (Bradford and YBRA surveys). All predicted densities are consistent with known values with a maximum error of 6%. The effect of lateral heterogeneity on MASW has also been evaluated using different numerical and physical models (dipping layers varying from 10º to 90º). MASW works well for gentle heterogeneity but provides smeared velocity structures for sharp heterogeneities (physical model experiment and Hockley fault survey). A basic full-waveform inversion scheme has been applied on a numerical model with a vertical interface (i.e. 90º dip) showing its potential to handle lateral heterogeneity problems.

CONTENTS

List of Figures

List of Tables

Chapter 1

Introduction

1.1 Motivation and objective

The primary motivation of this dissertation lies in characterizing the near-surface. It is important to determine near-surface properties (P- and S-wave velocities and densities) for geotechnical and environmental purposes. We also need to "see" through the shallow subsurface to resolve geology and resources at depth. The proper imaging of the near-surface has always been a challenge to seismic processors. The near-surface often has unconsolidated, low-velocity layers which can cause time delays in passing seismic waves (statics), especially for shear (S)-waves. This can lead to the degradation of the seismic image, false interpretation of geological features, and statics problems. Hence, it is necessary to obtain a detailed near-surface velocity structure. Once, a good quality shallow velocity structure is available then it can be applied to derive near-surface properties, identify shallow structures, and solve statics problems.

The goal of this dissertation is to determine the near-surface velocity structures and to apply them for various purposes. In this work, an emphasis is given to the determination of the high-resolution S-wave velocity structure (V_S) which is pertinent

with the increasing use and demand of multicomponent seismic data. The surface-wave (Rayleigh-wave or ground-roll) inversion method can estimate the near-surface V_S structure (Park et al., 1999; Strobbia, 2003; Socco et al., 2010). The surface-wave inversion method is common within the whole-earth (for deeper structures) community as well as for geotechnical studies (for shallow structures). But, the objective is to use the surface-wave inversion method for exploration seismology purposes which is less common in practice. In this dissertation, a frequency-based surface-wave inversion method (Multichannel Analysis of Surface Waves [MASW]) has been used. MASW (Park et al., 1998; ibid, 1999; Xia, 1999) uses the frequency-dependent properties of ground-roll to create dispersion curves (phase velocity versus frequency plots). Then, these dispersion curves are inverted for the fundamental (and higher) modes to provide the near-surface V_S structure.

Different seismic datasets have been used to assess the surface-wave inversion method. Datasets represent varied settings and scales. Modeling data sets (numerical and physical) are useful to correlate the estimated V_S velocities from the surface-wave inversion method with known velocities. Field datasets (La Marque, Texas; Barringer (Meteor) Crater, Arizona, YBRA field camp, Montana, Bradford 3C 3D survey, Pennsylvania, Hockley fault survey, Texas) provide the range of S-wave velocities for different geological settings. Figure 1.1 shows different survey locations from different parts of the USA. Most of the datasets have been acquired by the students and personnel from the Allied Geophysical Laboratories (AGL), University of

Houston, except Bradford survey. The datasets from the Bradford survey have been generously donated by GeoKinetics.

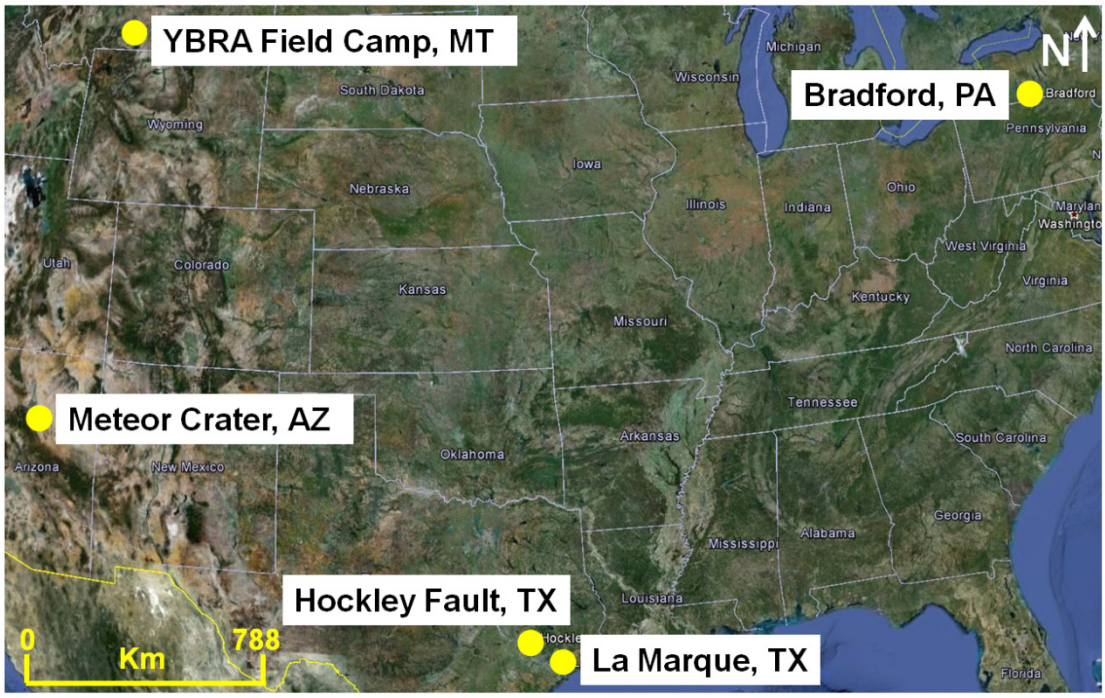

Figure 1.1. Satellite image (from Google Earth) of the locations of the seismic field sites from United States.

1.2 Structure of the dissertation

The basic structure of the dissertation can be divided in three parts – i) determining varied range of S-wave velocities from different studies (Chapter 2 and 3), ii) identifying some limitations of the MASW method and providing possible solutions (Chapter 4 and 5), and iii) applying the estimated S-wave velocities for different

practical purposes e.g. statics calculation, density prediction (Chapter 6 and 7). The following sections briefly introduce different chapters included in this thesis.

Chapter 2 discusses the basic theories of the MASW method and then shows the results (dispersion curves and S-wave velocities) from modeling (both numerical and physical) and field data. The results show how estimated S-wave velocities vary for different scales and geological settings. Some examples have also been presented related to the effect of offset and attenuation on the MASW dispersion curve results.

Chapter 3 is related to a detailed integrated geophysical case study from the Barringer (Meteor) Crater, Arizona. Apart from the S-wave velocities from MASW, P-wave velocities have also been derived from travel-time tomography. Both P- and S-wave velocities are used to identify a complex near-surface low-velocity structure related to the crater mechanism (ejecta blanket). Some results related to ultrasonic measurements, gravity and GPR analyses, and near-surface reflection studies have also been shown.

Chapter 4 discusses the role of lateral heterogeneity on the surface-wave inversion method (MASW). The MASW method is ideal for a horizontally layered earth model i.e. the earth model may be vertically heterogeneous but individual layer is laterally homogeneous. Datasets from numerical simulation, physical modeling, and a field

study have been used to identify the effect of gentle to sharp lateral heterogeneity on the MASW method.

Chapter 5 introduces a simple full-waveform inversion scheme as a solution for handling the lateral heterogeneity effect on MASW. The inversion scheme is based on forward-difference approach. Different forward modeling tools have been used to generate synthetic datasets. The full-waveform inversion procedure is applied on synthetic datasets with laterally homogeneous and laterally heterogeneous models.

Chapter 6 shows a practical application of the MASW method. The S-wave velocities from the MASW method are applied to estimate the S-wave statics. This is a stand-alone method of determining S-wave statics which does not depend on the P-wave statics value. S-wave statics are calculated for field datasets (Bradford and Meteor Crater survey). For the Bradford survey, a set of already calculated S-wave statics using traditional method have been provided by GeoKinetics. The S-wave statics estimated from the MASW method is compared with the given values.

Chapter 7 discusses another application of the MASW method. In this chapter, S-wave velocities are used to predict densities. Predicting densities from P-wave velocities (Gardner et al., 1974) is common in exploration studies. We have attempted predicting densities from S-wave velocities. First, densities are predicted from S-wave sonic logs and compared with actual density logs (for well logs from Bradford

survey). Then densities are predicted from S-wave velocities (derived from MASW method) and compared with known density values. Numerical simulation, physical modeling (blank glass block), and field data (from YBRA field camp) are used to test and compare predicted densities from S-wave velocities.

Chapter 2

Surface-wave inversion (MASW)

2.1 Introduction

The surface-wave inversion method is used to estimate the S-wave velocity in its propagation path. This is a popular method in the earthquake or whole-earth community (Anderson, 1984; Simons et al., 2002; Li and Detrick, 2003; Li and Detrick, 2006) as well as in the geotechnical community (Ryden et al., 2004). For the whole-earth application, the seismic traces contain very low frequencies or long periods and the goal is to delineate the crust or mantle properties (S-wave velocities). On the other hand, relatively high-frequency information is required for the geotechnical or civil engineering applications e.g. estimation of S-wave velocities and hence stiffness and soil properties for shallow subsurface; identification of cavities, tunnels etc.; and liquefaction studies (Lin et al., 2004). For the geotechnical purposes, S-wave velocities are generally evaluated for less than 100 m of subsurface. The main motivation of this dissertation is to apply the surface-wave inversion method beyond the realm of earthquake and civil engineering communities. We have applied the surface-wave inversion method to: i) estimate S-wave velocities and to delineate shallow geological structures, and ii) use the estimated S-wave velocities for different

exploration seismology purposes (S-wave statics calculation, density prediction, full-waveform inversion, etc.).

There are different surface-wave inversion methods available. Two commonly used surface-wave methods for the near-surface analysis are Spectral Analysis of Surface Waves (SASW) and Multichannel Analysis of Surface Waves (MASW). For the SASW method (Nazarian et al., 1983; Stokoe and Nazarian, 1983), only two geophones (or channels) are used and the data acquisition procedure is slow. The MASW method (Park et al., 1998; Park et al., 1999; Xia et al., 1999) is a frequency-based method and multiple geophones (or channels) are used. MASW is faster than SASW method and it has gained popularity (mainly in the geotechnical community) for the near-surface characterization. The acquisition geometry for MASW is very similar to the regular 2D seismic data acquisition geometry and hence no additional effort is required. We have applied the MASW method throughout the dissertation to estimate the S-wave velocities from the raw shot gathers (numerical modeling, physical modeling, and field data).

2.2 A brief description of the MASW method

The vertical (and radial) components of raw seismic shot gathers contain Rayleigh waves (i.e. surface-wave or ground-roll) if a free-surface (e.g. air-sediment interface) is present. Now, if the subsurface is layered and large velocity contrasts are present

(e.g. large velocity change across water-table) then the surface waves become more or more dispersive in nature (Liner, 2012). So, the dispersion studied here is layer-induced apparent dispersion as opposed to intrinsic dispersion which is related to actual rock materials. The MASW method uses this dispersive property to estimate S-wave velocities. The MASW method has been developed with the assumption that the subsurface is vertically heterogeneous and laterally homogeneous (i.e. a layer-cake model). The MASW method is a two-fold procedure. Step 1 is to generate the dispersion curves (frequency vs. phase velocity plots), and step 2 is to perform the inversion of dispersion curves to estimate S-wave velocities.

2.2.1 Generation of dispersion curves

MASW is a wavefield transformation method (Park et al., 1998) which first generates dispersion curves directly from the raw shot gathers. In the MASW method, the offset-time domain data (i.e. a raw shot gather) is first transformed to offset-frequency domain through 1D Fourier transform providing a combination of amplitude and phase spectra. The amplitude spectrum contains the information related to attenuation, spherical divergence, etc., whereas phase spectrum contains the information about dispersion (Park et al., 1998). Here, the term dispersion indicates the change of Rayleigh-wave phase velocities with frequencies. The MASW method is a frequency-based phase-shift method. A phase-shift is first applied followed by an integration which sums the entire wavefield related to a given offset range for a single frequency and a series of phase velocities. There will be a particular phase velocity at

given frequency which would yield a large value of the integral (or peak). Other velocities would yield a very small or zero value. The integration is then repeated in the similar fashion for other frequencies and same velocity range. In this way, a phase velocity-frequency image matrix will be produced containing dispersion curves. The dispersion curves can be multi-modal i.e. for a particular frequency there may be more than one phase velocities which produce large integral values (or peaks). So, the phase velocity-frequency image may contain a single dispersion curve (fundamental mode) or multiple curves (fundamental and higher modes). The higher modes have greater velocities than the fundamental mode at a particular frequency; hence, they have longer wavelengths and can penetrate deeper. Using higher modes may provide improvement in velocity estimations (Xia et al., 2003; Wisén et al., 2010).

2.2.2 Inversion of dispersion curves

Once a good quality dispersion curve is generated, an inversion scheme is applied to estimate the S-wave velocities from Rayleigh-wave (or ground-roll) phase velocities. For a homogeneous medium, it is commonly assumed that S-wave velocity (V_S) is related to the Rayleigh-wave velocity (V_R) through the linear relationship of - $V_R = 0.9194V_S$ for the Poisson's ratio of 0.25 (Sheriff and Geldart, 1985). First, an initial S-wave velocity model is derived based on the observed dispersion curve information. Then, a calculated dispersion curve (model response) is generated via forward modeling (from the initial S-wave velocity model). Then, the difference between the

observed and estimated dispersion curves is minimized in an iterative way and S-wave velocities are updated after individual iteration.

The MASW method is always applied on individual raw shot gathers. So, one single dispersion curve is inverted to estimate one 1D S-wave velocity structure. The 1D velocity structure for a shot gather is placed at the middle of the receiver spread related to that shot. So, the 1D S-wave velocity structure represents the averaged velocity of the active receiver spread for one shot. Then, same analysis is performed for consecutive shot gathers and finally multiple 1D S-wave velocity structures are merged (using interpolation technique) to generate a 2D S-wave velocity structure. A detailed description of the MASW method has been provided in Appendix A. The results related to the dispersion curves and S-wave velocities have been provided in the following sections and chapters.

2.3 Seismic experiments and surveys

I have applied the MASW method on different seismic datasets related to numerical modeling, physical modeling, and field datasets. I have purposefully used seismic datasets related to different scales, different geological settings, different acquisition geometries, sources, and receivers with the goal to test the applicability and robustness of the MASW method. The MASW method has been applied on datasets related to sources varying from ultrasonic transducers to 10-lb sledgehammer to

dynamite; receivers varying from pin transducers to 14 Hz vertical planted geophone to 3C geophones; and geophone intervals from 2 m to 5 m to 33.5 m. The MASW method has also been applied for different geological settings varying from layer-cake geological settings related to coastal plain (La Marque, Texas) to highly complex, brecciated near-surface of a unique astrobleme (Meteor Crater, Arizona). The following sections briefly describe few different experiments and field surveys, the seismic datasets from which have been used in this dissertation. These sections also show the dispersion curve and S-wave velocity results obtained from the MASW method. Though, some more experiments and survey areas will be introduced and discussed in details during later chapters.

2.3.1 Numerical modeling

Synthetic seismic datasets for a three-layer (two layers over a half-space) model are generated using ANIVEC which is a frequency-wavenumber based forward modeling code (Mallick and Frazer, 1987). A 30 Hz Ricker wavelet has been used as source wavelet along with the receiver interval of 2 m and shot interval of 20 m. The physical properties of the model are – Layer 1: V_P = 1000 m/s, V_S = 500 m/s, ρ = 1.74 gm/cc, thickness = 15 m, Layer 2: V_P = 1300 m/s, V_S = 740 m/s, ρ = 1.86 gm/cc, thickness = 45 m, and Layer 3 (Half-space): V_P = 1800 m/s, V_S = 1100 m/s, ρ = 2.02 gm/cc. Densities of each layer are set using the original Gardner's relation for P-wave velocities. The Quality factor (Q) is set as 100 for all layers (and for both P- and S-waves) which indicates weak attenuation.

A synthetic raw shot gather for the abovementioned model has been shown in Figure 2.1 with dispersive surface waves. As already discussed, the dispersion curve generation algorithm in MASW involves wavefield summation over an offset range. So, it is critical in MASW to select the optimum offset range (i.e. spatial window). If the near-offset (the distance from the source to the first active receiver for that analysis) is very short (or close) then near-field effects (the effects of non-planar surface-waves as the first active receiver is very close to the source) may contaminate the dispersion curve results (Park et al., 1999). On the other hand, if we select a long far-offset (the distance from the source to the last active receiver for that analysis) and/or long spatial window (far-offset – near-offset); then far-field effects (the influence of high frequency noise, higher modes, body wave energies etc. at far distance) may also contaminate the dispersion curves (Park et al., 1999). So, one should carefully select the optimum offset range or spatial window (Park et al., 2001; Park and Ryden, 2007; Ivanov et al., 2008; Park, 2011). This also depends on the type of source and receiver, acquisition geometry, and subsurface lithology. In addition, selection of longer spatial window may also incorporate the effect of lateral heterogeneity. Figure 2.2a shows a schematic of near-offset, far-offset, and spatial window concepts. Figure 2.2b-e show a series of dispersion curves for different spatial windows (300 m, 200 m, 150 m, and 100 m) related to the synthetic case. Since the synthetic seismic datasets are free of noise and attenuation, the long spatial window does not show any significant deterioration of the dispersion curve. In fact, the longer spatial window has generated sharper dispersion curve (Figure 2.2b). But

in reality, field-data has poor signal-to-noise ratio at large offset along with the attenuation. So while analyzing the field-data, selection of optimum offset range or spatial window is important. Such an example of selecting optimum offset has been provided in Chapter 3 for the Meteor Crater survey (Figure 3.7).

Next, the multiple dispersion curves have been generated for the above mentioned model for all shot gathers and then inverted to estimate the 2D S-wave velocity structure (Figure 2.3). The MASW method has successfully identified the transition between the first layer and the second layer at around 15 m. The estimated first layer S-wave velocity is approximately 500-600 m/s (actual value: 500 m/s) and second layer S-wave velocity is approximately 650-750 m/s (actual value: 740 m/s). The results show that the MASW method has worked reasonably well for the synthetic dataset. Also, the numerical modeling experiment is useful to test the MASW method as all model parameters are known.

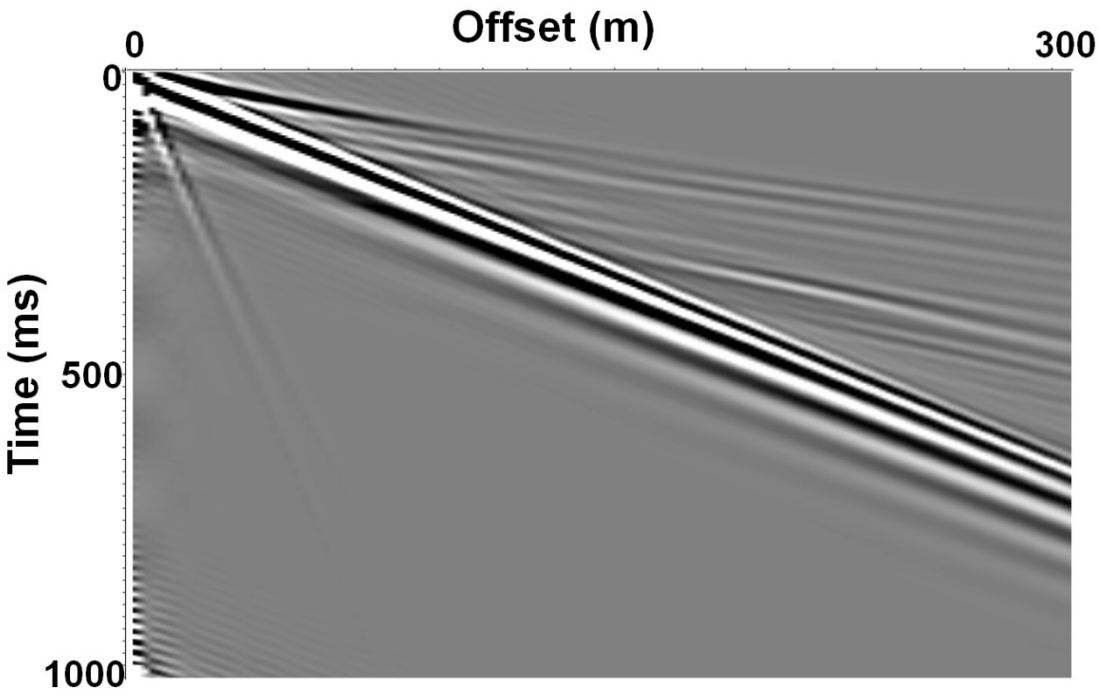

Figure 2.1. A synthetic raw shot gather, generated using the forward modeling code ANIVEC, shows a dispersive fan of surface waves.

a)

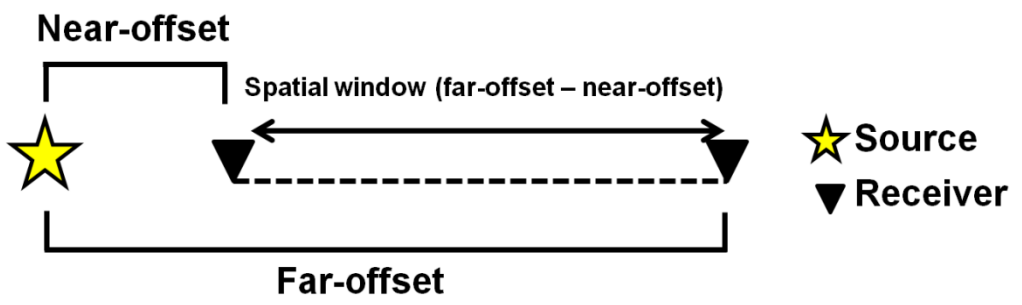
Near-offset
Spatial window (far-offset – near-offset)
Source
Receiver
Far-offset

b)

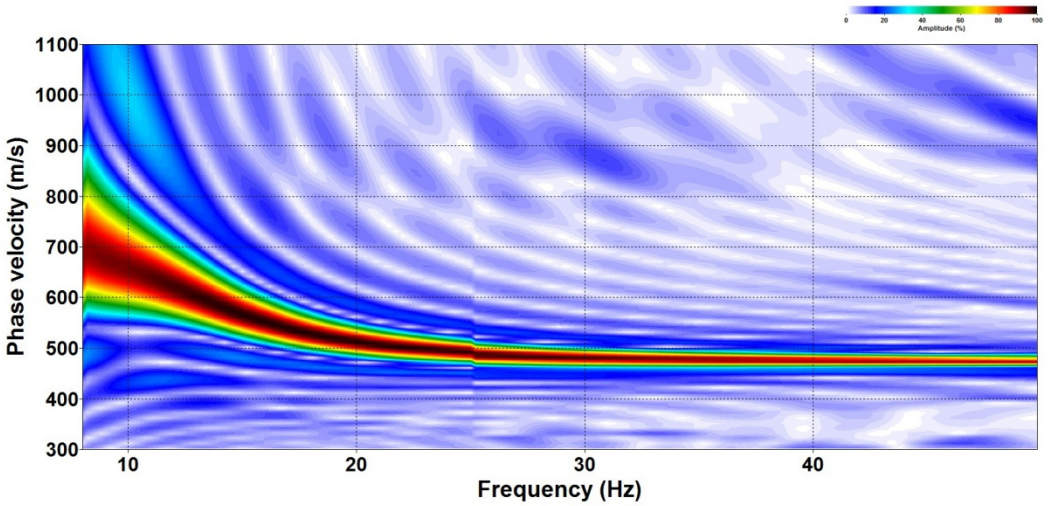
Amplitude (%)
Phase velocity (m/s)
Frequency (Hz)

c)

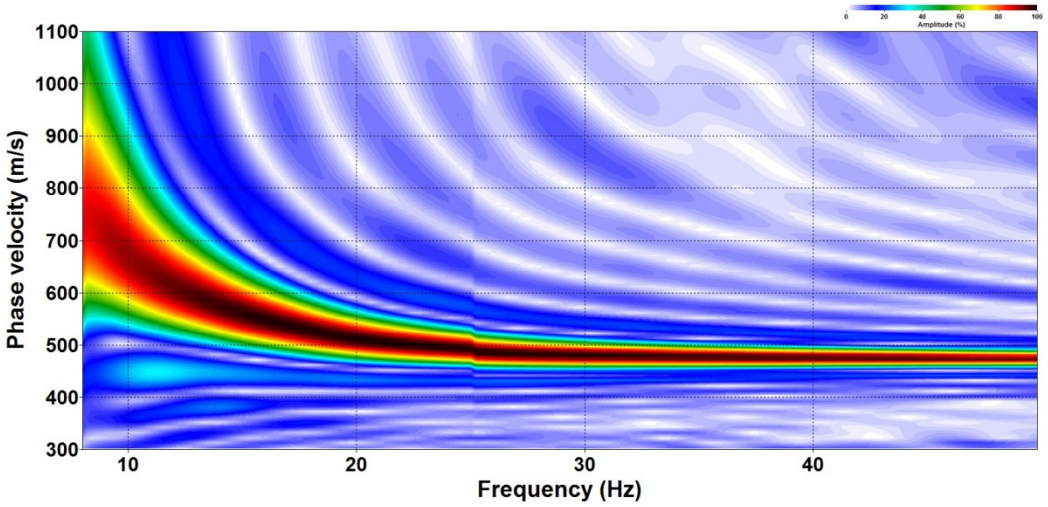
Amplitude (%)
Phase velocity (m/s)
Frequency (Hz)

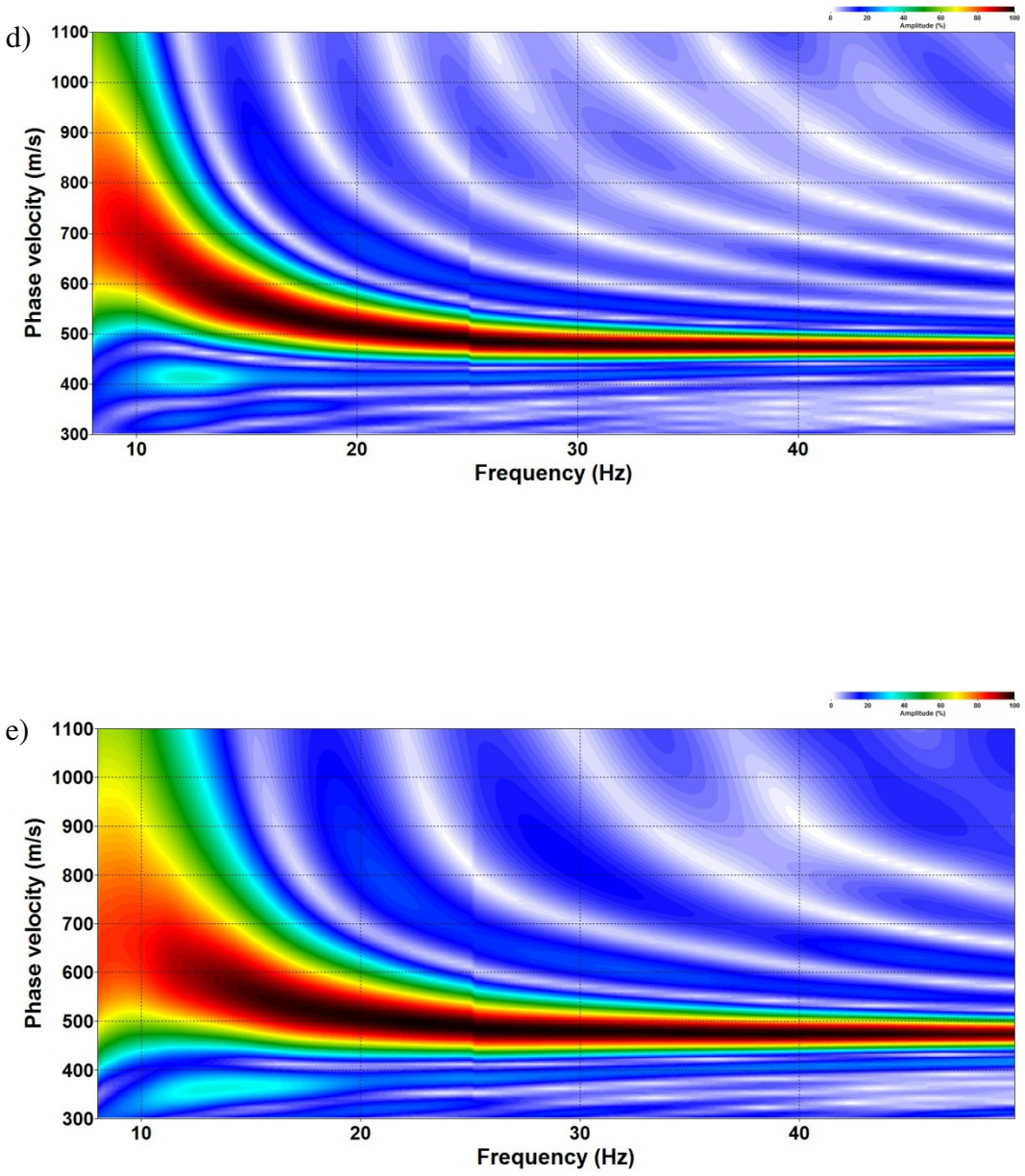

Figure 2.2. a) A schematic diagram demonstrating near-offset, far-offset, and spatial window definitions; and the dispersion curves related to the synthetic model for spatial windows of – b) 300 m, c) 200 m, d) 150 m, and e) 100 m.

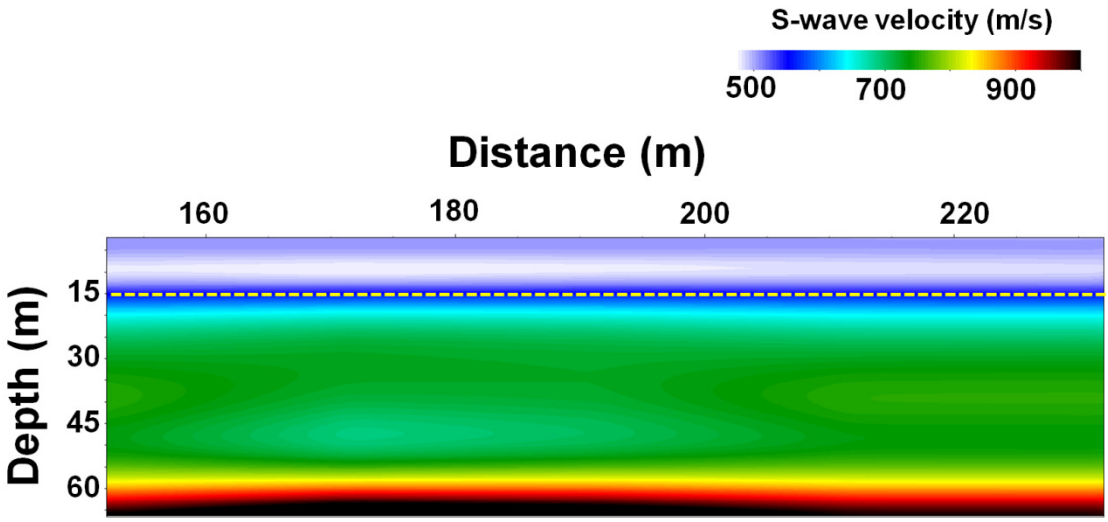

Figure 2.3. The 2D S-wave velocity structure related to the numerical modeling experiment. The yellow dashed line shows the interface between the first and second layer which is approximately identified from the MASW analysis also.

2.3.2 Physical modeling

This physical model experiment was a good way to test the feasibility of the MASW method as the physical model parameters are all known. So, one can compare the MASW results with the actual values. Also, the seismic datasets from this experiment are the results of real wave propagation as opposed to the only numerical results for synthetic datasets. The seismic datasets were acquired over a uniform velocity blank glass model (Figure 2.4) using the ultrasonic measurement systems at the Allied Geophysical Laboratory, University of Houston. Vertical contact transducers of 1 MHz central frequency are used as source and receivers. The receiver interval was of 0.4 mm (i.e. 4 m when scaled by the seismic-ultrasonic factor of 10000) with 26-

receiver spread, source to-receiver offset was16 mm (i.e. 160 m), and shot interval was of 0.4 mm (i.e. 4 m). The parameters for the blank glass model are - V_P~5804 m/s, V_S ~3447 m/s and density (ρ) ~ 2.6 gm/cc. Figure 2.5 shows a raw shot gather with non-dispersive ground-roll and Figure 2.6 shows a flat dispersion curve estimated using the MASW method. Since the glass model is homogeneous, a flat non-dispersive dispersion curve is observed. The flat ground-roll velocity in the raw shot gather is approximately 3071 m/s and dispersion curve trend is approximately 3000-3100 m/s. Figure 2.7 shows the final 2D S-wave velocity model estimated through the inversion of the dispersion curves for consecutive raw shot gathers. The estimated S-wave velocities are at around 3400-3500 m/s where the actual S-wave velocity of the glass model is 3447 m/s. So, the estimated S-wave velocity result using the MASW method shows good correlation with the actual known value.

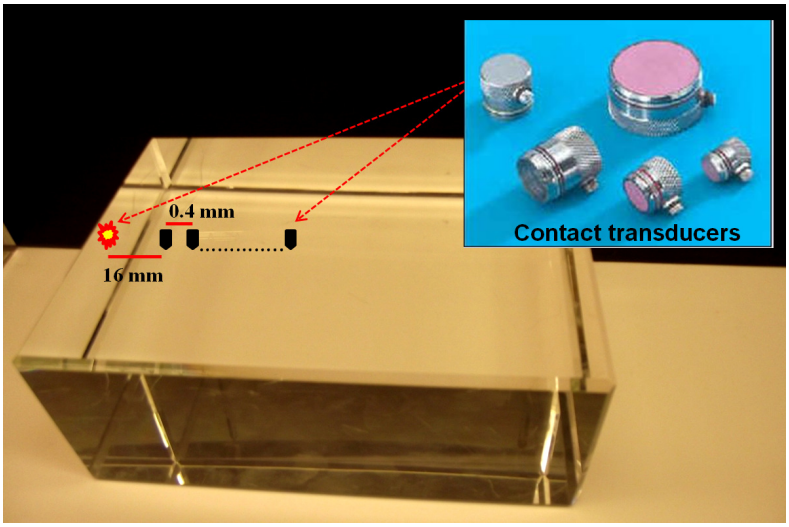

Figure 2.4. The figure shows the uniform velocity, homogeneous glass model used in the physical modeling experiment with example of contact transducers in the inset.

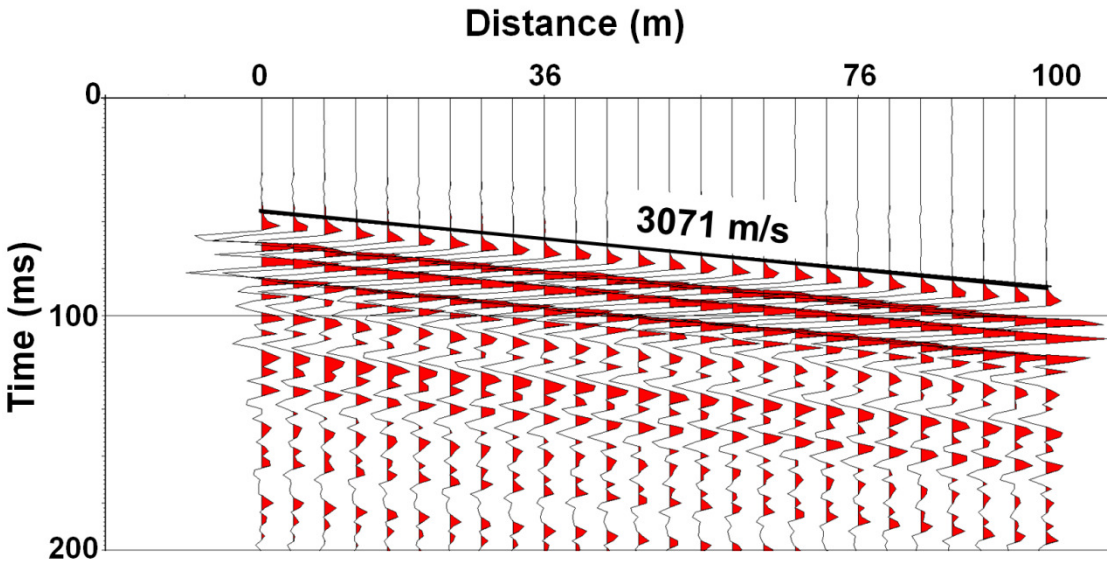

Figure 2.5. A raw shot gather from the physical modeling experiment (blank glass model) showing a non-dispersive ground-roll (in black solid line).

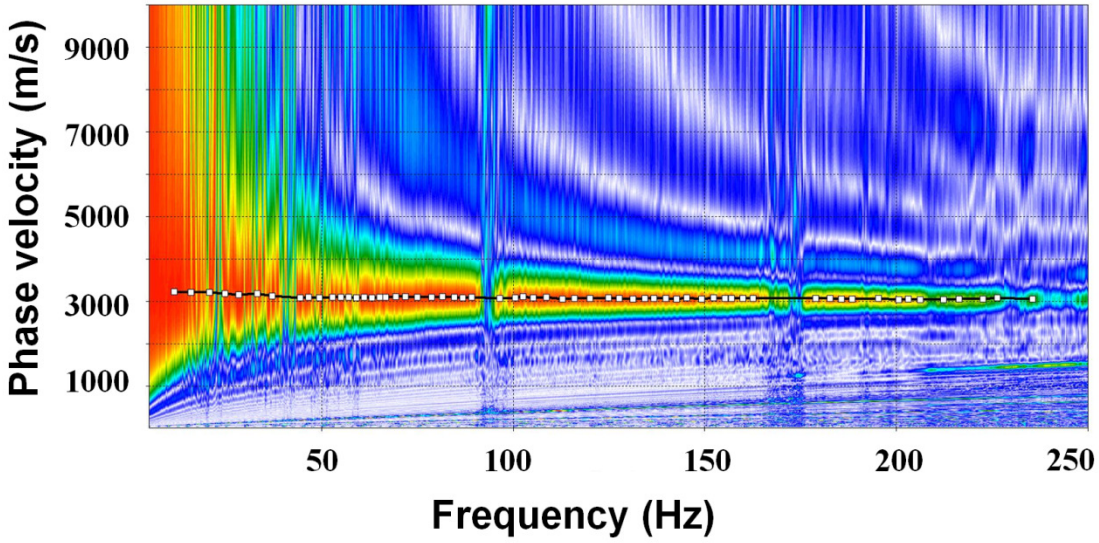

Figure 2.6. A flat dispersion curve estimated from a raw shot gather from the physical modeling experiment (blank glass model).

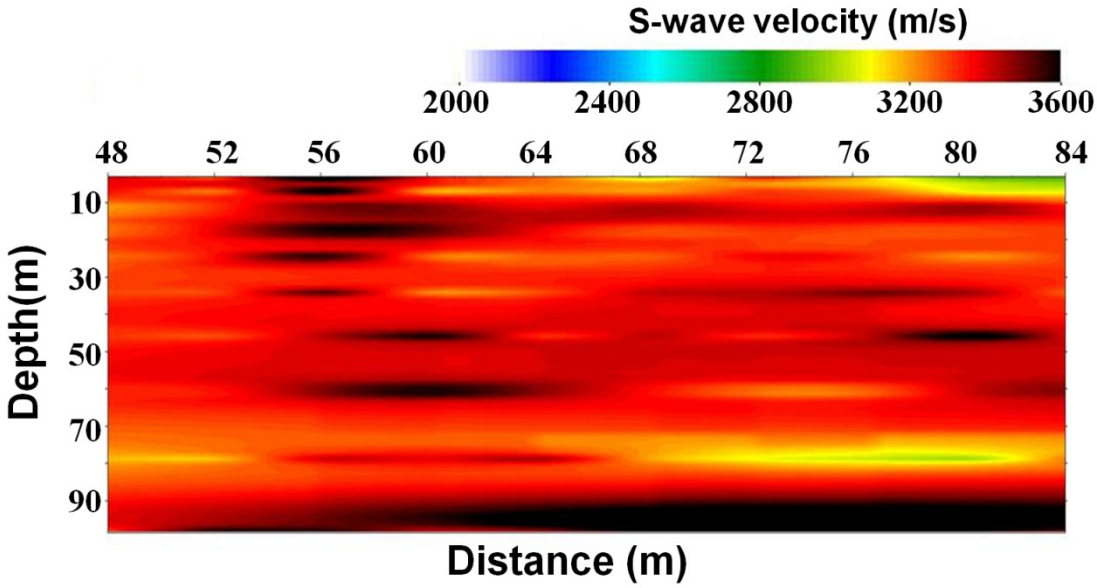

Figure 2.7. The figure shows the final 2D S-wave velocity structure for the blank glass model.

2.3.3 La Marque Geophysical Observatory, Texas

The La Marque Geophysical Observatory is at the UH Coastal Center in Galveston County, Texas (Figure 2.8). The coastal region of Texas is characterized by the flat-lying sediments (Salvador, 1991; Turolski, 2013). The sediments at the observatory are from the Quaternary Beaumont Formation and consist of clay and silty clay (Capuano and Jan, 1996). The seismic data used in this section were acquired in March, 2010 using a 10-lb sledgehammer as the source and planted vertical geophones as receivers (with 2 m receiver interval) along a NS-trending line (Figure 2.9).

Figure 2.8. The location map of the La Marque Geophysical Observatory.

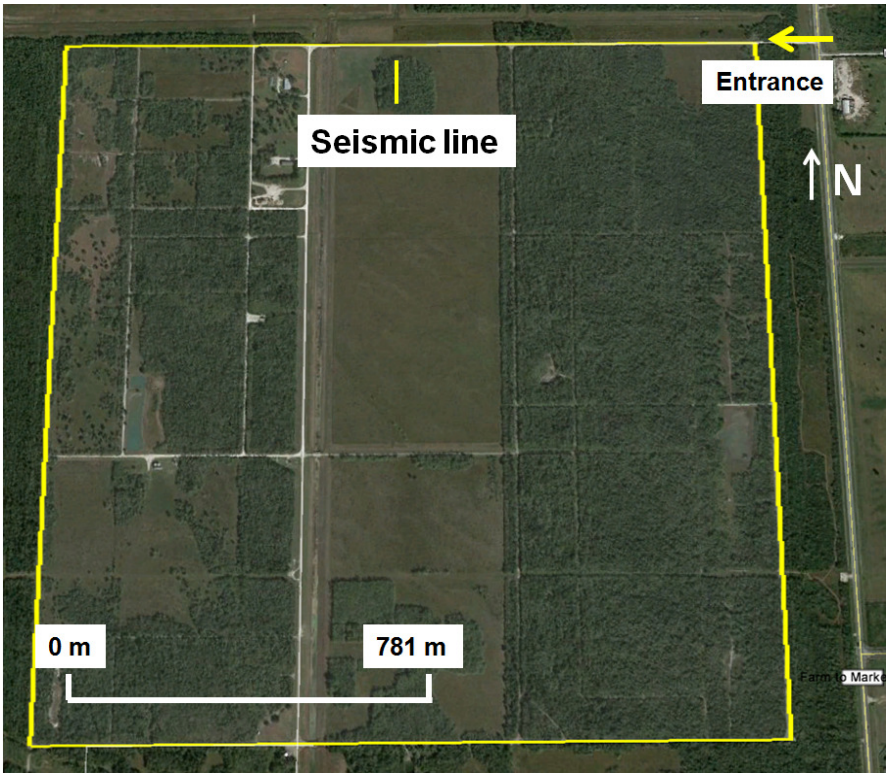

Figure 2.9. The figure shows a zoomed view of the La Marque Geophysical Observatory and the location of a NS-trending seismic line used in this study.

A raw shot gather from the La Marque study (Figure 2.10) shows the well developed fan of dispersive ground rolls or surface waves. Figure 2.11 shows the multimodal dispersion curve generated from a raw shot gather as opposed to the flat non-dispersive dispersion curve from the homogeneous physical model (Figure 2.6). The final 2D S-wave velocity profile (Figure 2.12) shows a flat structure with very low S-wave velocities varying from 100 m/s to 300 m/s.

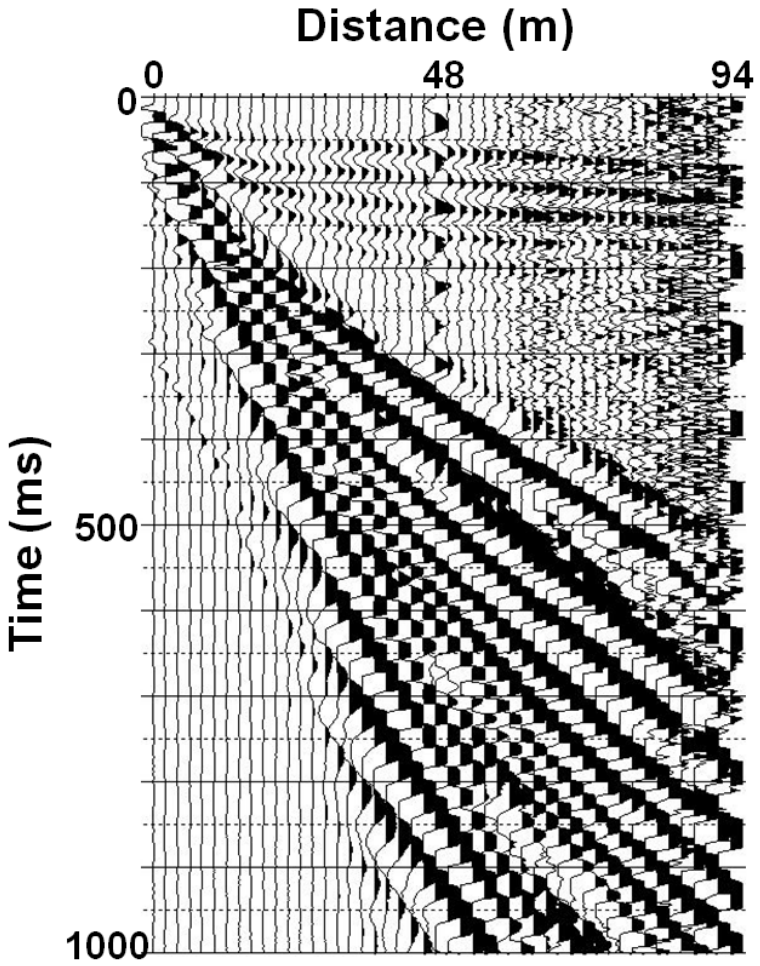

Figure 2.10. A raw shot gather from the seismic line in Figure 2.9 (La Marque survey) showing dispersive surface waves.

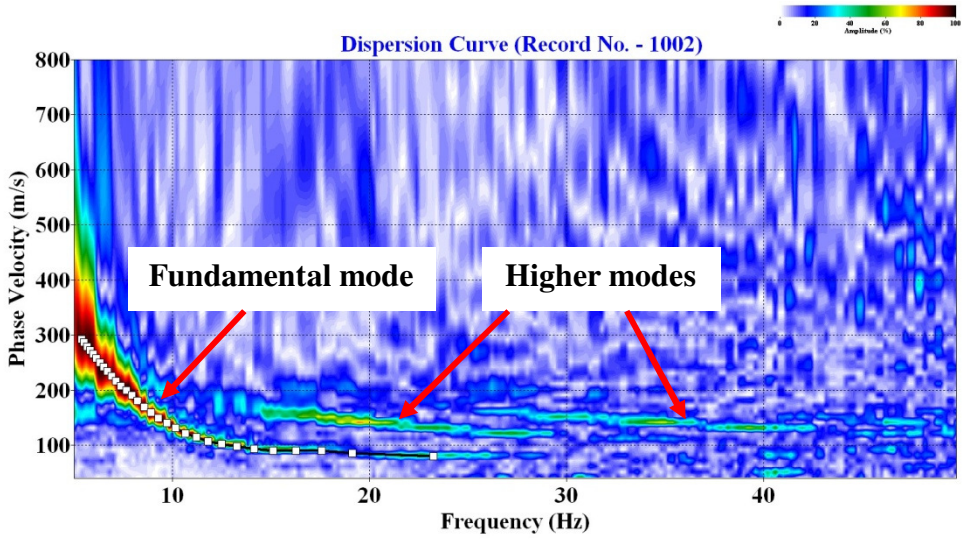

Figure 2.11. The figure shows a multimodal dispersion curve from the La Marque survey.

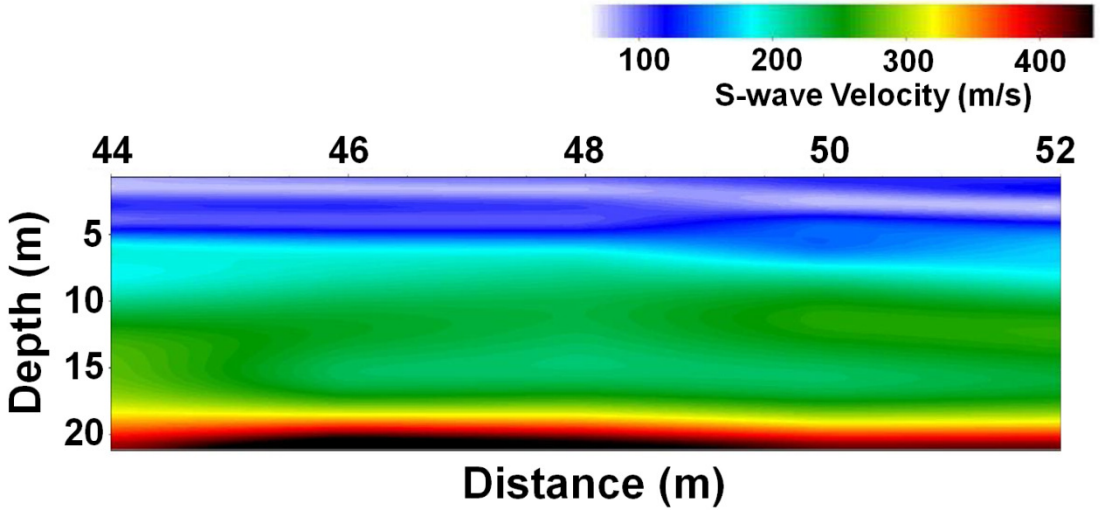

Figure 2.12. A 2D S-wave velocity structure (plotted from the ground surface: 0 m) from the La Marque survey showing low S-wave velocities.

2.3.4 Barringer (Meteor) Crater, Arizona

The University of Houston, the University of Texas (Austin), and the Lunar and Planetary Institute (LPI) jointly organized a geophysical expedition at the Barringer (Meteor) Crater site in May 2010. Barringer (Meteor) Crater, situated near Winslow, Arizona, was excavated some 49,000 years ago by the collision of a high-velocity iron-nickel meteorite with the Colorado Plateau (Kring, 2007). One of the principal goals of this survey was to image this ejecta blanket (debris thrown out of the crater during the impact) structure. The MASW method has been applied to estimate the 2D S-wave velocity structure for a 645 m long seismic line from the south flank of the crater. This velocity structure has successfully imaged the ejecta blanket. The detailed geophysical analysis and geological interpretation can be found in Roy and Stewart (2012) and in Chapter 3.

2.4 MASW and attenuation

The MASW analysis is affected by various parameters –offset range (section 2.3.1), attenuation etc. This section discusses the effect of attenuation on MASW. In fact, some attempts had been made to estimate the attenuation or Q from Rayleigh waves (Xia et al., 2001). A numerical modeling experiment with different attenuation or Q has been performed using ANIVEC. The numerical model parameters have been chosen as - Layer 1: V_P = 750 m/s, V_S = 250 m/s, ρ = 1.62 gm/cc, and thickness = 8

m; Layer 2: V_P = 1000 m/s, V_S = 500 m/s, ρ = 1.74 gm/cc, and thickness = 8 m; Half-space: V_P = 1600 m/s, V_S = 800 m/s, ρ = 1.95 gm/cc. Now, for experiment 1, Q (for both P-and S-waves) has been chosen as 100 (lower attenuation) and for experiment 2 Q (for both P- and S-waves) has been chosen 10 (higher attenuation) for the same numerical model. Figure 2.13 shows amplitude spectra for different offsets (8 m, 68 m, 168 m, and 208 m) for the synthetic dataset for experiment 1 and 2. As anticipated, the amplitude spectra show that for the attenuative experiment 2, overall absolute amplitudes are lower and high frequencies are lost. The dispersion curves for the same experiments show that the fundamental mode energy for the experiment 2 (Q = 10 case) is lost for the high frequencies compared to Q=100 case (Figure 2.14). Some examples from the field surveys (Meteor Crater survey in Chapter 3) have also shown a similar effect of attenuation.

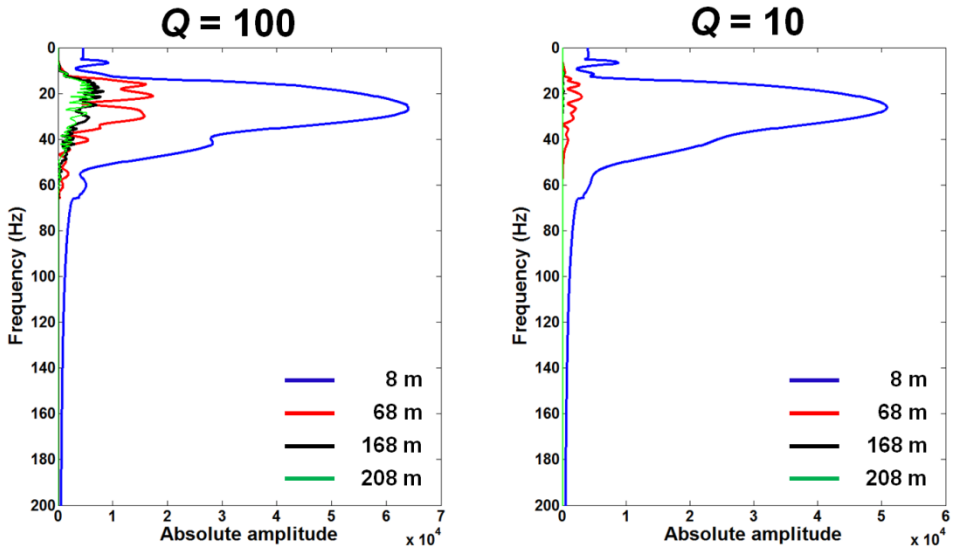

Figure 2.13. The figures show the amplitude spectra from synthetic dataset for Q = 10 and Q = 100 for different offsets - 8 m (solid blue), 68 m (solid red), 168 m (solid black), and 208 m (solid green).

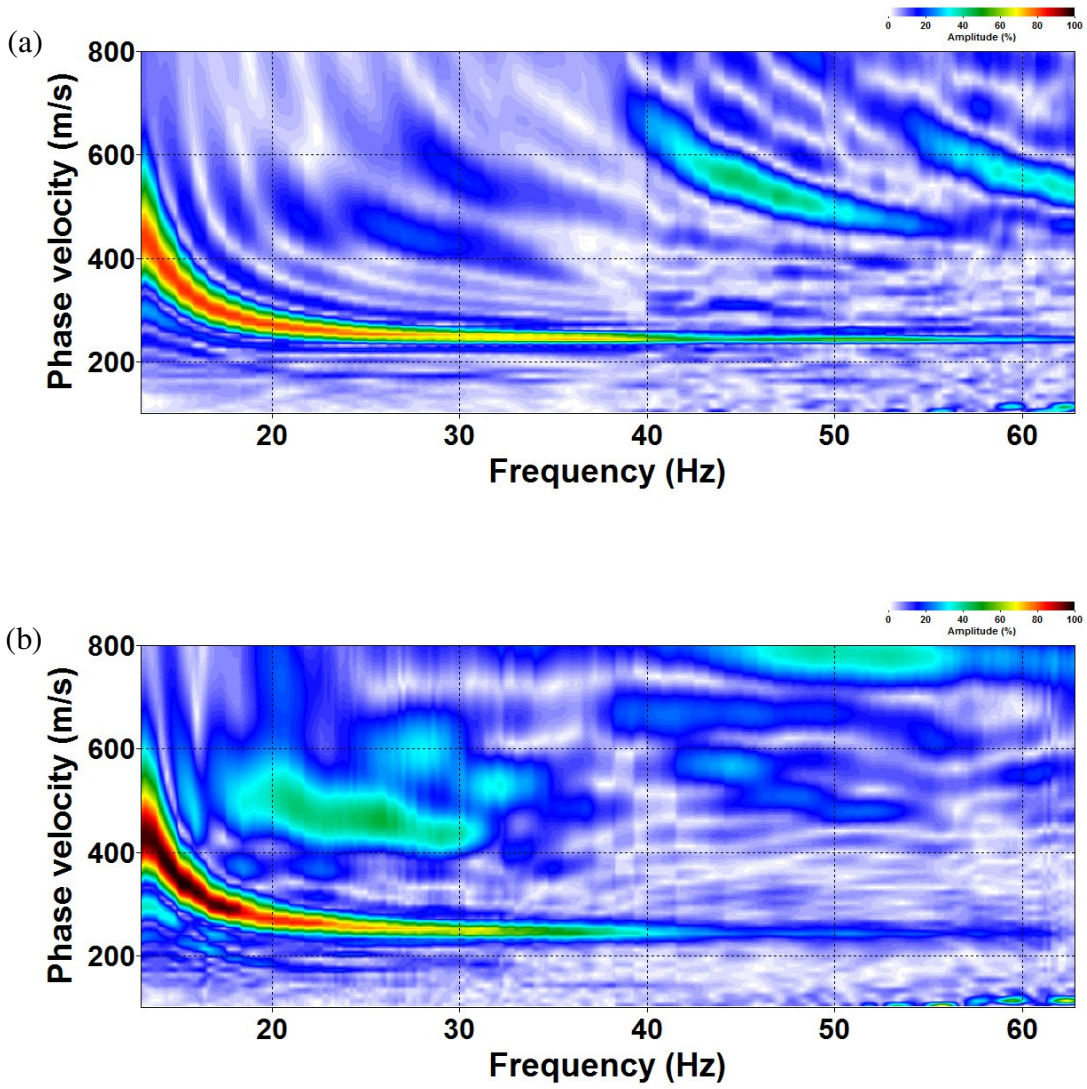

Figure 2.14. The dispersion curves for numerical experiments showing – a) greater high frequency content of fundamental mode for Q = 100 case, and b) loss of high frequency energies for Q = 10 case.

2.5 Conclusions

We have briefly discussed a frequency-based surface-wave inversion method (MASW) in this chapter. The MASW method is then applied to different datasets – modeling (numerical and physical) and field data (La Marque, Meteor Crater). The results show well-developed dispersion curves (fundamental and higher modes). The inversions of dispersion curves yield S-wave velocity results for wide range – as low as 100 m/s for La Marque survey to very high value for the glass model (3400-3500 m/s). Different analyses show that the MASW method has been applied successfully to derive the near-surface S-wave velocities. The effects on MASW method related to attenuation, offset etc. have also been identified and demonstrated with different datasets.

Chapter 3

A detailed case study of an impact crater: Barringer (Meteor) Crater, Arizona

3.1 Introduction

Barringer (a.k.a. Meteor) Crater is situated near Winslow in Arizona, USA (Figure 3.1a). The crater was excavated some 49,000 years ago as a consequence of the collision of a high-velocity iron-nickel meteorite with the existing Colorado Plateau (Kring, 2007). Meteor Crater is one of the first recognized, best exposed, least eroded, and well preserved impact craters on this planet (Shoemaker, 1987). The meteorite impact created a 180 m deep, smooth, bowl-shaped depression with no central uplift. Meteor Crater has the diameter of approximately 1.2 km with the raised rim structure (some 30 to 60 m above the surrounding plain). Based on these structural properties, Meteor Crater can be categorized as a simple crater (Melosh, 1989; Mazur et al., 2000; Kring, 2007). The ejecta blanket (debris thrown out of the crater during the impact) is also present on the rim and flanks of the crater as expected for any impact crater. Due to the impact shock, the near-surface of the crater rim and flank is fractured or brecciated composed of unconsolidated debris of different lithological components and meteoritic materials.

In May 2010, a joint expedition took place at the crater site by the University of Houston, the University of Texas at Austin, and the Lunar and Planetary Institute (LPI) to investigate and image the shallow subsurface of the crater using geophysical methods (especially near-surface seismic methods). The primary motivations behind this survey are to: i) determine physical properties (velocities, densities, conductivities etc.) of materials affected by impact structures, ii) identify the near-surface geological structure, especially the ejecta thickness and faulting, and iii) assess various geophysical techniques for imaging crater structures. An initial attempt had been made in Roy and Stewart (2012) to answer some of these questions. Extensive geological studies assessed the crater for long time. This study aims to contribute some geophysical measurements and results; and to focus towards the advanced geological interpretation from those geophysical results. The recent meteor showers (February 2013) at Chelyabinsk in Russia and related hazards reinforce the significance of this kind of study to provide a more detailed understanding of impact structures.

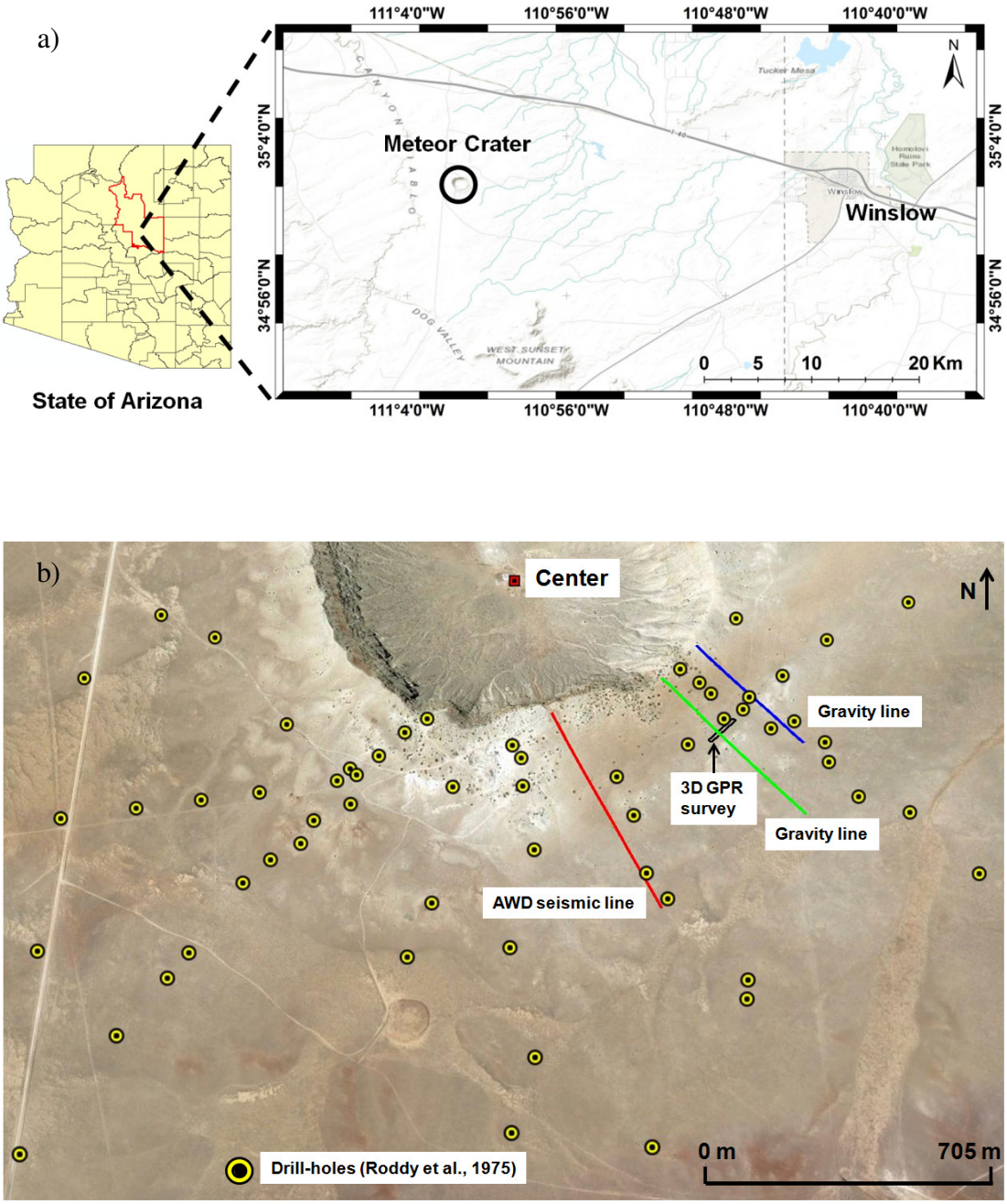

Figure 3.1. Satellite image shows – a) the location of Barringer (Meteor) Crater, and b) a zoomed view of the survey area showing seismic line, gravity lines, GPR survey, and drill-hole locations from the rotary drilling program of Roddy et al., 1975 (Google Earth plots).

3.2 Geological background of Meteor Crater

The pre-impact stratigraphy was composed of sedimentary layers related to famous Grand Canyon sequence. The impact activity involved younger strata of Triassic and Permian age. The geological features and lithological distribution pattern at the Meteor Crater are consistent with any typical impact crater. The present day near-surface normal stratigraphy at Meteor Crater consists of white Coconino sandstone overlain by the very thin Toroweap sandstone and followed by the yellowish Kaibab dolomite formation. These Permian age formations are overlain by the red Moenkopi siltstone of Triassic age. Now, the impact created an overturned sequence of debris derived from bedrocks (Coconino, Kaibab, and Moenkopi) and deposited at the top of the normal bedrock sequence. The overturned layers consist of debris from Coconino-Toroweap at the top, underlain by debris from Kaibab, followed by debris from Moenkopi at the base, and then underlain by the normal bedrock sequence (Figure 3.2). This whole package of inverted, unconsolidated sequence of debris is commonly known as "ejecta blanket". The ejecta at the Meteor Crater site is extended up to 1-2 km away from the edge of the crater (Kring, 2007). Though this impact structure is relative younger, still differential erosion took place at the area eroding some overturned layers. Hence at the very top of the ejecta blanket, thin film of recent alluvium (due to erosion) is also observed. The ejecta may also contain fragments of actual metallic extra-terrestrial meteorites. We have used the following abbreviations for the lithologies – Q_{al} (recent alluvium), Q_{ct} (debris from Coconino-Toroweap), Q_k (debris from Kaibab), Q_m (debris from Moenkopi), T_m (Moenkopi), P_k (Kaibab), and

P_{ct} (Coconino-Toroweap) which mostly follow the nomenclature used in Shoemaker (1960). So, to summarize the present day stratigraphy at the site, one should expect to find the following sequence from top to bottom – Ejecta blanket ($Q_{al} – Q_{ct} – Q_k – Q_m$) underlain by $T_m – P_k – P_{ct}$. Though, due to complex impact mechanism and erosion, this ideal sequence is not present at many areas of the rim and flanks. More on that has been discussed in the interpretation section. Since the ejecta blanket is mixed debris, it is relatively unconsolidated compared to the bedrock. Hence for our purpose, we should anticipate that the ejecta would have lower seismic velocities compared to bedrocks of higher seismic velocities.

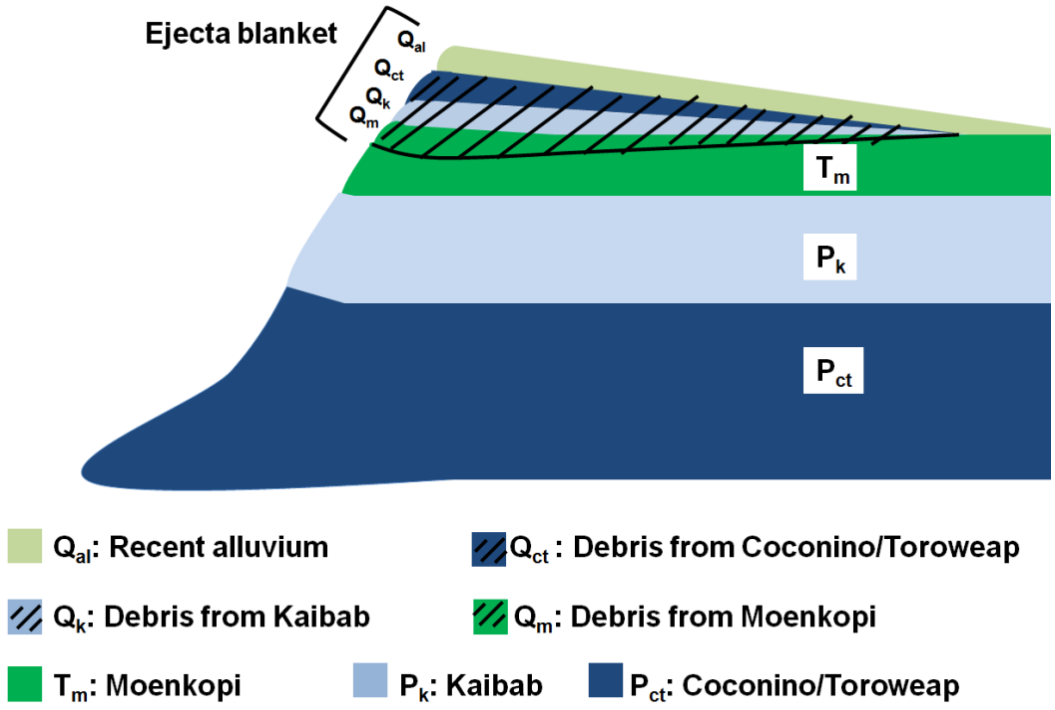

Figure 3.2. Schematic diagram of the modern-day stratigraphy at Meteor Crater (modified after Shoemaker et al., 1974; Kring, 2007).

3.3 Drilling database

During 1970s, extensive drilling program was coordinated on the rim and flanks of Meteor Crater. A huge database of drilling results from Meteor Crater is available from Roddy et al. (1975), other literatures (Kring, 2007), and USGS website. The drilling database contains information about identified lithologies from rock samples and drill cuttings. So, this is very helpful to identify the transition from the ejecta blanket to the bedrock Moenkopi (T_m) and deeper lithological transitions (bedrock Moenkopi to bedrock Kaibab). Unfortunately, there are very few drill-holes along the AWD line. To overcome the lack of control points along the AWD line, we have used several drill-holes from the south flank (Figure 3.1b) surrounding the AWD line to make interpolated geological model which can be used to interpret the obtained velocity results. The transitions- i) from the ejecta blanket to the bedrock Moenkopi, and ii) from the bedrock Moenkopi to the bedrock Kaibab have been plotted for several drill-holes generating a 2D profile (Figure 3.3). We also used these drill holes to make an interpolated horizon map of the ejecta to Moenkopi transition plane and overlaid on the Meteor Crater location map (Figure 3.4). Though, the horizon map is very useful but it is important to remember that the interpolation is entirely dependent on the number of control points (or drill-holes). The plots (Figure 3.3 and Figure 3.4) show that the transition depths from the ejecta to Moenkopi are shallower (i.e. the ejecta blanket thickness decreases) as we move away from the center of the crater.

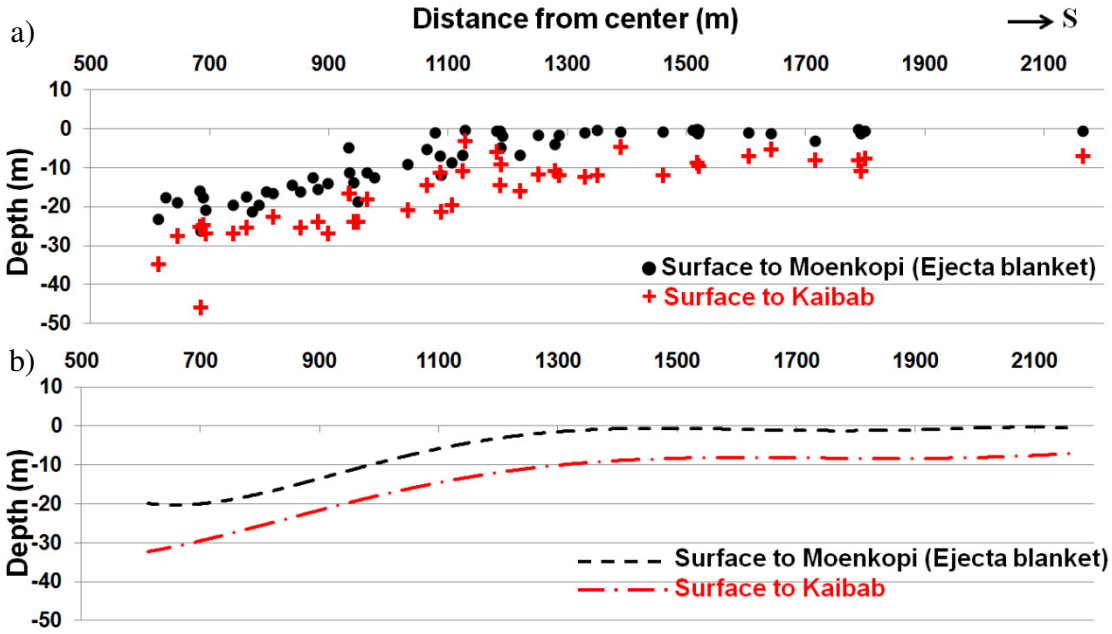

Figure 3.3. a) The transition depths – i) from the ejecta blanket to the bedrock Moenkopi, and ii) from the bedrock Moenkopi to the bedrock Kaibab are plotted using drill-holes from the southern flank of Meteor Crater (from the rotary drilling program by Roddy et al., 1975); b) The best fit lines for same two sets of transition depths are plotted.

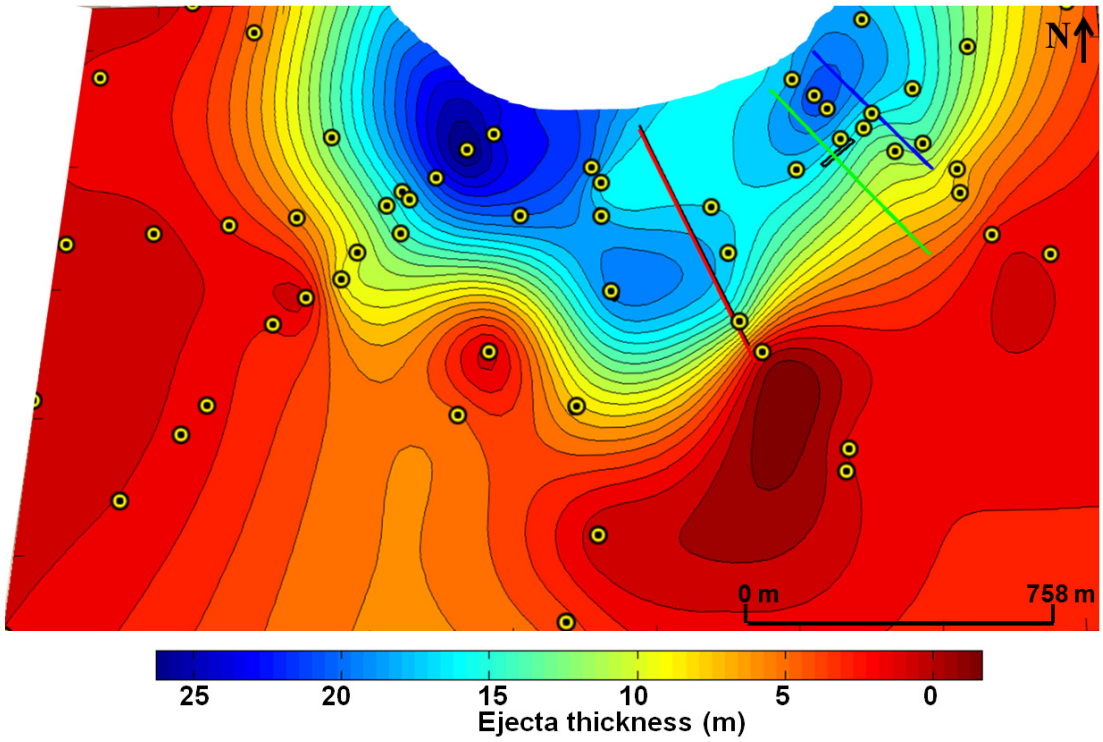

Figure 3.4. The contour map shows the transition (ejecta to Moenkopi) horizon overlain on the location map. The ejecta thickness is greater near the crater rim and decreases away from the rim.

3.4 Ultrasonic measurements

We have performed some bench-top measurements on the collected hand samples using ultrasonic transducers to have an initial idea about the velocities of the target lithologies and for future calibrations (Figure 3.5). We measured samples during the expedition (using portable V-meter) as well as at the Allied Geophysical Laboratories (AGL), University of Houston. During the field work, we were only able to measure P-wave velocities and measurements were less accurate. The probable reasons are:

1) the samples are weathered differently, 2) the samples are of irregular shapes, and 3) measurement errors (as we had to depend entirely on auto-analysis by the instrument). But, our measurements at AGL (measurement courtesy: Dr. Nikolay Dyaur) were very precise because we were able to: i) polish some surfaces of the samples for better coupling of transducers, and ii) measure both P- and S-wave velocities by analyzing seismic waveforms instead of depending on auto-analysis.

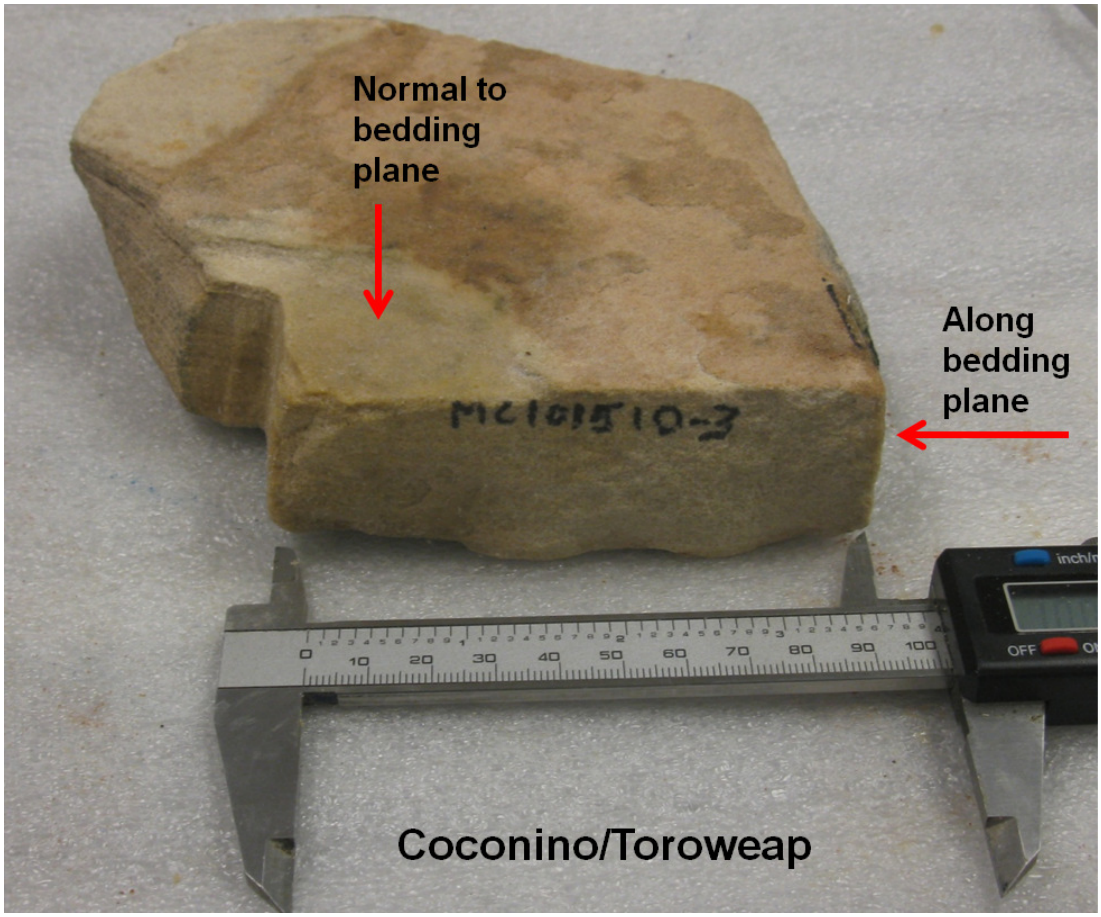

Figure 3.5. The Coconino/Toroweap hand sample during ultrasonic bench-top measurement at AGL, University of Houston. The bedding plane and normal to bedding plane directions are also shown.

The ultrasonic measurements of collected hand samples provide us seismic velocities which we can use as ground-truth and for calibrations along with estimated seismic velocities from seismic data. The precise measurement results at AGL, University of Houston has been provided in Table 3.1. The P-wave velocities vary from 2700-6100 m/s and S-wave velocities vary from 1700-3300 m/s. These ultrasonic measurements are stand-alone bench-top results as we are measuring some rock fragments at surface (atmospheric pressure) isolated from its actual framework. So, we expect these velocities to be different (faster) than the seismic results. We used the ultrasonic P-wave velocities in the Wyllie time-average equation (Wyllie et al., 1956) for 10% air-filled porosity. These calculated velocities with porosity drop significantly and become close to the range of velocities obtained by seismic analysis methods (Table 3.1).

<table>
<tr><th rowspan="2">Sample</th><th rowspan="2">Sample description</th><th colspan="2">P-wave velocity (m/s)</th><th colspan="2">S-wave velocity (m/s)</th></tr>
<tr><th>Along bedding plane</th><th>Normal to bedding plane</th><th>Along bedding plane</th><th>Normal to bedding plane</th></tr>
<tr><td>Moenkopi</td><td>From uplifted crater wall</td><td>4276 (1993)</td><td>3523 (1830)</td><td>2629</td><td>2538</td></tr>
<tr><td rowspan="2">Kaibab</td><td rowspan="2">From uplifted crater wall</td><td>5724 (2230)</td><td rowspan="2">5654 (2220)</td><td>3102</td><td rowspan="2">3266</td></tr>
<tr><td>6126 (2280)</td><td>3227</td></tr>
<tr><td>Coconino/ Toroweap</td><td>From ejecta blanket (SE side of crater)</td><td>2807 (1634)</td><td>2695 (1600)</td><td>1706</td><td>1771</td></tr>
</table>

Table 3.1. The table shows the ultrasonic bench-top measurement results for hand samples. The P-wave velocity values in brackets indicate the velocities obtained using Wyllie time-average equation with 10% air-filled porosity.

3.5 Seismic analyses and results

We performed the seismic survey in the southern flank of the crater (Figure 3.1). We used a truck-mounted 40 kg (88 lb) accelerated weight drop (AWD) as the seismic source for the N-S trending seismic line (AWD line). The receivers were planted vertical geophones having the natural frequency of 14 Hz. The AWD line is 645 m in length (216 receiver stations with 3 m intervals). The beginning of the AWD line is approximately 565 m from the center of the crater (hence, AWD line spans approximately 565–1210 m from the center of the crater). Details of the seismic survey and analysis of raw seismic shot gathers can be found in Roy and Stewart (2012).

One of the main goals of this study is to estimate high-resolution velocity structures (especially the S-wave velocity (V_S) structure). We applied surface-wave inversion (Multichannel Analysis of Surface Waves [MASW]) method for delineating V_S structure (Park et al., 1998; ibid, 1999; Xia et al., 1999). As discussed previously, MASW is a two-step process – i) generation of the dispersion curves (phase velocity versus frequency plots), and ii) inversion of the multimodal dispersion curves to estimate the near-surface V_S structure. The details of the multimodal MASW analysis for Meteor Crater site can be found in Roy and Stewart (2012).

MASW analysis is followed by P-wave refraction analysis. In this process, the first-break arrival times are picked from raw shot gathers providing initial knowledge of the P-wave velocities. Then, an iterative travel-time tomography (or inversion) is performed to estimate final V_P structure. It is important to note that for MASW, the inversion is performed based on observed dispersion curves whereas for P-wave analysis it is based on observed travel times.

The initial analysis of raw shot gathers brings up some important information. Figure 3.6a shows two example travel-time curves obtained from first-break pick analysis. One is from the beginning of the AWD line (or close to the crater rim) and another is from the end (or away from the rim). Similarly, two example dispersion curves (fundamental modes only) from the beginning and end of the AWD line are also plotted together in Figure 3.6b. Both plots show that the velocities (P-wave velocities from travel-time curves and surface-wave (Rayleigh-wave) phase velocities from dispersion curves) far away from the crater rim are much higher than those which are close to the rim. Since these same kinds of curves are later inverted to get velocity structures, we can expect to see higher velocities away from the rim in the final velocity structures. The dispersion curve, derived from the shot near to the rim, shows the loss of high-frequency content compared to that which is far from the rim. This loss of energy indicates that the unconsolidated near-surface close to the rim is more attenuative compared to the consolidated near-surface away from the rim. As discussed earlier (in Chapter2), the dispersion curves are dependent on the selected

offset ranges or spatial window. Figure 3.7 shows how the quality and structure of the dispersion curves change with the selection of the offset range. The dispersion curve shows that when very long offset is used (10.5-178.5 m), the curve becomes noisy, especially at higher frequencies (Figure 3.7a) whereas an optimum offset selection (10.5-82.5 m) produces a balanced dispersion curve (Figure 3.7b).

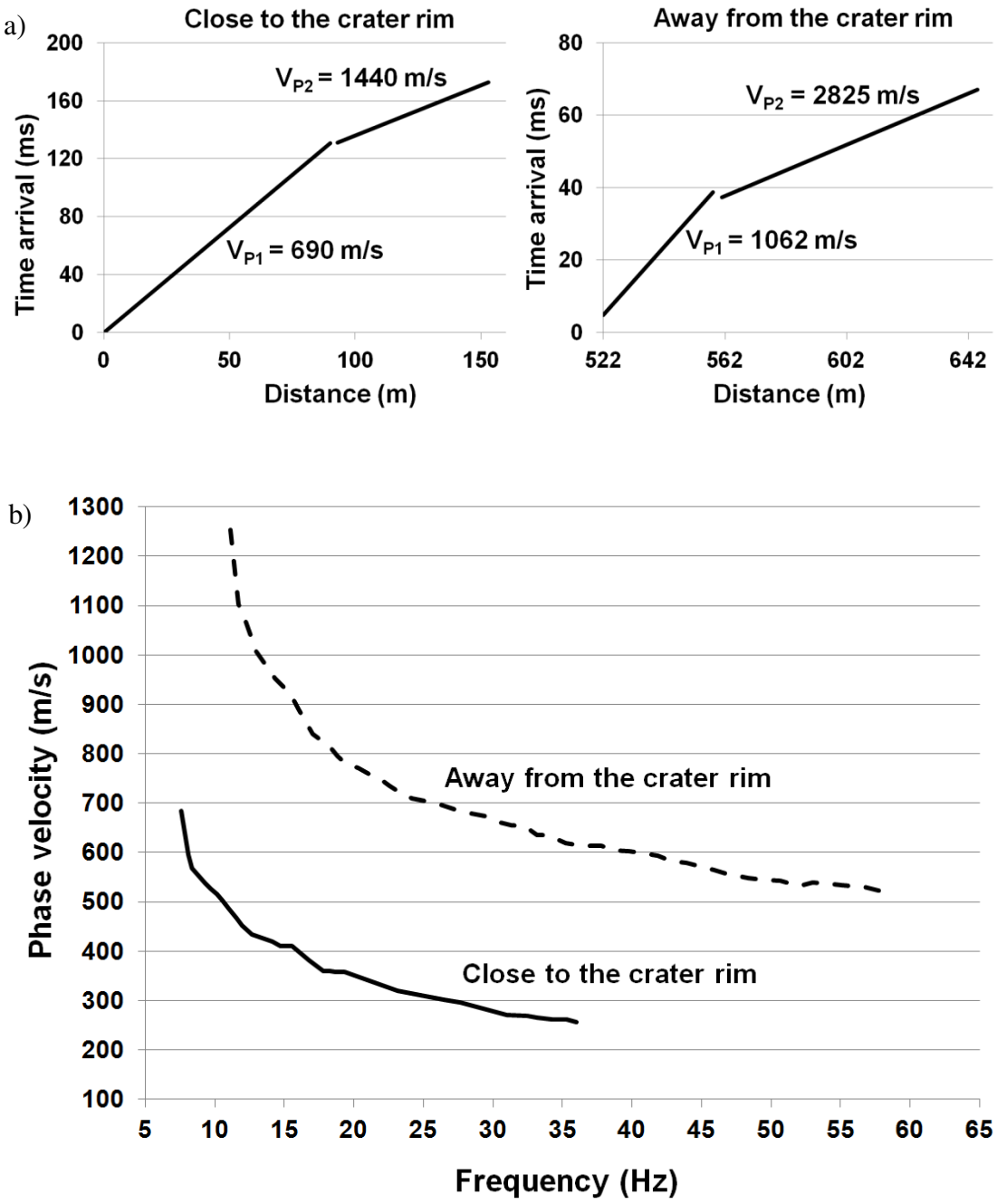

Figure 3.6. a) Travel-time curves (from first break picks) show shallow layers have higher P-wave velocities away from the crater rim, and b) dispersion curves (from surface-wave analysis) show higher surface-wave (Rayleigh-wave) phase velocities away from the crater rim.

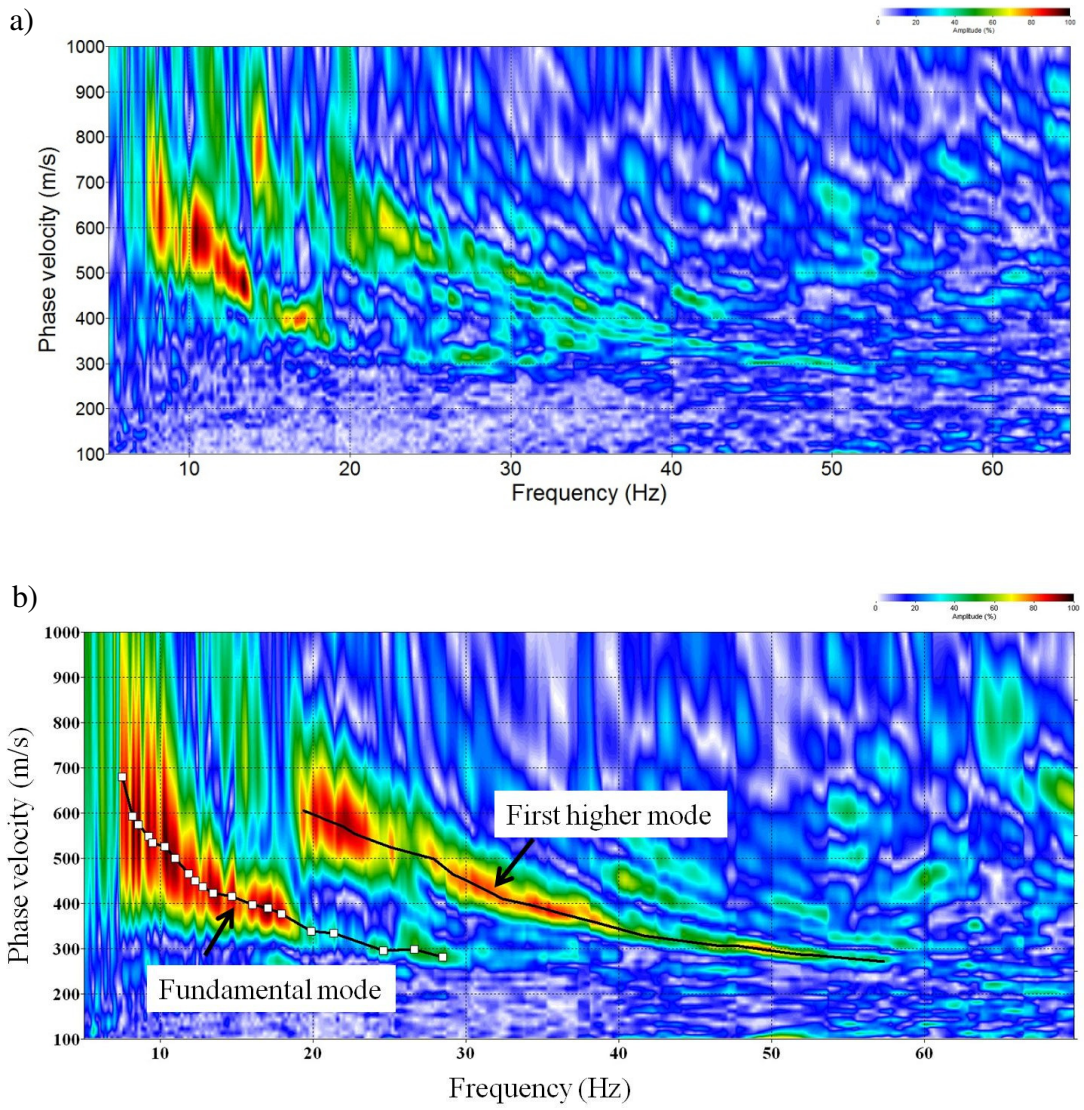

Figure 3.7. The figure shows – a) a noisy dispersion curve for an offset range of 10.5-178.5 m, and b) a well developed multimodal dispersion curve for an offset range of 10.5-82.5 m.

The 2D P-wave velocity structure for the 645 m long AWD line is determined (from P-wave refraction analysis using travel-time tomography). A minimum V_P of 450 m/s and maximum V_P of 3000 m/s have been assumed for a 55 m deep model during the

tomography analysis. These values are determined on the basis of the initial analysis of first-break picks for several raw shot gathers (Roy and Stewart, 2012). The final velocity structure for the AWD line shows the range of V_P values varying from 450 m/s to 2500 m/s up to 55 m depth (Figure 3.8a). The first observation that draws our attention is that low P-wave velocities are replaced by high P-wave velocities as we move away from the crater rim (towards south), as we anticipated. The 2D V_S structure (from MASW analysis) for the AWD line varies from 200-1000 m/s up to 38 m depth (Figure 3.8b). As we expected, S-wave velocities are low near the crater rim and replaced by high S-wave velocities away from the rim (similar to the V_P structure).

From the drill-hole results, we notice the similar thinning of the ejecta blanket away from the crater rim. As already mentioned, the ejecta blanket is unconsolidated mixed debris and it should have lower seismic velocities compared to consolidated bedrocks. So, the thinning of the low-velocity layers can be thought as the thinning of the ejecta layer. Finally, Figure 3.3 is overlain on the 2D P- and S-wave velocity structures (Figure 3.8a and 3.8b). A good matching trend has been observed between the thinning ejecta and thinning low-velocities. So, it can be concluded that the structure and thickness of the ejecta blanket have been successfully modeled by the seismic velocity analyses. Also, in addition to 1D drill-hole results, the ejecta thickness is identified along a 2D profile. The transition from the bedrock Moenkopi to the bedrock Kaibab has also been identified which is consistent with the drill-hole results.

Though, we always should consider the fact that the site is complex and local variations in the near-surface lithology is expected.

The Normal Move-Out (NMO) velocity (for P-wave) structure for top 1000 ms (Figure 3.9) has also been derived (Turolski, 2013). The velocity model from NMO analysis shows a similar increase of V_P values (especially for top 300 ms) away from the crater rim indicating the thinning of the ejecta blanket (as we identified previously). Those NMO velocities have been used to generate a near-surface CMP-staked section showing several sub-horizontal reflections. A structural interpretation of the stacked seismic section is shown in Figure 3.10. Four prominent horizons and probable faults can be identified from this initial stacked section (Roy et al., 2012 and Turolski, 2013). Probable stratigraphic boundaries are Kaibab/Coconino, intra-formational heterogeneities within Coconino, and Coconino/Supai. Faults are interpreted based on discontinuities in reflection events only. Since the resolution of the seismic image is too low (due to high attenuation caused my brecciated and complex near-surface), it is very difficult at this stage to identify the nature of the faults (normal or reverse). This important to note that the near-surface reflection analysis provides deeper information compared to travel-time tomography and surface-wave inversion methods.

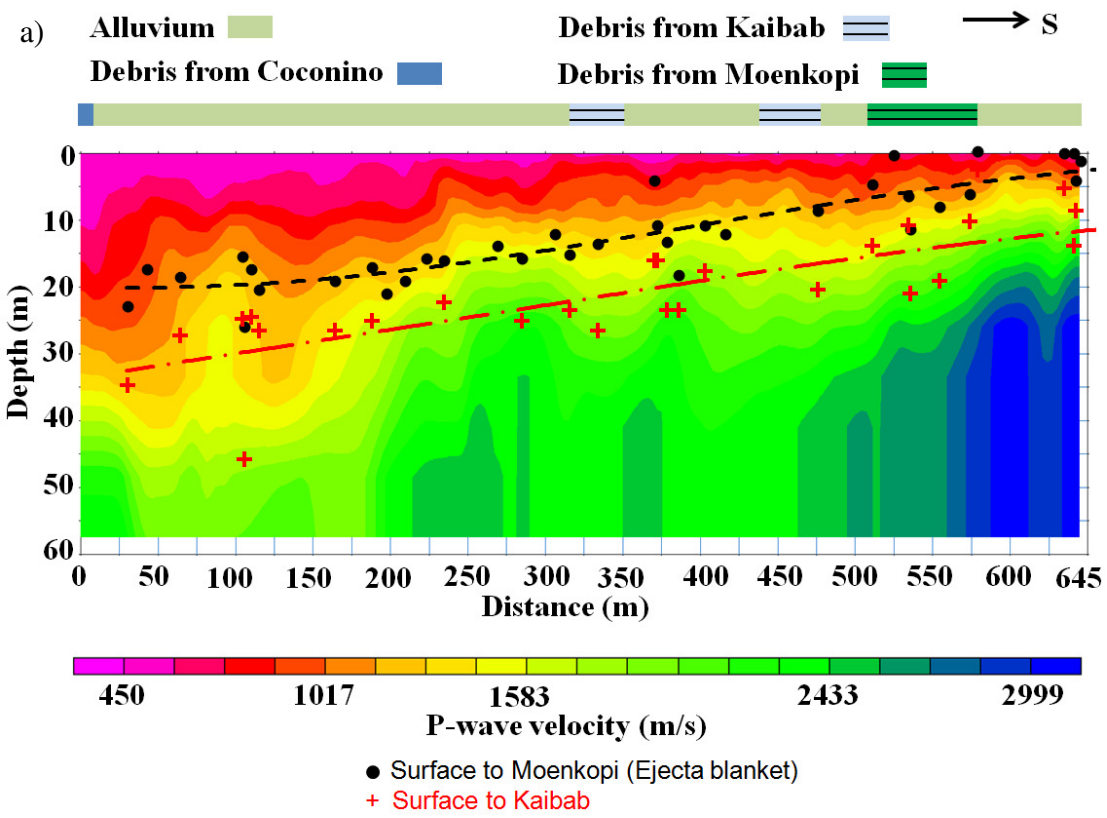
a)
Alluvium
Debris from Kaibab
S
Debris from Coconino
Debris from Moenkopi
Depth (m)
0
10
20
30
40
50
60
0
50
100
150
200
250
300
350
400
450
500
550
600
645
Distance (m)
450
1017
1583
2433
2999
P-wave velocity (m/s)
Surface to Moenkopi (Ejecta blanket)
Surface to Kaibab

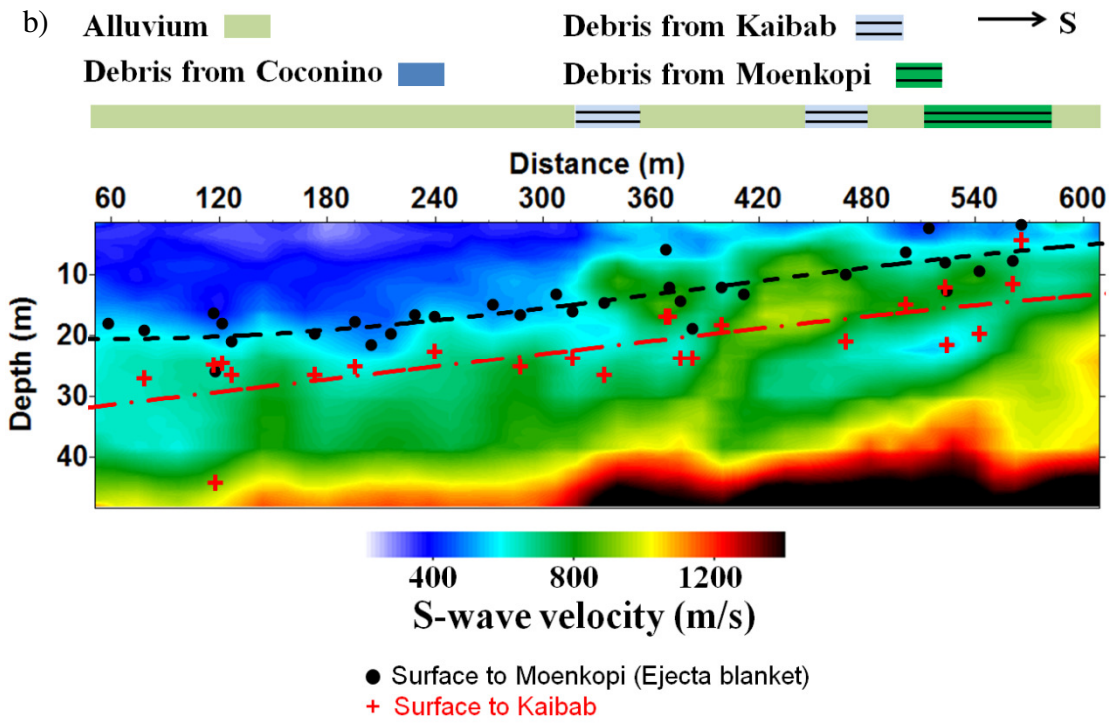

Figure 3.8. a) The 2D P-wave velocity structure (from refraction analysis) and b) the 2D S-wave velocity structure (from surface-wave inversion) along AWD seismic line. The transition depths (from ejecta to Moenkopi and Moenkopi to Kaibab) from drill-holes (Figure 3.3) are overlain on the velocity structures showing the thinning of the ejecta away from the crater rim (velocity profilesplotted from the ground surface: 0 m).

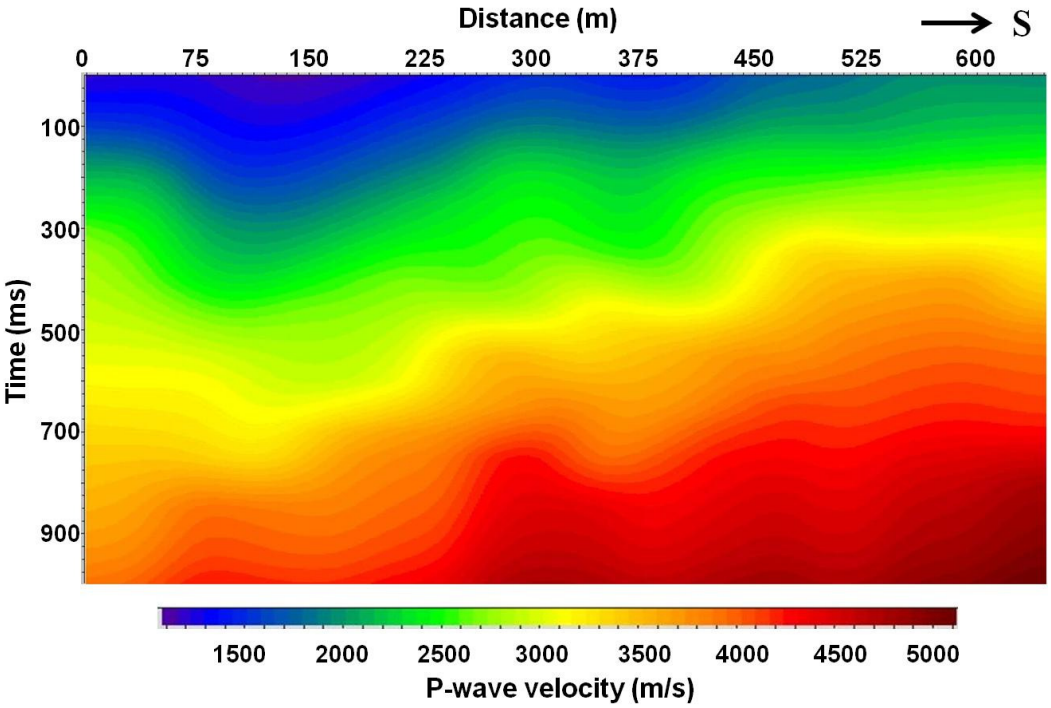

Figure 3.9. The P-wave NMO velocity structure along the AWD line (Roy et al., 2012 and Turolski, 2013).

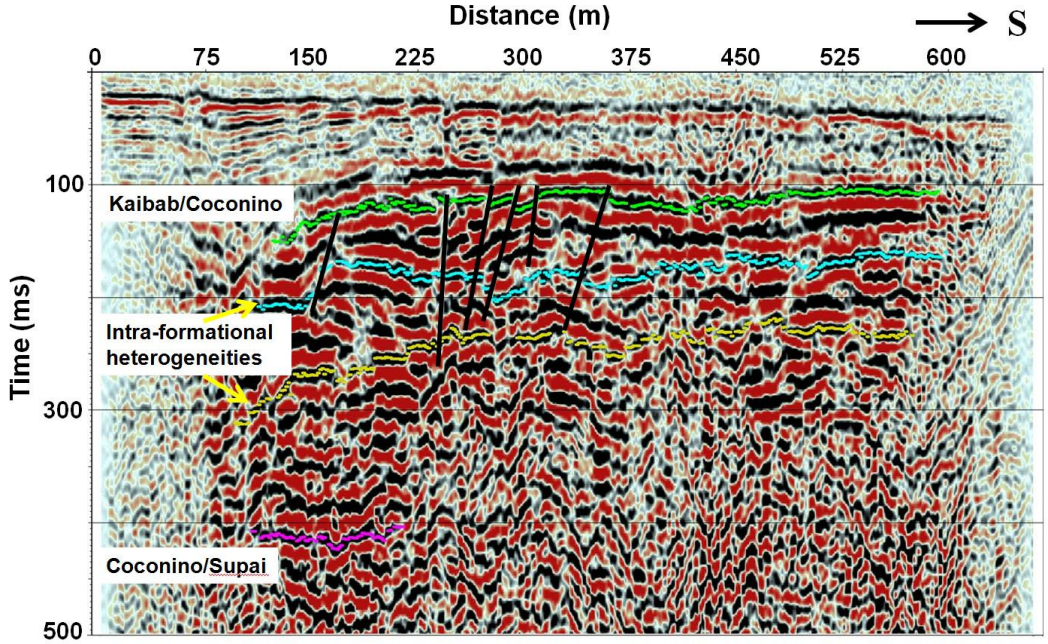

Figure 3.10. The CMP-stacked seismic section for the AWD line. Four reflector horizons are marked in different colors and interpreted faults are indicated with solid black lines (Roy et al., 2012 and Turolski, 2013).

3.6 Gravity survey and results

We also acquired gravity data along several lines in the southern flank of the crater (Figure 3.1a). We used Scintrex CG-5 gravimeter with station intervals of 30 m. The initial gravity results from Turolski (2013) are shown in Figure 3.11. The figure shows an initial drop in resultant gravity values possibly due to the effect of unconsolidated low-velocity ejecta layers, followed by an increase in gravity values due to the emergence of consolidated bedrocks and thinning of ejecta. The high gravity values near to the crater rim may be due to the increase in topography and existence of outcrops in the crater wall. Also, the effect of deeper subsurface structures can have an effect on the gravity results. A gravity modeling for the crater site can also be found in Turolski (2013) which shows a model response similar to the results obtained from different gravity lines. Further details of the gravity analysis can be found in Turolski (2013).

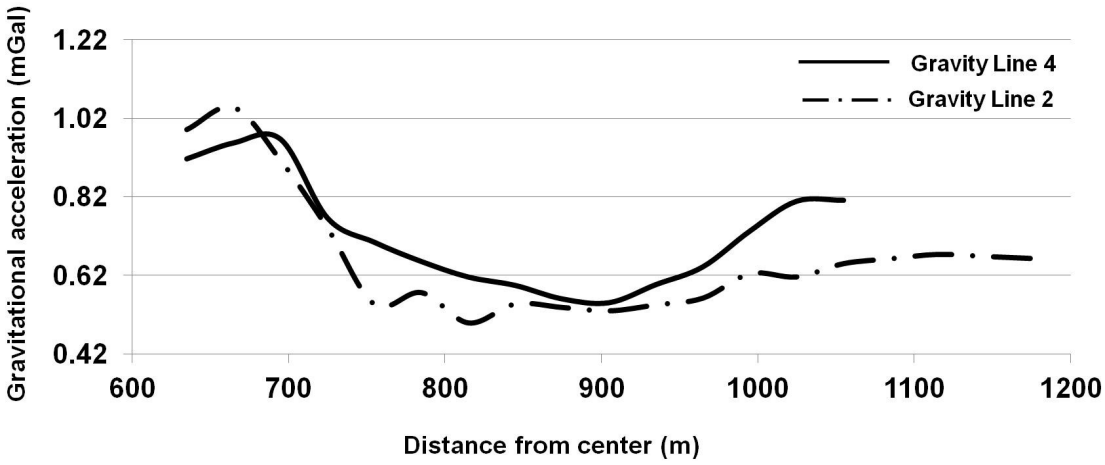

Figure 3.11. The residual gravity anomaly along radial gravity lines showing initial drop (due to ejecta effect) followed by increase in gravity values (bedrock).

3.7 GPR survey and results

The Ground Penetrating Radar (GPR) survey is located on the southeast flank of the Meteor Crater as well (Figure 3.1a). We used a 250 Hz Noggin system (common offset cart system) to acquire GPR data in the form of two swaths of 100 m x 4.5 m each. During GPR analyses, the main aim is to identify the reflectors generated due to the difference in subsurface electrical properties (dielectric contrasts). As relatively high-frequency GPR instrument was used, the depth of investigation is very shallow. Some initial analysis has been done for the GPR data acquired from the crater site. A 2D reflection profile (100 m long) is shown in Figure 3.12 (from personal communication with Susan Green, a graduate student at the University of Houston).

The profile has been generated using the processing steps as follow: i) temporal filtering to remove very low frequencies, ii) applying gain (spreading and exponential compensation) to enhance deeper signals, iii) background subtraction (spatial filter to enhance diffraction hyperbola and to remove horizontal noise and air/direct wave), and iv) time to depth conversion using a velocity of 0.096 m/ns. Several diffraction hyperbolas related to some point reflectors (most likely some fragments or blocks embedded in the ejecta blanket) have been noticed within the profile. A very shallow interface (at around 1 -1.5 m depth) shown by a yellow dashed line in Figure 3.12 has been interpreted as a probable change from the recent alluvium to other ejected materials. This initial GPR result shows that a very shallow high-resolution imaging of the complex near-surface at the Meteor Crater is possible.

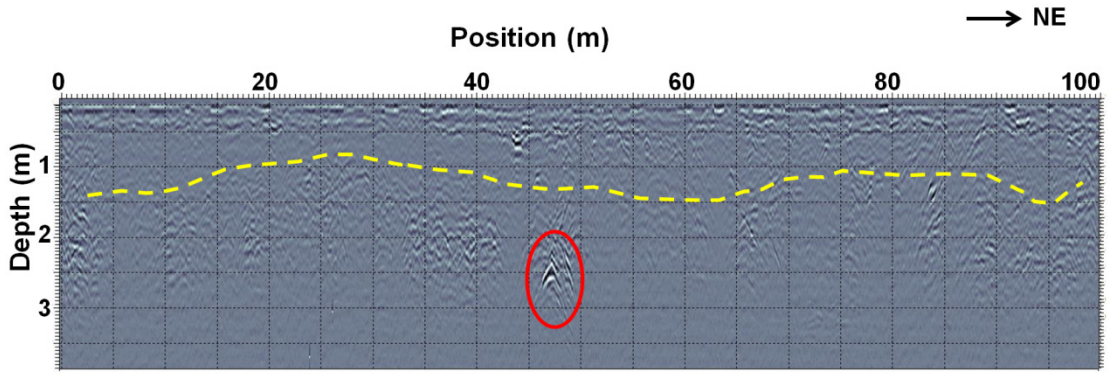

Figure 3.12. A 2D reflection profile from GPR survey shows the probable interface between recent alluvium and other ejecta materials (yellow dashed line) and a strong point reflector (red ellipse) probably related to some fragment or block embedded in the ejecta blanket (from personal communication with Susan Green, a graduate student at the University of Houston).

3.8 Conclusions

We acquired a suite of geophysical datasets at Barringer (Meteor) Crater. We analyzed these datasets (with emphasis on seismic methods) to build the near-surface geological model. We found P-wave velocities varying from 450 m/s to 2500 m/s for a 55 m deep earth model and S-wave velocities of 200-1000 m/s for 38 m deep earth model. A trend has been identified such as the low-velocity layers thin away from the crater. We interpret this as the expected thinning of the ejecta blanket. Drill-hole results show that the ejecta thickness is 15-20 m near the rim and decreases to 5m and less away from the rim. Thus, we have successfully modeled the ejecta blanket based on P- and S-wave 2D velocity structures and calibrating them with drill-hole results. We also measured velocities from ultrasonic experiments for different hand samples.

The P-wave velocities vary from 2700-6100 m/s and S-wave velocities vary from 1700-3300 m/s. After incorporation of a straightforward porosity effect, the ultrasonic velocities are comparable to the seismic estimates. Also, deeper stratigraphic boundaries and near-surface faults have been identified from the stacked seismic section (seismic reflection analysis). The gravity results also show similar ejecta thinning trend. This integrated approach shows that we have successfully imaged complex near-surface, from ultra-shallow (GPR analysis) to shallow (refraction and surface-wave analysis) and relatively deeper events (reflection analysis). Near-surface geophysical methods as outlined above may be useful in studying other impact craters (or any similar sites) with similar complex brecciated structures.

Chapter 4

Limitations of the surface-wave inversion method (MASW)

4.1 Introduction

The Multichannel Analysis of Surface Waves (MASW) is a popular frequency-based, surface-wave inversion method intended to estimate the near-surface shear (S)-wave velocities (1D and 2D), and to identify various subsurface features and geological structures (as discussed in previous chapters). Two main assumptions in the MASW method are: i) subsurface layers are horizontally layered (i.e. vertically heterogeneous), and ii) laterally homogeneous (e.g. no dipping layer or horizontal velocity variation). MASW input is a multichannel (or multireceiver) seismic gather and the output is 1D S-wave velocity structure which is positioned at the middle of the receiver spread used (Figure 4.1). Then, the next shot gather is processed and the above mentioned step is repeated. Hence, each resultant S-wave velocity structure is only influenced by the subsurface structures within that receiver spread (Luo et al., 2009a). Finally, all 1D velocity structures are merged (or interpolated) to provide the final 2D S-wave velocity (V_S) structure. So, the success of the MASW method is dependent on the extent of lateral heterogeneity within the active receiver spread. In

this study, we attempt to assess the limitations MASW may have when there is a lateral heterogeneity within the receiver spread (Figure 4.2).

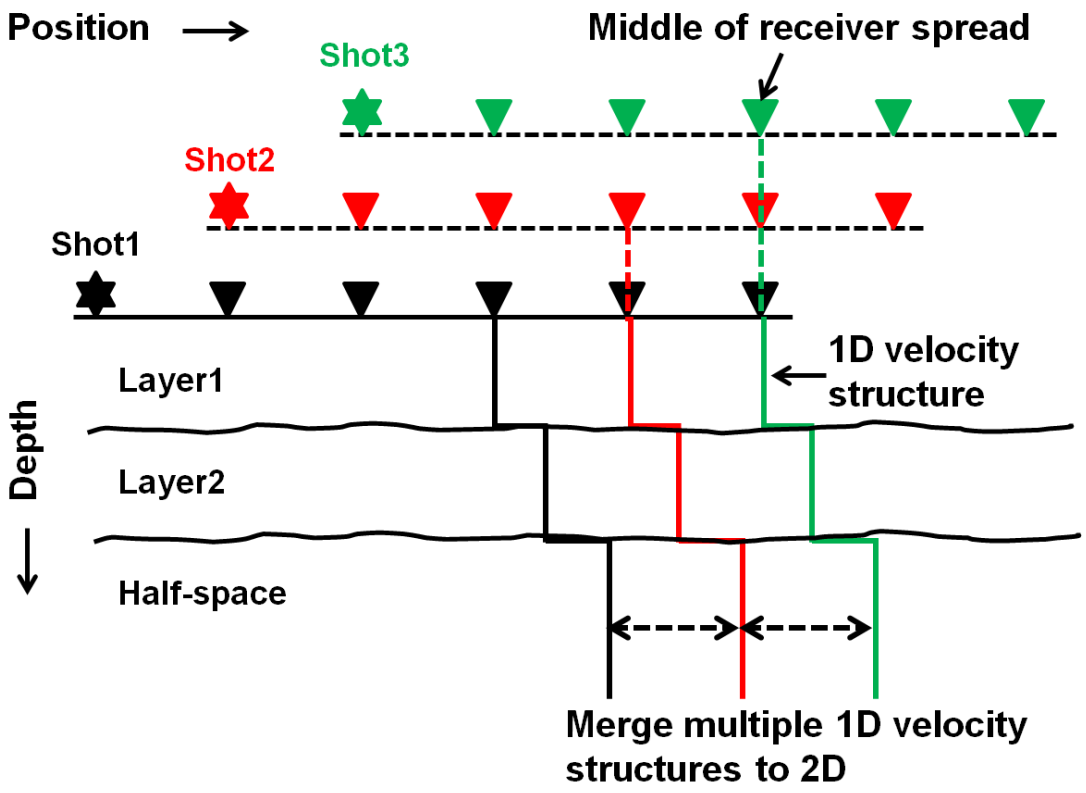

Figure 4.1. A schematic diagram shows that 1D S-wave velocity structures extracted from individual shot gathers, from MASW analysis, are positioned at the middle of corresponding receiver spreads.

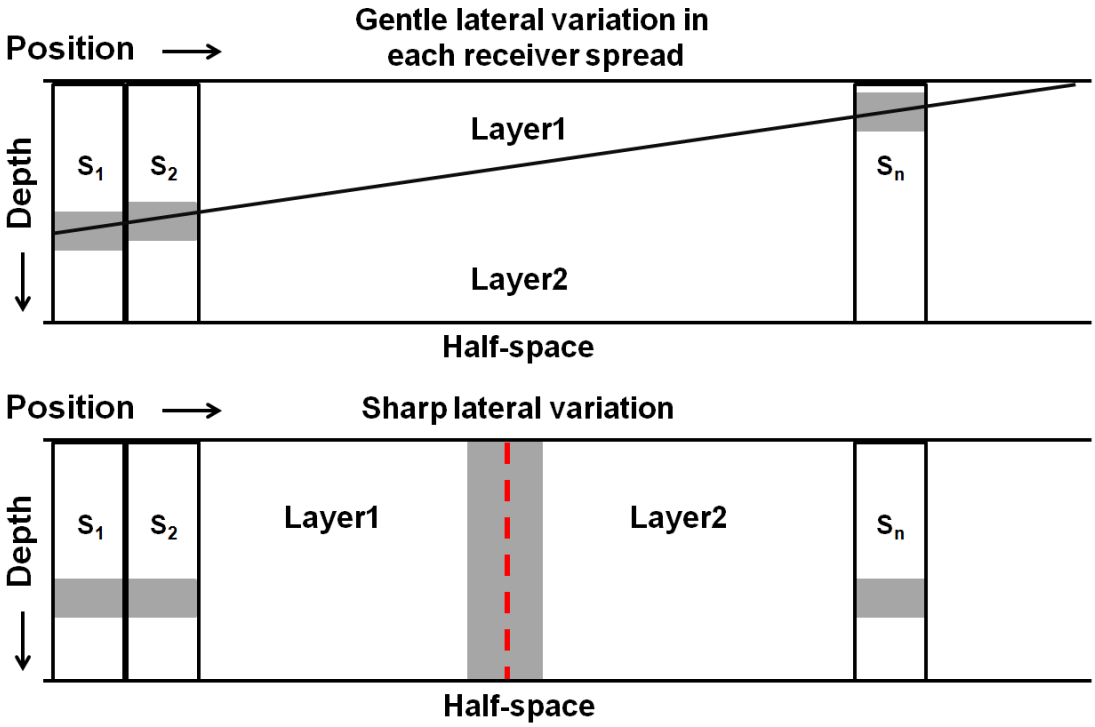

Figure 4.2. A schematic diagram showing gentle and strong lateral heterogeneities encountered in consecutive individual shots ($S_i = S_1, S_2,\ldots, S_n$) and related receiver spreads.

4.2 Gentle lateral heterogeneity case

The surface-wave inversion in laterally varying media is an important area of study (Luo et al., 2009b; Socco et al., 2009; Boiero and Socco, 2010) and should be dealt in details in future. We have analyzed datasets generated from numerical modeling to evaluate the gentle lateral heterogeneity case. Synthetic seismic data sets for a three-layered model are generated using an elastic finite-difference numerical modeling code for layered isotropic media (Manning, 2007; Al Dulaijan, 2008). The model

analyzed here has top two layers over a half-space (Figure 4.3). The interface between the top two layers has a 10º dip. The geometry consists of 401 stations with a receiver interval of 2.5 m, an explosive source at 2 m depth with Ricker wavelet signature of 30 Hz central frequency. Physical properties of the model are given as – Layer 1: V_P = 600 m/s, V_S = 300 m/s, density = 1.6 gm/cc; Layer 2: V_P = 1000 m/s, V_S = 500 m/s, density = 1.8 gm/cc; and Layer 3 (half-space): V_P = 1400 m/s, V_S = 700 m/s, density = 2 gm/cc. Densities of each layer are estimated using the Gardner's relation for P-wave.

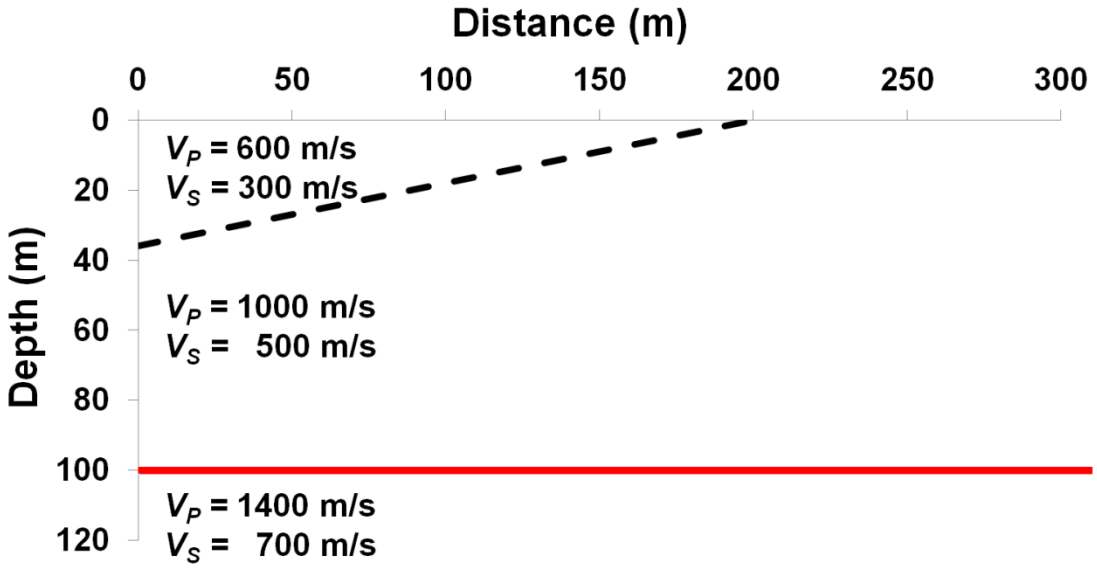

Figure 4.3. A schematic diagram showing a gentle dipping interface (10º) between two layers followed by a third layer (half-space). The model has been used for the numerical modeling experiment.

After careful offset analysis (Park et al., 2001; Park and Ryden, 2007; Park, 2011), 31 traces have been used to estimate the dispersion curves. The first dispersion curve for shot-1 (shot location: 0 m) shows more inclination towards the ground-roll phase velocities for the first-layer (Figure 4.4a). This is because the dipping interface is deeper here and ground-roll interacts more with the first layer. Then, the dispersion curve related to shot-4 (shot location: 120 m) shows average velocity values as ground-roll encounters both layer almost equally (Figure 4.4b). The dispersion curve is relatively noisy but not too contaminated. Figure 4.4c shows the dispersion curves which is related to a shot gather (shot-13 and location: 240 m) which is beyond the dipping zone, So, the ground-roll interacts only with the second layer and resultant phase velocity values are closer to that of the second layer. So, a smooth variation in phase velocities has been observed as shots move along the model (Figure 4.3). A scattering and averaging in phase velocities are observed (Figure 4.5). But, the effect is less stringent as the extent of lateral heterogeneity is mild.

The S-wave velocity structure is then estimated. The resultant S-wave velocity structure (Figure 4.6) shows a smooth change in velocities from 250-300 m/s to 450-500 m/s for the actual change of 300 m/s to 500 m/s for the first two layers. A smearing of velocities is observed along the dipping surface with smooth variation. But, the boundary is imaged more-or-less properly along the dipping surface (shown by black dashed line in Figure 4.6). The S-wave velocity model is required to be further updated for even better match. Though MASW analysis is affected by the

lateral heterogeneity, but the degree of effect is very mild for this gently dipping model. The overall performance of MASW is satisfactory, especially for imaging the dipping surface at its approximate proper spatial location.

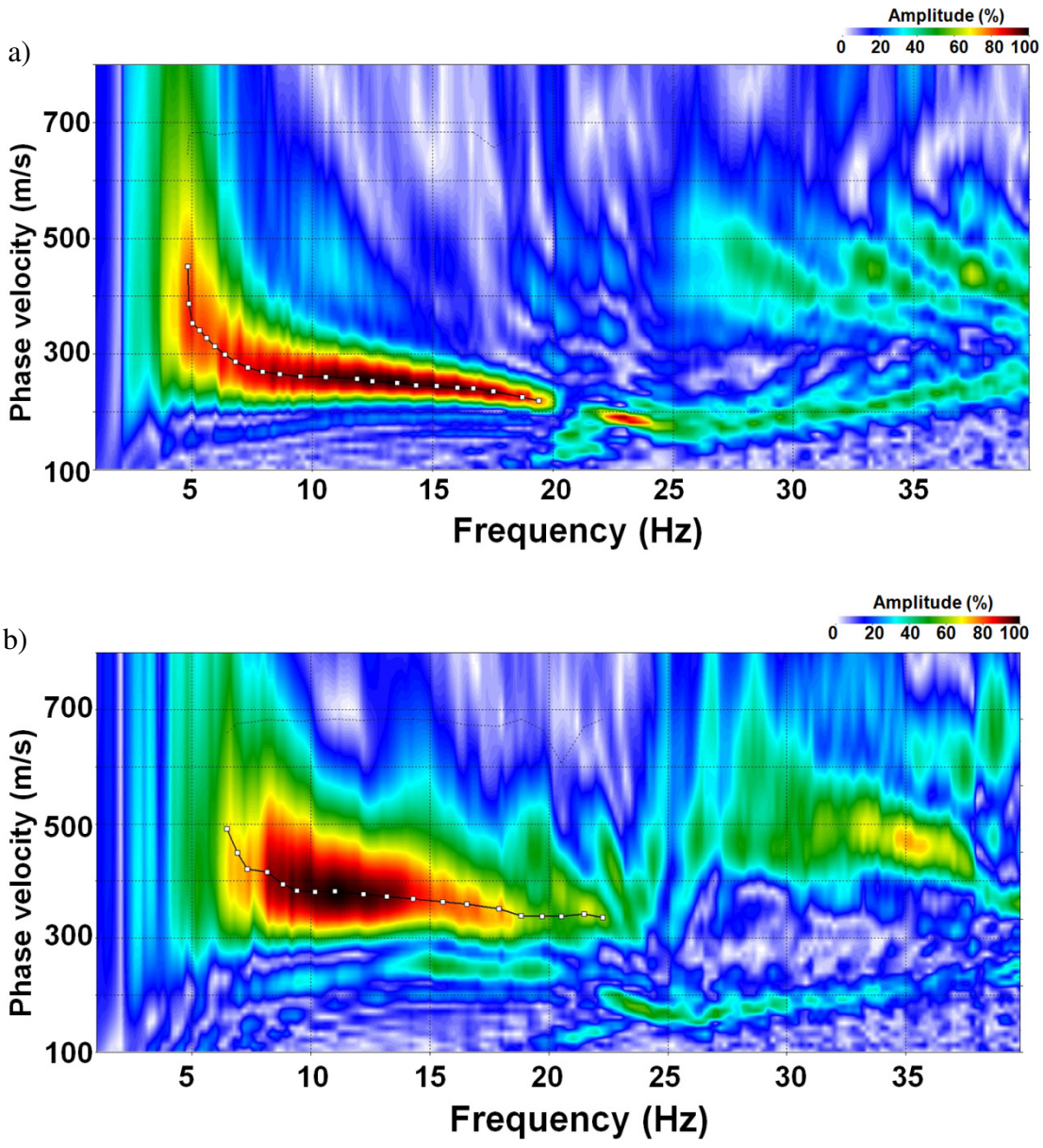

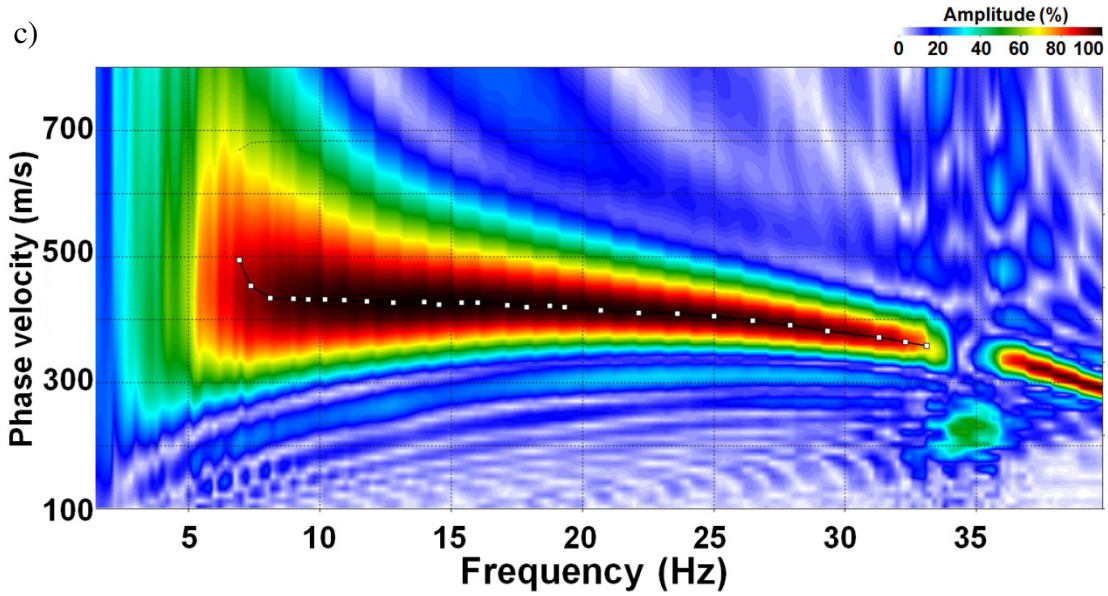

Figure 4.4. The dispersion curves for synthetic shot gathers (generated using the model in Figure 4.3) – a) from the beginning of the line, b) from the middle of the line, and c) from the end of the line.

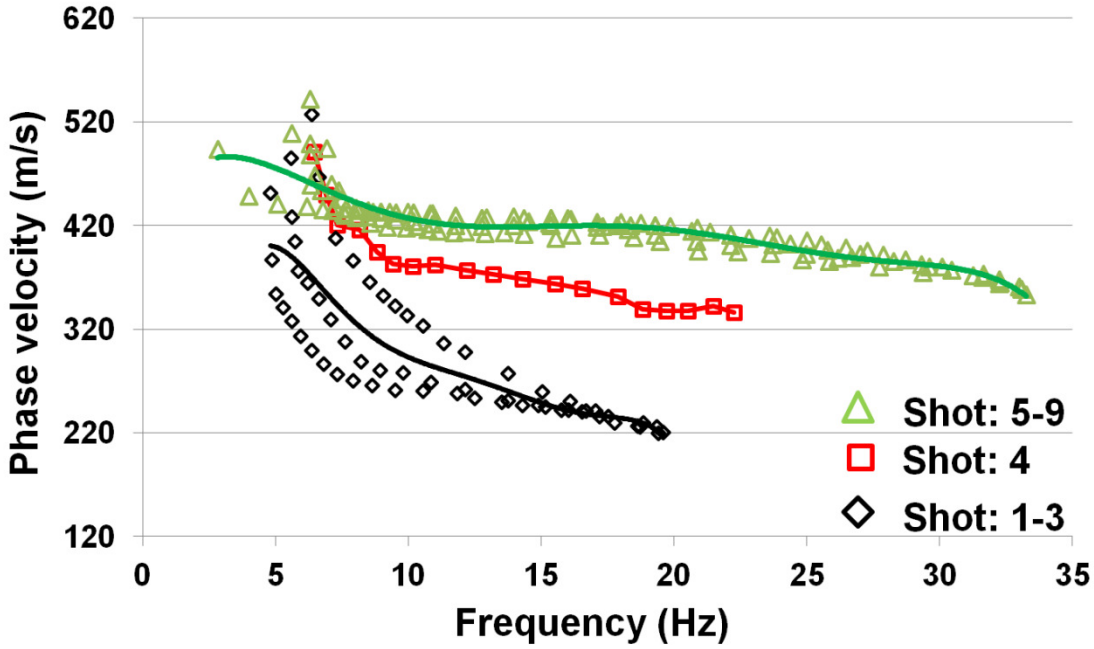

Figure 4.5. The picks from all dispersion curves (for nine shots along the model in Figure 4.3) plotted together. The best-fit lines are also plotted for batches of dispersion curves from - beginning (black), middle (red), and end (green) sections.

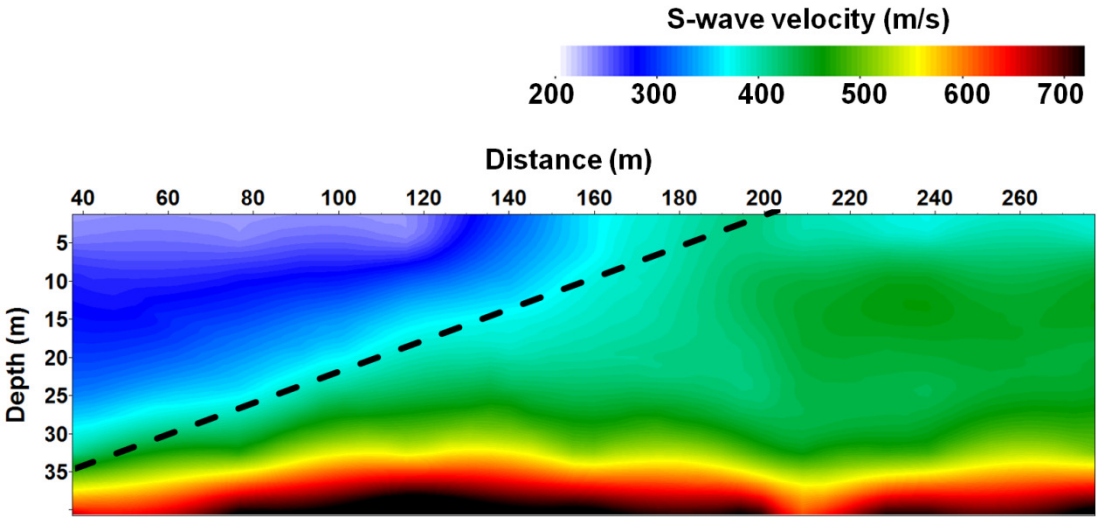

Figure 4.6. The 2D S-wave velocity structure estimated after MASW analysis from the synthetic datasets generated using the model in Figure 4.3.

4.3 Sharp lateral heterogeneity case

It is important to evaluate the response of MASW method if there is a sharp lateral change (e.g. lateral layers having moderate to high contrast in velocities, near-surface fault etc.) within the receiver spread patch. Two studies have been presented in the following sections: i) a physical modeling experiment, and ii) Hockley fault survey, Texas. Both cases involve steep lateral changes in material properties.

4.3.1 Physical modeling experiment and results

Physical modeling is often useful in providing a better understand in a complicated earth model situation. The advantages of the physical modeling experiments are: i) the intrinsic properties of constituent materials are known and the vibrations in materials are real, in contrast to numerical modeling, and ii) surveys in the laboratory

are less expensive, repeatable, and controllable than in the field (Stewart et al., 2013). A physical modeling experiment has been performed at the Allied Geophysical Laboratories (AGL), University of Houston using ultrasonic data acquisition system to assess a relatively complex situation (steep lateral heterogeneity case). An effort was made to prepare a model using a block of plexiglas and a block of aluminum. The velocities of the blocks are – i) plexiglas: $V_P \approx 2740$ m/s and $V_S \approx 1380$ m/s; and ii) aluminum: $V_P \approx 6300$ m/s and $V_S \approx 3100$ m/s. Two blocks are carefully merged together using adhesives, viscous couplant (honey), and firmly tied using clear tape to develop a laterally varying two-layer model having a vertical boundary with pseudo vertical fault like structure (steep lateral variation) at the conjunction of two blocks (Figure 4.7 and Figure 4.8). Then, the experiments were carried out to acquire seismic datasets with a roll-along source-receiver geometry configuration (Figure 4.8 and Table 4.1) using ultrasonic contact transducers (Table 4.1). We apply honey as a couplant between the transducers and blocks to enhance signal transmission. A scaling factor of 1:10000 for time and space is always used to upscale (or for frequency downscaling) to convert ultrasonic measurements as close as possible to seismic values on earth scale. So, for example 0.5 mm of receiver interval in physical modeling experiment is equivalent to 5 m for a real earth experiment.

a)

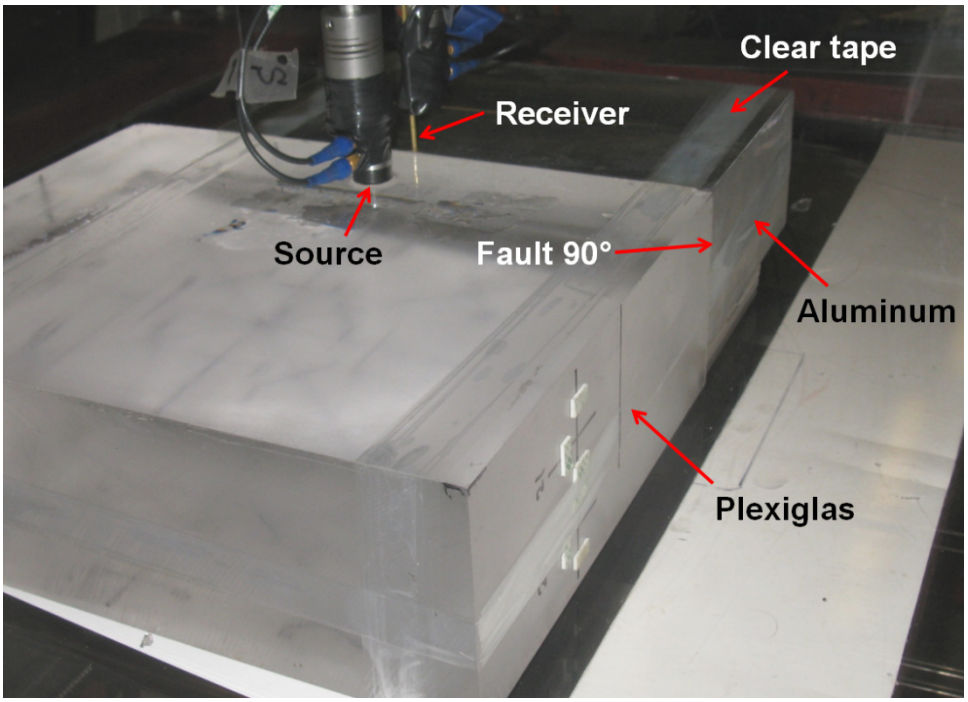

b)

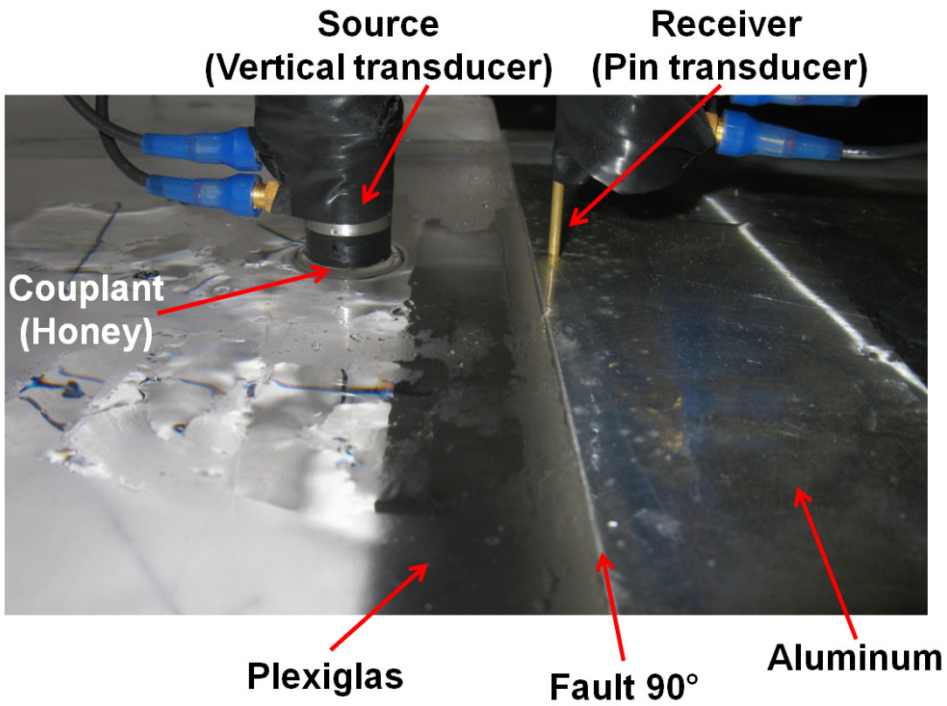

Figure 4.7. a) The ultrasonic physical modeling experiment set-up at the Allied Geophysical Laboratories (AGL) in the University of Houston, and b) the magnified view showing transducers at close range.

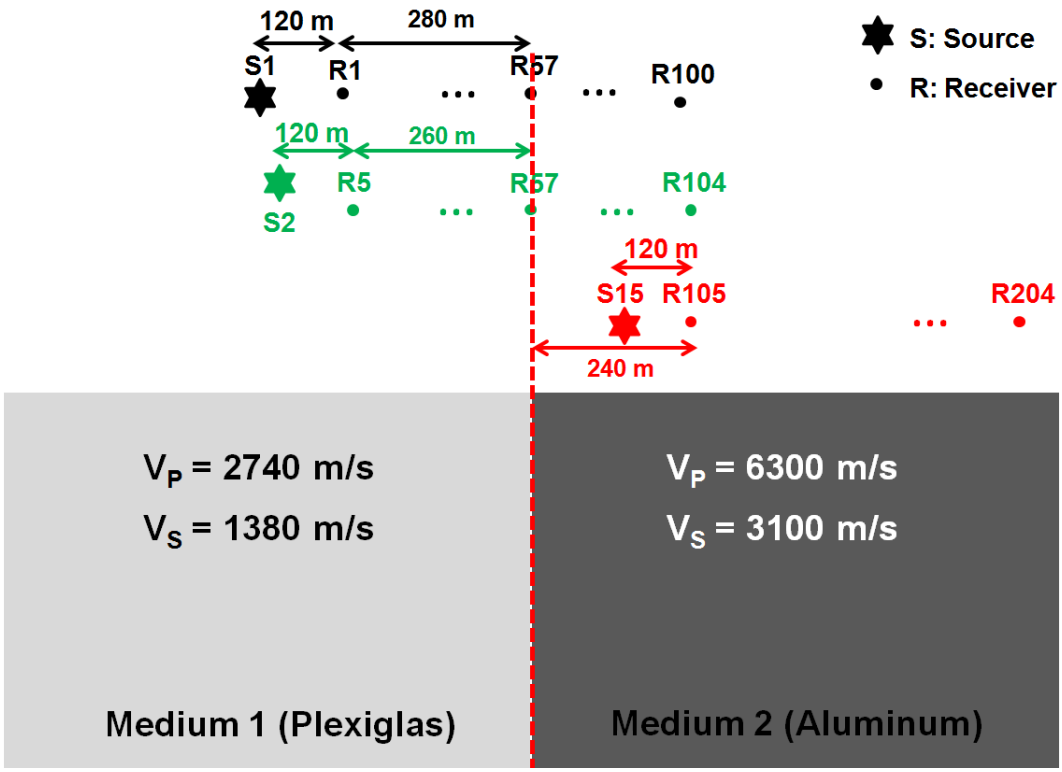

Figure 4.8. A schematic diagram showing the data acquisition configuration for the physical modeling experiment. The source-receiver configurations shift in a roll-along manner. The dashed red line shows the vertical interface between two layers.

Source type	1 MHz vertical transducer (Central frequency: 0.95 MHz)
Receiver type	Vertical pin transducer (Central frequency: 1.5 MHz)
Source to first receiver (Near-offset)	120 m (Before scaling: 12 mm*)
Source interval (Shot 1-9 and Shot 13-15)	20 m (Before scaling: 2 mm*)
Source interval (Shot 10-12)	40 m (Before scaling: 4 mm*)
Receiver interval	5 m (Before scaling: 0.5 mm*)
Number of receivers (for each shot)	100
Sample interval	1 ms

* A scale factor of 1:10000 used in these experiments

Table 4.1. Acquisition parameters for the physical modeling experiment.

We attempted to understand the effect of lateral variations in MASW analysis, hence we chose two blocks with sufficient variations in velocities. We can observe the non- (or very low) dispersive ground-roll (or surface waves) in the raw shot gathers as the materials are homogenous and not vertically layered (Figure 4.9). The first shot contains the receiver spread from receiver-1 to receiver-100 (R1-R100). The vertical boundary or fault is at around 280 m (receiver-57) from R1. So, we should expect some anomalous behavior around receiver-57 (R57). As anticipated, we can observe a strong reflection (and refraction) of ground-roll (along with other events) from the vertical boundary (Figure 4.9). This is the so-called back-scattering of the surface-wave which can be found in many land seismic datasets, and is a full study of its own. The back-scattering of ground-roll is evident in f-k plot of the raw shot gather as it dips in the opposite direction compared to other events for the end-on type of shot gather (Figure 4.10).

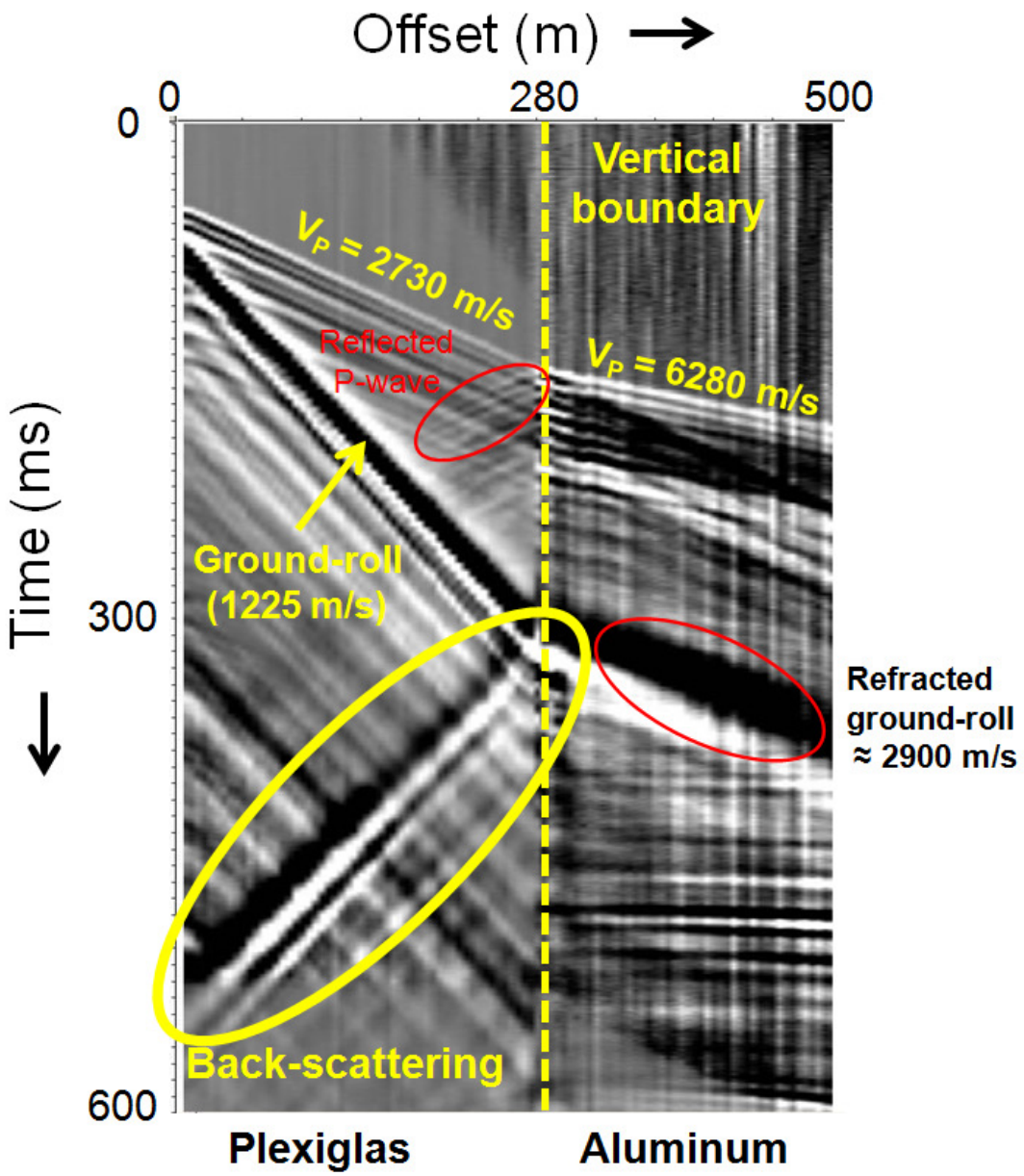

Figure 4.9. A raw shot gather from the physical modeling experiment dataset showing the reflection (or back-scattering) of the ground-roll (or surface-wave) along with other events (AGC applied for visual purposes only).

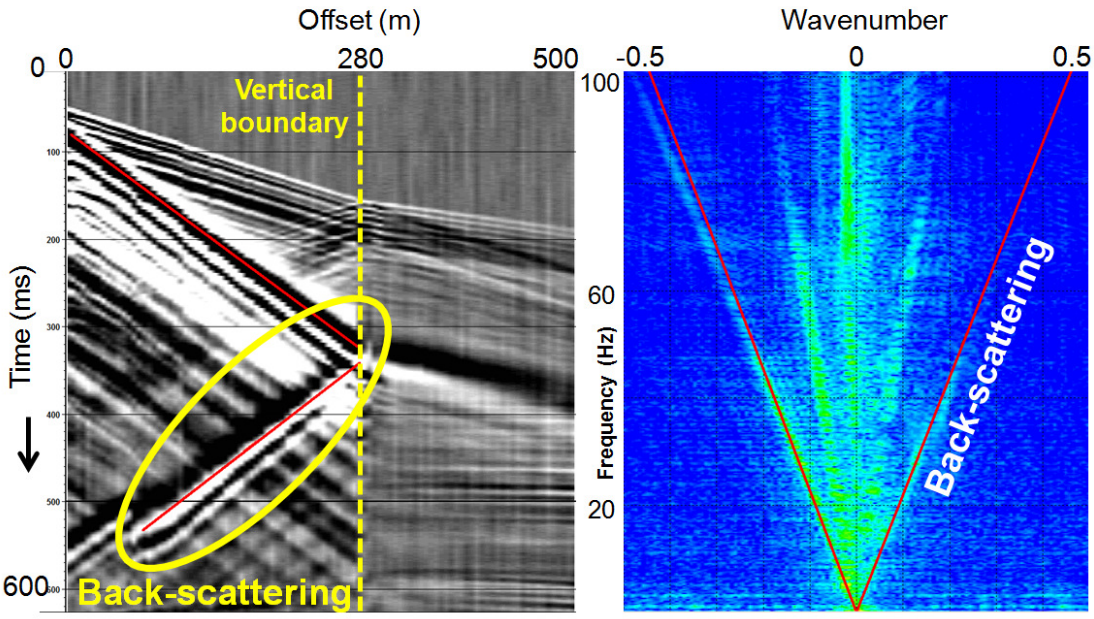

Figure 4.10. A raw-shot gather (left) same as in Figure 4.9 and its f-k domain representation (right) showing that the back-scattering event dips in the opposite direction for the f-k plot.

We then performed the MASW analysis on individual raw shot gathers. Only 30 traces or 145 m long receiver spread has been chosen for each shot gather after careful offset analysis to estimate less noisy dispersion curves (only fundamental mode in this physical modeling study). So, the traces used in MASW analysis for the first raw shot include only plexiglas information since we do not encounter the vertical boundary until 280 m. The resultant dispersion curve (Figure 4.11a and Figure 4.12) is mostly flat showing the non-dispersive nature for this homogeneous (both vertically and laterally) receiver spread portion of plexiglas. In the similar fashion, we get relatively flat dispersion curves for next seven shots i.e. from shot-2

to shot-8 (only two traces from aluminum part across the vertical boundary for 8th shot).

Then, from shot-9 to shot-11, the vertical boundary is encountered within the used receiver spreads. The effects of this heterogeneity are evident from the noisy dispersion curves (Figure 4.11b and Figure 4.12). The resultant dispersion curves in this anomalous zone are dependent on the contribution of number of traces from each material. For shot-9, the number of traces from the plexiglas zone is 25 and those from aluminum zone are only 5. So, the dispersion curve is more weighted towards the ground-roll phase velocity of plexiglas (green triangles in Figure 4.12). But for shot-10, traces from plexiglas zone are 17 and those from aluminum are 13. So, almost equal contribution from each zone has been observed and picks of dispersion curves are distributed between two extreme ground-roll phase velocity boundaries (red crosses in Figure 4.12). For shot-11, traces for plexiglas are 9 and those for aluminum are 21. So, the dispersion curve is shifted towards the ground-roll phase velocities of aluminum (black stars in Figure 4.12).

The dispersion curves became relatively flatter again when the receiver spread zones pass the anomalous zone and enter into the homogeneous (both vertically and horizontally) aluminum block (Figure 4.11c and Figure 4.12). This analysis shows that MASW is only sensitive to the structures related to the used receiver spread. The

results are noisy and dependent on the amount of contribution of different materials within the receiver spread zone if any sharp variation is present.

a)

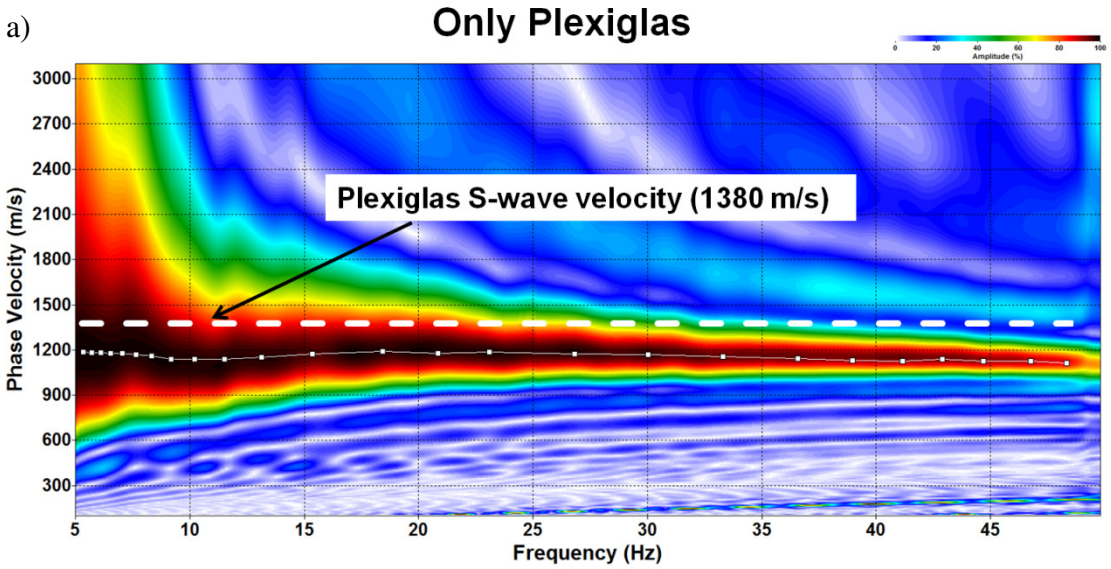

b)

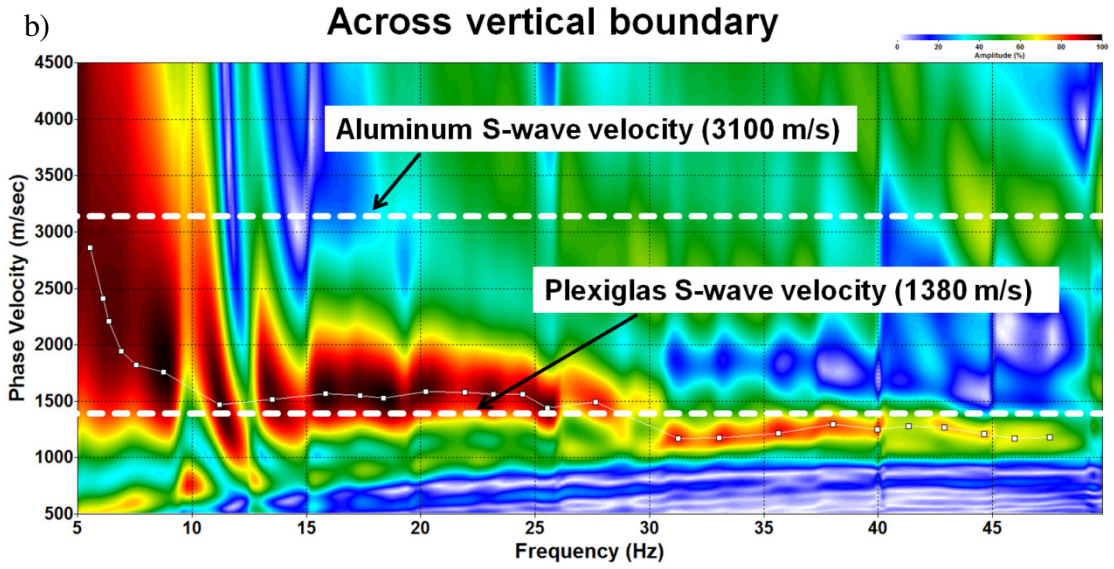

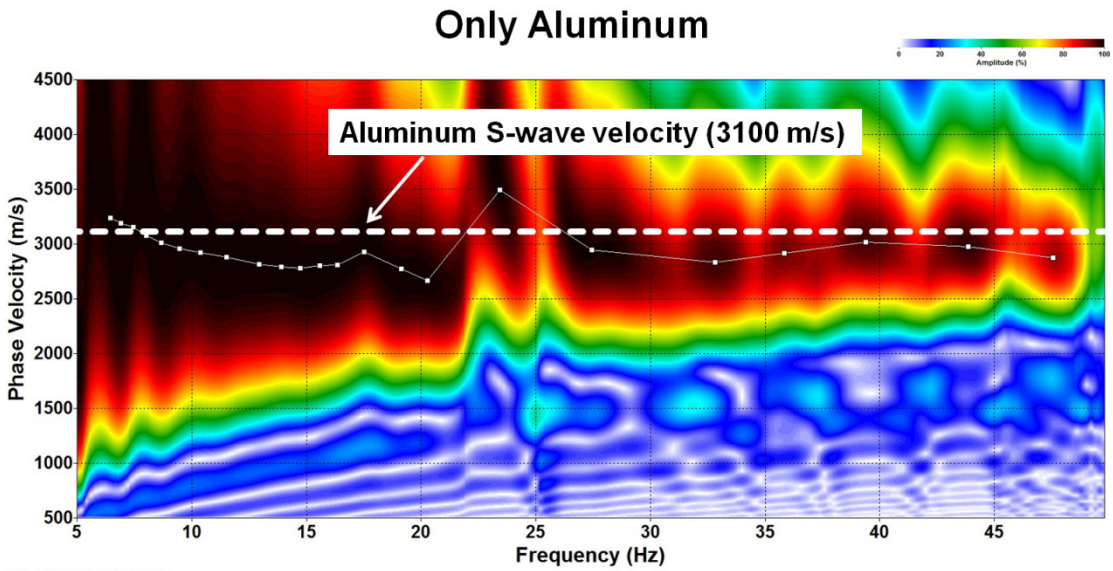

Figure 4.11. The dispersion curves for the shot gathers from – a) only plexiglas part (shot-1), b) across vertical boundary (shot-10), and c) only aluminum part (shot-15).

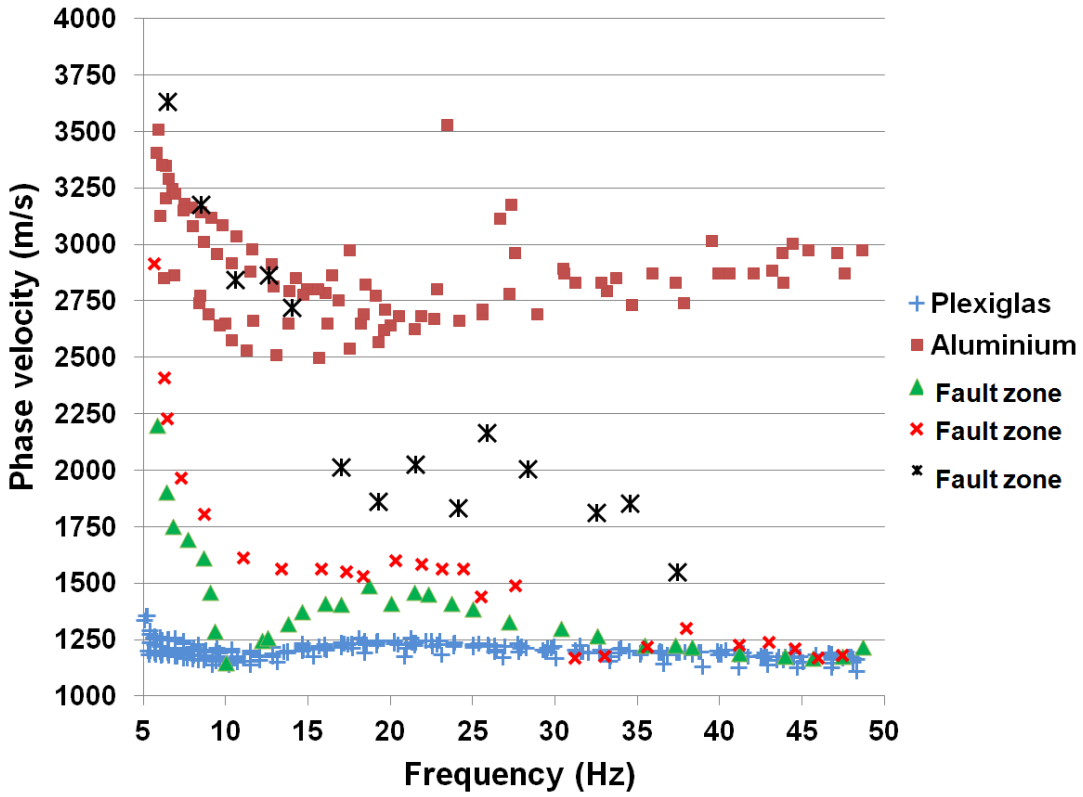

Figure 4.12. The picks from all dispersion curves for fifteen shot gathers plotted together.

We continued to apply the MASW analysis and generated the 2D S-wave velocity structure along the model. Figure 4.13 shows the estimated 2D V_S structure. The velocity model is relatively smooth in the only plexiglas region and resultant velocity (1400 m/s) is very close to the S-wave velocity of plexiglas (1380 m/s). But, an anomalous zone has been encountered around the vertical boundary. The vertical boundary (or pseudo-fault) zone is broader (instead of sharp) and velocity structure is not smooth and values are mixed. The velocity structure becomes smoother again when only aluminum zone is encountered and the S-wave velocities (3000-3100 m/s) are also close to the S-wave velocity of aluminum (3100 m/s). So, MASW is a good tool to identify laterally homogenous media; but it is compromised in the sharp laterally variable zone. While positioning the anomalous zone in the proper location, the velocity results are mixed and smeared.

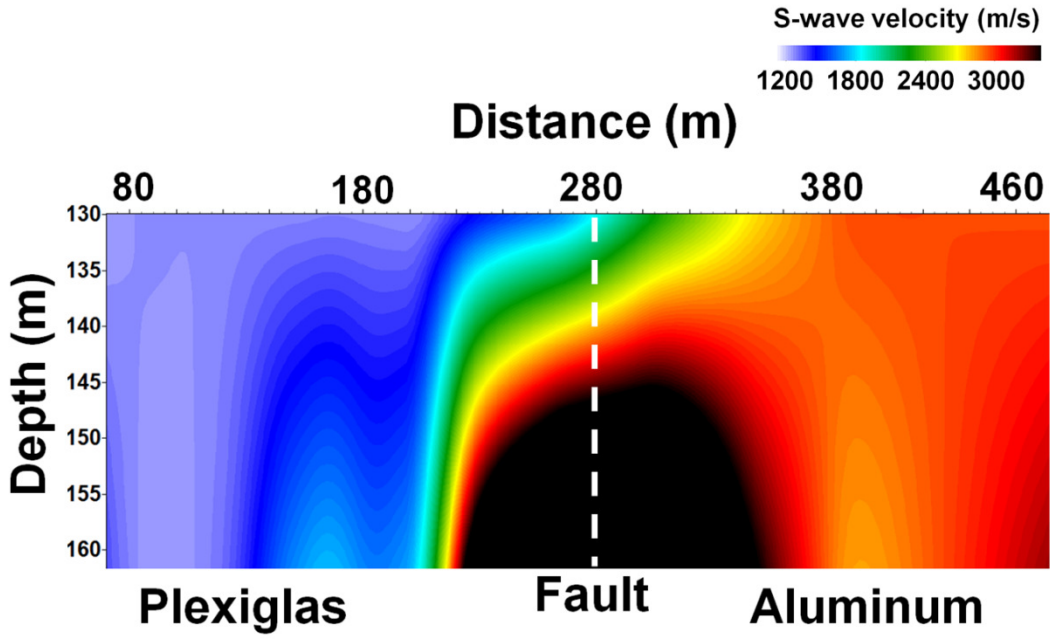

Figure 4.13. The 2D S-wave velocity structure for the physical modeling experiment.

4.3.2 Hockley fault survey and results

We next analyze a field seismic dataset related to the Hockley fault system (Figure 4.14a) in Texas (near Houston) having a sharp lateral heterogeneity along our seismic survey line. The coastal region of Gulf of Mexico, particularly in the Houston area contains more than 300 active faults including the Hockley fault system (Engelkemeir and Khan, 2007, Khan et al., 2013). The dip of the fault is steep with approximately 70° (Khan et al., 2013) towards the SE and in many cases extended up to surface.

The coastal plain bordering the Gulf of Mexico is underlain by a thick sequence of largely unconsolidated deposits of clays and sands. Growth faults are common throughout these unconsolidated sediments. Such sediments near shelf margins are usually good candidates for faulting; especially in environments where continuous deposition activities prevail. Within the Harris County area, three main near-surface geologic formations are present: Willis, Lissie, and Beaumont. The contact between these formations is a weak zone, and some of the normal faults are formed at the contacts between these formations. The Hockley fault makes a clear boundary between the clay-dominated Willis formation (upthrown block) and sand-dominated Lissie (downthrown block) formations (Otoum, 2011).

For the 2D seismic survey, we used a vibroseis truck as seismic source to acquire data along a 1075 m line using 216 vertical geophones with 5 m receiver interval. The main fault is located at 325 m from the beginning of the seismic line (Figure 4.14b).

For the vibroseis, we used sweep length of 12 s with a linear sweep of 10-150 Hz. The main fault scarp is located in highly populated area and intersects Highway 290. The raw shot gathers are contaminated with strong low frequency noise from the highway traffic.

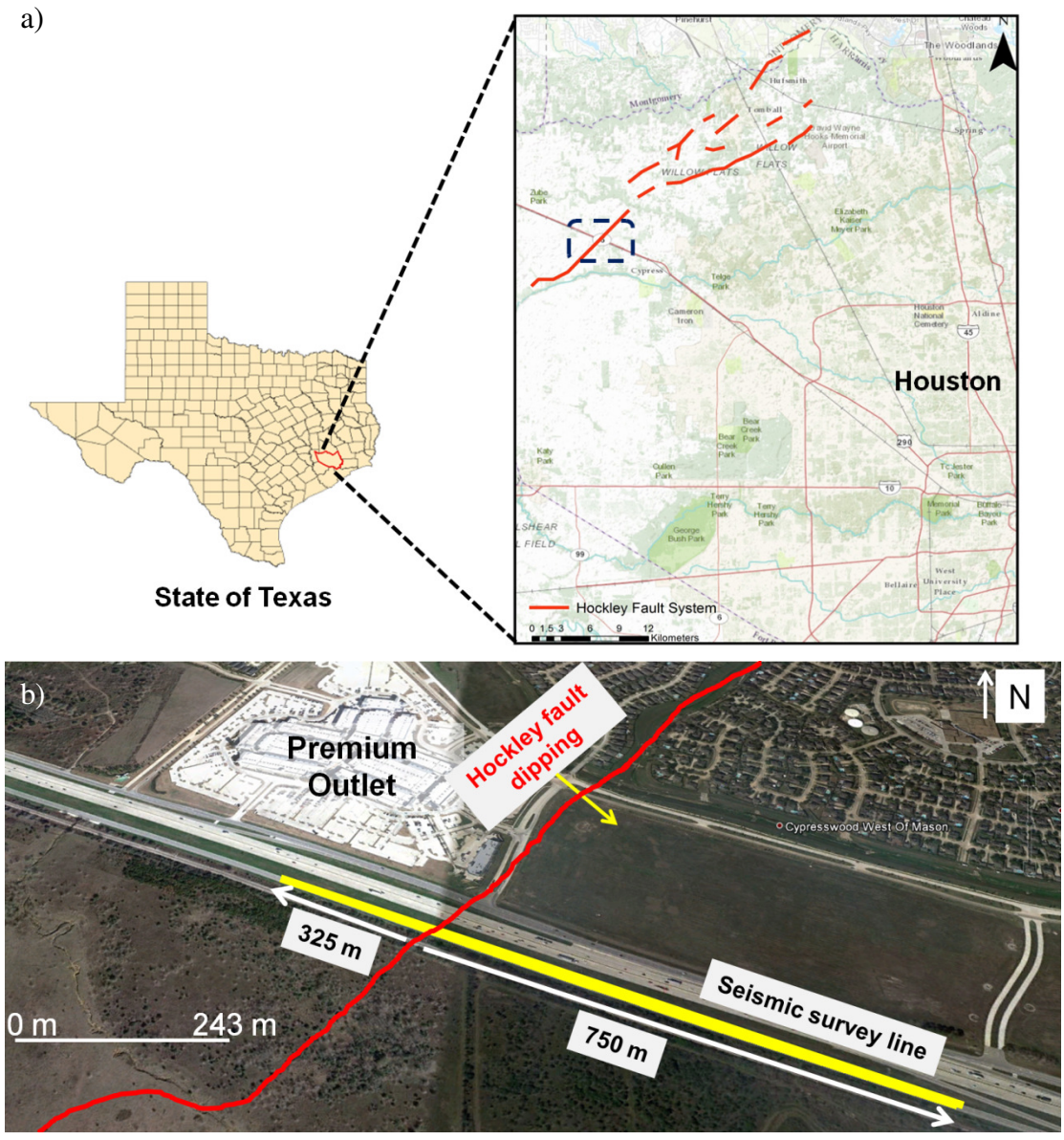

Figure 4.14. a) The location of Hockley fault system, and b) the seismic survey configuration across a fault scarp.

The traditional MASW analysis has been performed to generate the 2D S-wave velocity structure. Figure 4.15 shows the 2D S-wave velocity structure for Hockley fault survey. The highly attenuative near-surface, low-frequency noise, and lack of lower frequencies (below 10 Hz) due to the used seismic sweep range restrict the resultant velocity structure to shallow depths. S-wave velocities vary from 200-32m m/s for only 10 m deep model. We found a noisy, anomalous zone in the 2D profile near the fault location, but with poor resolution. Near-surface reflection seismic analysis provided the CMP stacked section (from personal communication with Mr. Eray Kocel) which shows multiple discontinuities (possibly near-surface faults) along the seismic line. The S-wave velocity structure correlates well with those anomalous zones, especially with the main fault. So, MASW can be used to identify fault zones but some smearing is expected around the fault zone.

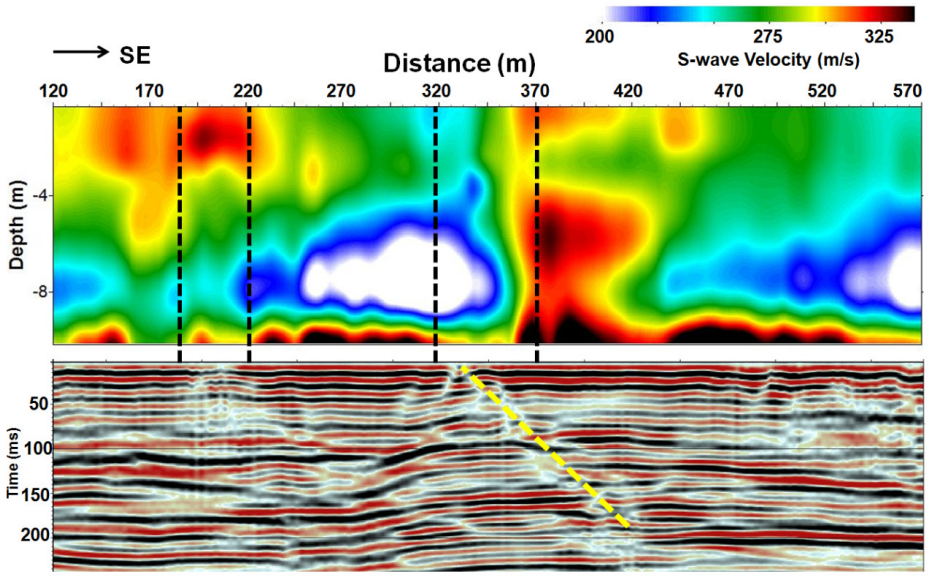

Figure 4.15. The 2D S-wave velocity structure for the Hockley fault survey showing anomalous zone across the main fault in the survey area (plotted from the ground surface: 0 m).

4.4 Conclusions

We have evaluated the effect of lateral heterogeneities on MASW analysis using numerical simulation, a physical modeling experiment, and the Hockley fault survey, Texas. We have successfully identified the S-wave velocities for the numerical simulation experiment with gentle lateral variation. The resultant S-wave velocity structure shows a smooth change in velocities from 250-300 m/s to 450-500 m/s for the actual change of 300 m/s to 500 m/s for the first two layers. A smearing of velocities is observed along the dipping surface with smooth variation. Still, the boundary is imaged more-or-less properly along the dipping surface. We have found S-wave velocities of 1400 m/s for plexiglas (actual value 1380 m/s) and 3000-3100 m/s for aluminum (actual value 3100 m/s) in the final S-wave velocity structure after full MASW analysis. But, the velocities are mixed across the vertical boundary between two blocks. Similarly, S-wave velocity structure (varying from 200-325 m/s for 10 m deep model) shows noisy, mixed velocity values near the main fault area for Hockley fault survey. We can conclude that MASW can identify the proper zones of lateral variations spatially but resultant S-wave velocity values around those zones are adversely affected.

Chapter 5

Basic full-waveform inversion

5.1 Introduction

We have used a popular frequency-based surface-wave inversion method, Multichannel Analysis of Surface waves (MASW), to estimate the near-surface S-wave velocities (1D and 2D). But, the MASW method has some inherent limitations. As previously discussed, the main assumption in the MASW method is that subsurface layers are considered to be horizontal (i.e. vertically heterogeneous) and laterally homogeneous. The resultant 1D S-wave velocity structures from MASW for individual shot gathers are smoothed average velocities of the subsurface regions over the individual receiver spreads. This becomes approximate if there is a lateral change in velocities within that receiver spread. One practical way to handle this problem is to select shorter receiver spreads. But, the problem still persists if there is a significant change in material properties e.g. a near-surface fault, cavity etc. Also, if the input receiver spread is too short then it may lead to the generation of a poorly developed dispersion curves which suffer from noise problems. The length of the receiver spread and the resolution of the dispersion curve will depend on the seismic acquisition geometry. If the receiver intervals are small (2-5 m) then better resolution is anticipated compared to larger receiver intervals (20-30 m). This thesis work has a

goal to apply the surface-wave inversion method towards the exploration seismology (e.g. S-wave statics calculation). But, for the industry standard, the receiver interval of 20-30 m is very common. Hence, the receiver spread length and lateral heterogeneity will play important role for the MASW method and there is definite scope for future work.

The use of a basic full-waveform inversion (FWI) scheme for the near-surface is proposed in this chapter to address some of those problems. In the FWI, entire waveforms of individual traces are compared between observed and estimated data. Since one would attempt in FWI to estimate the physical properties of the subsurface layers through matching the actual traces, the lateral heterogeneity problem should be solved to some degree. In next few sections, the methodology of the basic FWI used in this study has been discussed along with some synthetic dataset examples related to vertically and laterally heterogeneous media.

5.2 Basic concepts of full-waveform inversion

The basic pattern of many geophysical inversions is to find a match between observed and estimated (or modeled) data. In most of the cases, a parameter is first derived from the original dataset e.g. slowness or velocity, travel-time, amplitude, dispersion curve (for MASW) etc. Then, the measured wavefield through the medium is estimated based on the forward modeling. The parameters are changed until the

synthetic data matches the actual data. Any limitation in deriving those data propagates throughout the entire inversion scheme. In other words, the inverted results will be as good as the quality of the derived parameters. For example, the travel-time estimation is dependent on the quality of the first-break picks from the raw seismic dataset. In many cases, the first-break picking procedure is entirely dependent on the efficiency and experience of the processers and ought to be contaminated with some human error. So, when the travel-times (estimated from these first-break picks) are inverted to generate the background velocity structure, one should not expect the perfect match.

Similarly, MASW has some limitations for generating dispersion curves, e.g. receiver spread length and averaging of velocity, heterogeneity, mixing of modes etc. The manual picking of the highest amplitudes (related to the specific phase velocity and frequency pair) from the semblance-like dispersion curves may cause some errors as well. These picked dispersion curves are used for the inversion to estimate S-wave velocities. So, some errors are anticipated which may propagate in the final S-wave velocity results. In previous chapters, it has been shown that the MASW method works well to estimate the near-surface S-wave velocities. But, the above mentioned limitations would affect the results, especially the presence of any strong lateral heterogeneity. So, there is a scope to improve these smoothed S-wave velocity models for better resolution. Since FWI is a data-fitting procedure, it is commonly considered as a more accurate inversion process. A basic FWI scheme through

modeling surface-waves (ground-roll) is discussed in this chapter as a potential tool to mitigate above mentioned problems. We use the S-wave velocities from the MASW method as the starting model for FWI.

The most important requirements for the FWI procedure are: i) a good starting earth model, ii) an efficient forward modeling tool, and iii) the presence of lower frequencies in the observed dataset (Virieux and Operto, 2009). FWI is a computationally expensive method. The most common scheme for FWI is the gradient-based local differential approach which is time-consuming but more accurate. But, commendable improvement in computing power during last few years can handle this problem and hence FWI is gaining popularity. For FWI (and many geophysical inversions), a common problem is the convergence of the misfit function (difference between observed and calculated data) or error to the local minima instead of global minima (Menke, 2012). This is dependent on the quality of the starting model, the propagation assumed, the complexity of the parameters, and the presence of the lower frequencies. If a good starting model closer to the actual model (i.e. global minima) is available, then there is a less chance of converging to the local minima. Figure 5.1 shows that the improved (or updated) solution is very close to the global minimum when the trial solution is also closer; but Figure 5.2 shows that the error hits the local minimum when the trial solution is far from global minimum (Menke, 2012). We use the estimated S-wave velocities from MASW as the starting model (or solution) for the proposed inversion scheme. The S-wave velocity results

from MASW may not be perfect but can be very close to the actual S-wave velocities (as shown in earlier chapters). The presence of the lower frequencies in the data is essential to handle the 'cycle-skipping' problem (Figure 5.3). Cycle-skipping may arise if a particular cycle of the modeled data is not in-phase with the same cycle of the observed data. The proper care (low-frequency input, use of optimum offset etc.) should be taken to handle this problem for faster convergence.

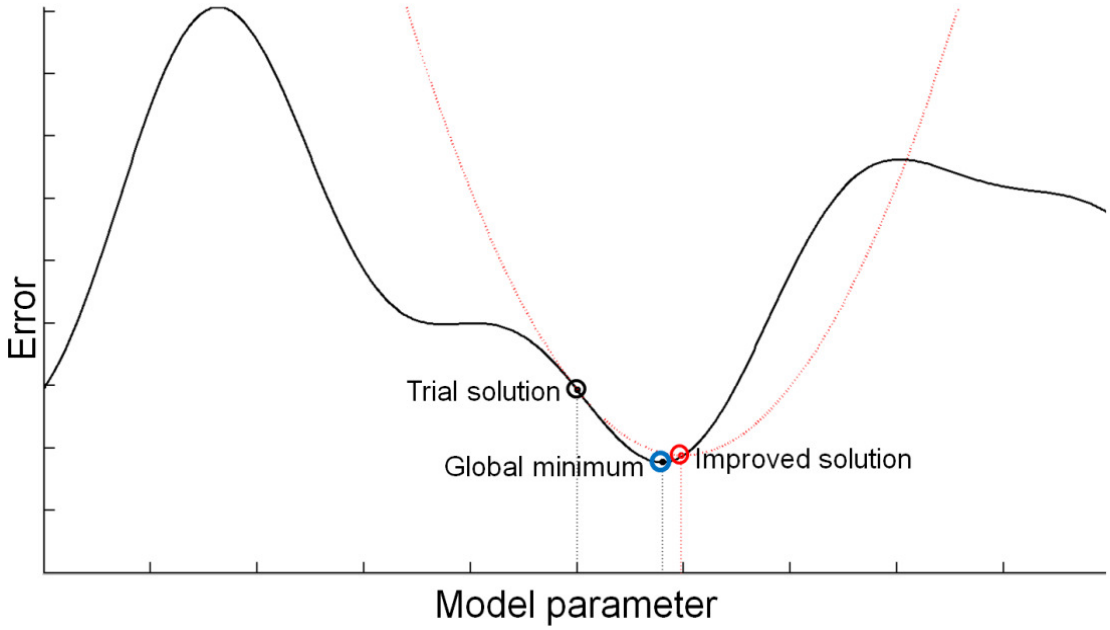

Figure 5.1. The figure shows that if the trial solution or initial estimate (black circle) is close to the global minima (blue circle) then the improved solution or updated estimate (red circle) converges to the global minima (modified after Menke, 2012).

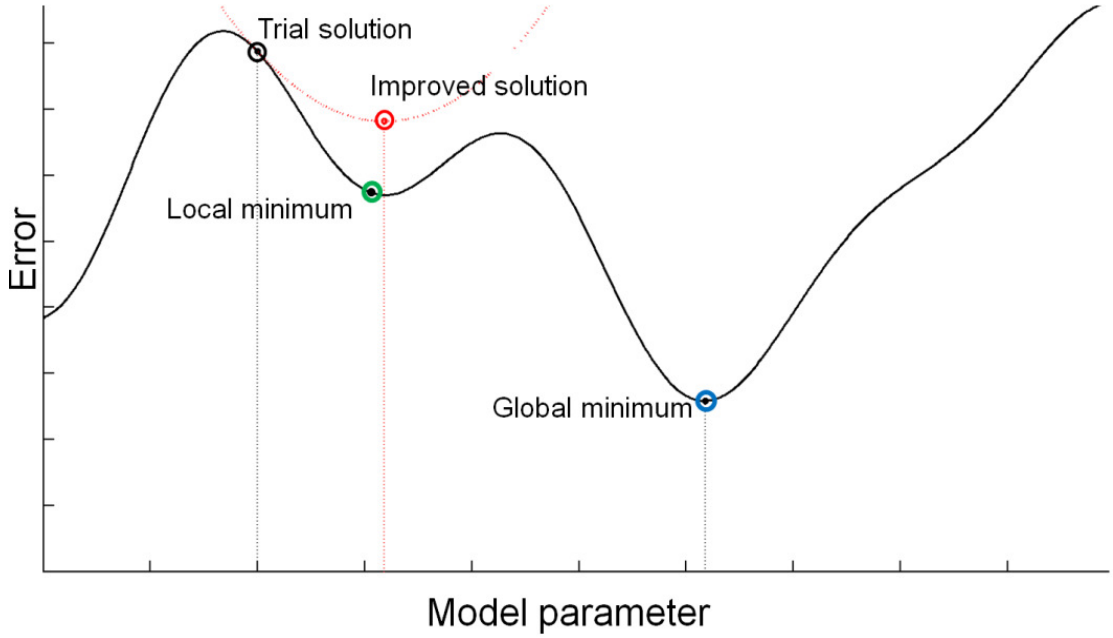

Figure 5.2. The figure shows that if trial solution or initial estimate (black circle) is too far from global minima (blue circle) then improved solution or updated estimate (red circle) converges to local minima in green circle (modified after Menke, 2012).

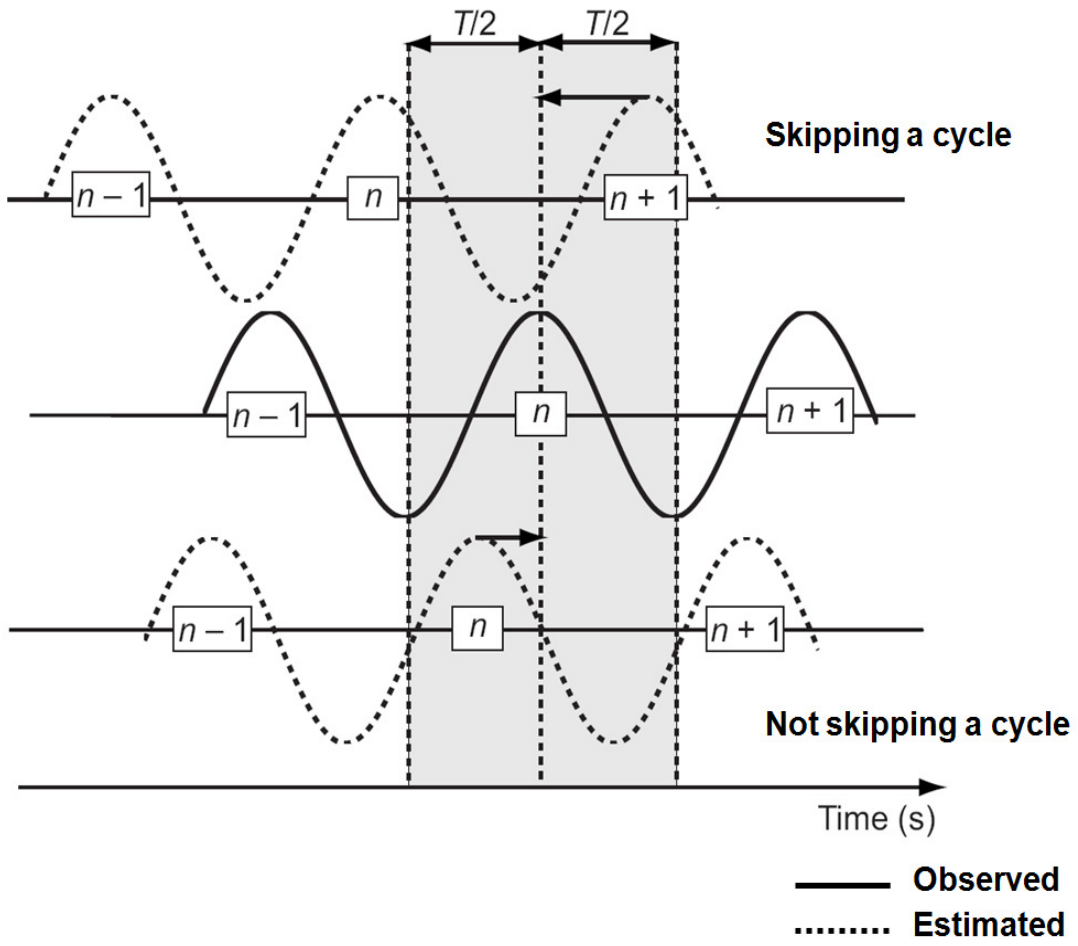

Figure 5.3. A schematic diagram shows the cycle-skipping concept in FWI. The observed seismogram (in solid black) is of period *T*. The upper dashed line represents the estimated seismogram with a time delay > *T*/2. At this situation, the *n*+1th cycle of estimated data will match the *n*th cycle of observed data (cycle-skipping phenomena). For the bottom case, estimated data is in-phase with the observed showing no cycle-skipping (modified after Virieux and Operto, 2009).

5.3 FWI methodology

We use a straightforward FWI scheme just to evaluate how an input starting model from MASW can be updated to get more accurate results for laterally homogeneous

as well as heterogeneous media. The strategy for this FWI method is to – i) estimate a good quality starting model (S-wave velocities and layer thickness from MASW), ii) generate modeled data through forward-modeling, and iii) invert in a linear least-square manner to obtain the model parameter update. Figure 5.4 visually summarizes these steps. We have attempted a totally discrete approach instead of analytical approach. The method for this study is similar to that of a discrete Gauss-Newton method (Pratt et al., 1998; Menke, 2012; Sen, 2012). For the forward-modeling, we have used the ANIVEC software (Mallick and Frazer, 1987) for laterally homogeneous media and a finite-difference based code written in MATLAB environment (Manning, 2007) for laterally heterogeneous media. Once the modeled data is estimated through forward modeling, we have used the MATLAB environment to compare observed and modeled data and to calculate the model update. The details of this FWI procedure are discussed in the following sections. We seek to develop a near-surface, elastic, multi-component, multi-parameter FWI method. Each layer of the subsurface can be simply characterized by the following parameters –

1. P-wave velocity: V_P
2. S-wave velocity: V_S
3. Density: ρ
4. Thickness: T
5. Attenuation: Q

We can estimate the near-surface P-wave velocity structure (from first-break pick and travel-time tomography), S-wave velocity structure (from S-wave refraction, MASW or any other surface-wave inversion method), density (from well log or predicted from V_P and/or V_S), and thickness (from velocity structures) as the starting model for FWI. Estimation of the attenuation is always a challenge. It is to some extent a common practice to pre-condition the data by correcting for attenuation before running FWI. Though it is challenging, but the modeling of attenuation can be performed in FWI as well. So, one can update five parameters for each layer. The goal of this study is to evaluate whether S-wave velocity from MASW analysis can be used as a good starting model for a near-surface FWI. So, in this FWI scheme, only S-wave velocity (and thickness) has been updated.

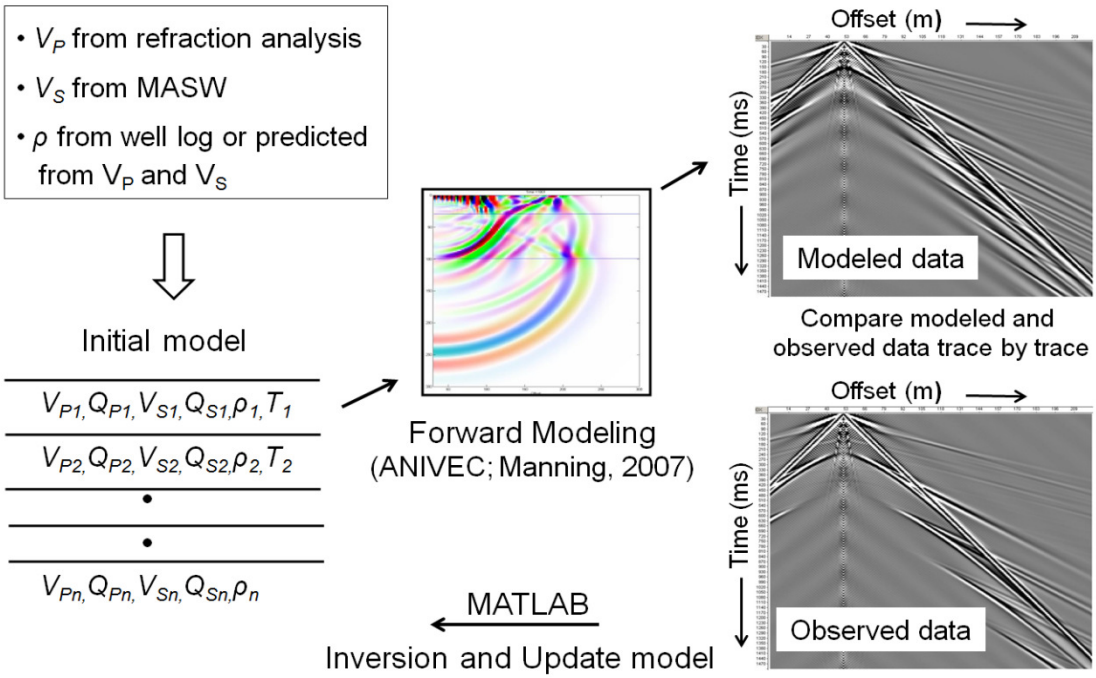

Figure 5.4. A schematic diagram shows the overall scheme of the basic FWI used in this study.

The observed seismic data (synthetic or real data) can be expressed as $d_{m\times n}^{obs}$ (for one component), where the number of samples is *m* and number of traces is *n*. Then, a starting model can be established by analyzing the observed data (e.g. S-wave velocity from MASW for this study). A forward modeling tool is applied on the starting model to generate the initial estimated data $d_{m\times n}^{est0}$. The difference between the observed and the estimated data is termed as the data misfit (Δd) and can be written as $\Delta d = d^{obs} - d^{est}$. Now, in FWI, observed and estimated data are compared in data domain itself i.e. trace by trace and sample by sample. So, the observed and the estimated data can also be written as long column vectors - $d_{mn\times 1}^{obs}$ and $d_{mn\times 1}^{est0}$ and the data misfit can be written as:

$$\Delta d_{mn\times 1}^{0} = d_{mn\times 1}^{obs} - d_{mn\times 1}^{est0} \tag{5.1}$$

The difference between observed and estimated data (Equation 5.1) can be linearly related to the changes required in the parameter which we plan to update (Stewart, 1983). So, the linearized equation can be written as:

$$\Delta d_{mn\times 1}^{0} = \frac{\partial d_{mn\times 1}^{est0}}{\partial p_j^0} \Delta p_j^0 \tag{5.2}$$

where, p_j^0 are the starting parameters needed to be updated. The partial derivative portion in Equation 5.2 can be calculated analytically or by forward difference. For this study, we have opted for the simple but accurate forward difference approach to calculate the partial derivatives. Now, Equation 5.2 can be written in the matrix form such as:

$$\begin{bmatrix} \Delta d_1^0 \\ \Delta d_2^0 \\ \vdots \\ \vdots \\ \vdots \\ \Delta d_m^0 \\ \vdots \\ \vdots \\ \vdots \\ \Delta d_{mn}^0 \end{bmatrix} = \begin{bmatrix} \frac{d_1^{est0}(p_1^0+h_1)-d_1^{est0}(p_1^0-h_1)}{2h_1} & \cdots\cdots & \frac{d_1^{est0}(p_j^0+h_j)-d_1^{est0}(p_j^0-h_j)}{2h_j} \\ \frac{d_2^{est0}(p_1^0+h_1)-d_2^{est0}(p_1^0-h_1)}{2h_1} & \cdots\cdots & \frac{d_2^{est0}(p_j^0+h_j)-d_2^{est0}(p_j^0-h_j)}{2h_j} \\ \vdots & & \vdots \\ \vdots & & \vdots \\ \vdots & & \vdots \\ \frac{d_m^{est0}(p_1^0+h_1)-d_m^{est0}(p_1^0-h_1)}{2h_1} & \cdots\cdots & \frac{d_m^{est0}(p_j^0+h_j)-d_m^{est0}(p_j^0-h_j)}{2h_j} \\ \vdots & & \vdots \\ \vdots & & \vdots \\ \vdots & & \vdots \\ \frac{d_{mn}^{est0}(p_1^0+h_1)-d_{mn}^{est0}(p_1^0-h_1)}{2h_1} & \cdots\cdots & \frac{d_{mn}^{est0}(p_j^0+h_j)-d_{mn}^{est0}(p_j^0-h_j)}{2h_j} \end{bmatrix} \begin{bmatrix} \Delta p_1^0 \\ \vdots \\ \Delta p_j^0 \end{bmatrix} \quad (5.3)$$

where h is the small perturbation used to calculate the partial derivatives. Equation 5.3 can be written in a shorter form:

$$Y = AX \quad (5.4)$$

where Y is the data misfit column vector of $mn \times 1$ size, A is the partial derivative matrix (commonly known as Jacobian matrix or Frechet derivative matrix) of $mn \times j$ size, and X is the column vector of parameter updates of $j \times 1$ size. The goal is to calculate X by matrix inversion. We have calculated X using the simple least-square inversion in the MATLAB programming environment which can be written as:

$$X = (A^T A)^{-1} A^T Y \quad (5.5)$$

where, superscript T refers to the regular matrix transpose. Once, X is calculated then the starting earth model is updated and the entire procedure is repeated in an iterative manner until the desired data matching has been achieved. So, the input parameters for the next model will be:

$$p_j^1 = p_j^0 + \Delta p_j^0 \tag{5.6}$$

Then, the estimated dataset is again calculated through forward modeling using these updated parameters. So, the new estimated dataset can be written as $d_{m\times n}^{est1}(p_{1,}^1 p_{2,}^1 \dots , p_j^1)$. For this study, we are dealing with five parameters – P-wave velocity, S-wave velocity, density, thickness, and attenuation for each layer. From the procedure described above, it is evident that for each step or iteration, we have to perform $2j+1$ forward modeling steps – one forward modeling step to generate the estimated dataset and $2j$ forward modeling steps to calculate the partial derivatives (two forward models for each parameter).

5.4 Results

We evaluate whether the S-wave velocity structure from MASW can be used as a good starting model for the above discussed FWI scheme. For the simplicity and testing the FWI scheme, we assume P-wave velocity, density, and attenuation to be known. So, S-wave velocity (and layer thickness) will only be updated. Two synthetic models have been used: i) Model 1: a laterally homogeneous layer over half-space, and ii) Model 2: a vertical single layer merged with another vertical layer of different material properties i.e. laterally heterogeneous. The synthetic seismic dataset from Model 1 has been generated using ANIVEC which is a fast and stable forward modeling code that generates elastic, multicomponent seismic dataset. But, it is a reflectivity based code and only works for the layered earth model where each layer is

horizontal and laterally homogeneous. It works well for Model 1 but not for Model 2 since that is a laterally heterogeneous case. So, the synthetic seismic dataset from Model 2 has been generated using finite-difference forward modeling code written in MATLAB (Manning, 2007) and capable of handling lateral changes.

5.4.1 Laterally homogeneous case

This section shows the application of the FWI method to a laterally homogenous case (Model 1). The properties of the Model 1 have been described in Figure 5.5. The synthetic seismic dataset from Model 1 has been generated using ANIVEC (Figure 5.6). Then, the traditional MASW method has been applied on the synthetic data to estimate the S-wave velocity and thickness. For simplicity, we just use S-wave velocity and thickness (estimated from MASW) of the first layer and assume all other parameters to be known. So, we invert for two parameters (j=2 in Equation 5.3) – the first layer S-wave velocity and the first layer thickness. From MASW, we estimated the first layer S-wave velocity as 257 m/s (actual value is 250 m/s) and the first layer thickness as 20 m (actual value is 30 m). A starting model has been assumed with these new values of first layer S-wave velocity and thickness and keeping all other parameters same as the actual model. Then forward modeling (using ANIVEC) on this starting model generates the initial estimated data i.e. $d_{m\times n}^{est0}$ (Figure 5.7). Then we followed the Equation 5.3 to calculate the partial derivative matrix and the Equation 5.5 to estimate the parameter updates (i.e. Δp_j^0). After careful analysis, we identified that low-frequency (common for FWI to avoid cycle-skipping) and

relatively near-offset input was required for better convergence to the global minima for first few iterations. The frequency content and offset range were increased in later iterations. Figure 5.8 shows that how some individual estimated traces (or waveforms) are converging or matching with the synthetic (or observed) traces after every iteration. Figure 5.9 shows how the data residuals change with iterations and finally residuals become almost zero i.e. observed and estimated datasets have been matched completely. The final estimated parameter values are: first layer S-wave velocity = 250.04 m/s (actual value = 250 m/s), and first layer thickness = 29.6 m (actual value = 30 m).

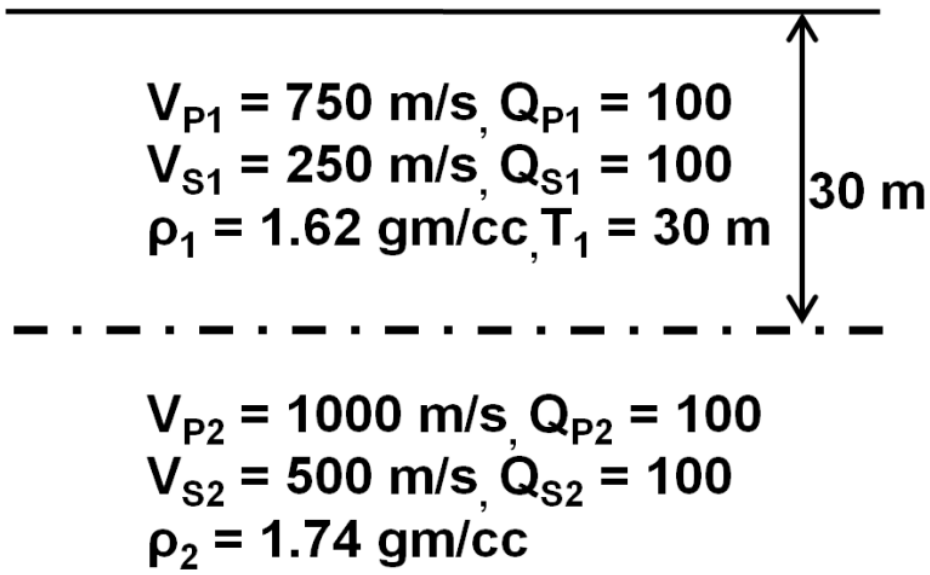

Figure 5.5. The schematic diagram shows the laterally homogeneous Model 1 used in this study.

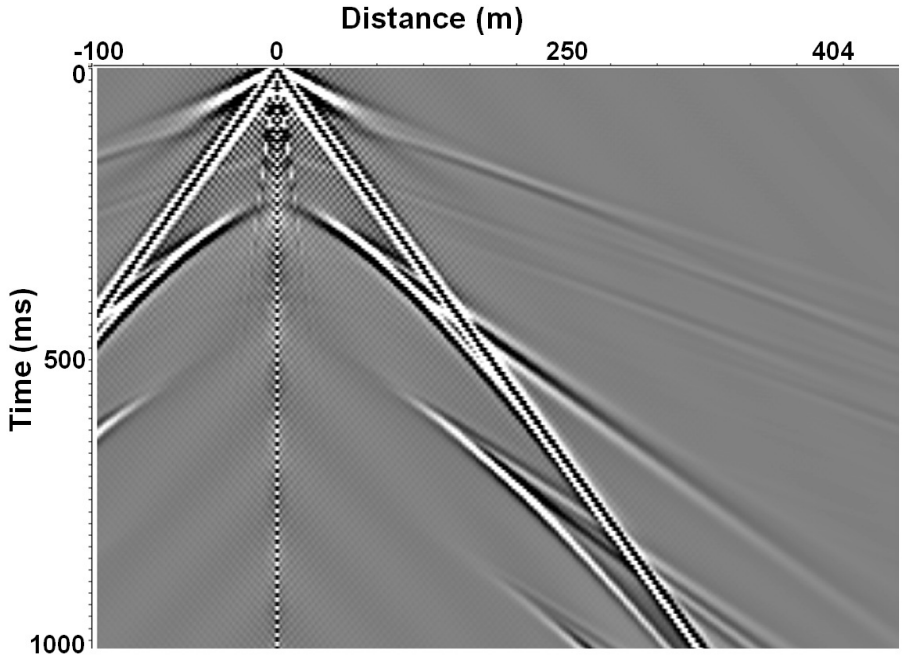

Figure 5.6. The synthetic dataset (observed data) from Model 1 generated using ANIVEC.

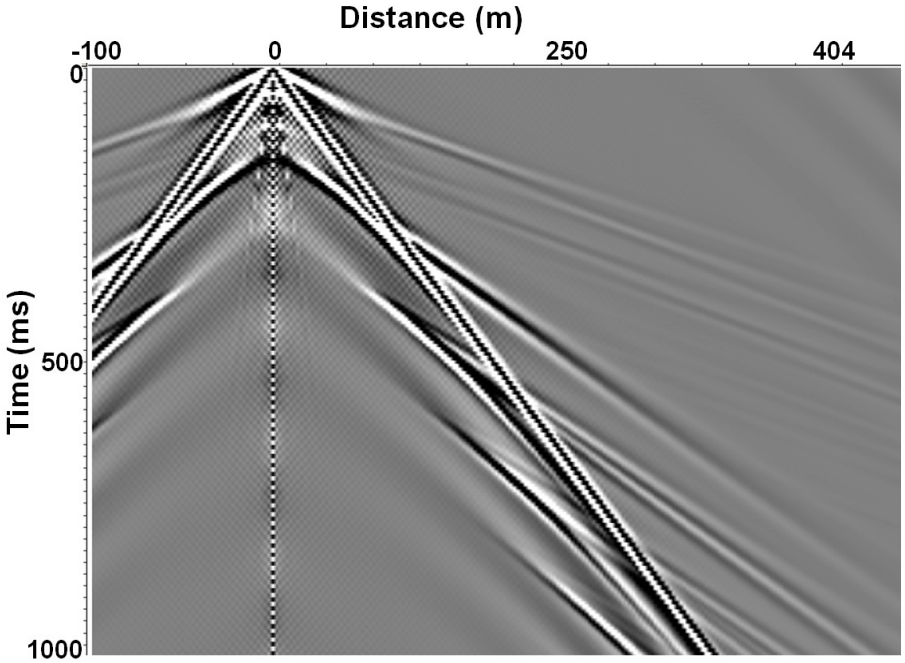

Figure 5.7. The initial estimated dataset with the starting S-wave velocity model of the first layer obtained from MASW (generated using ANIVEC).

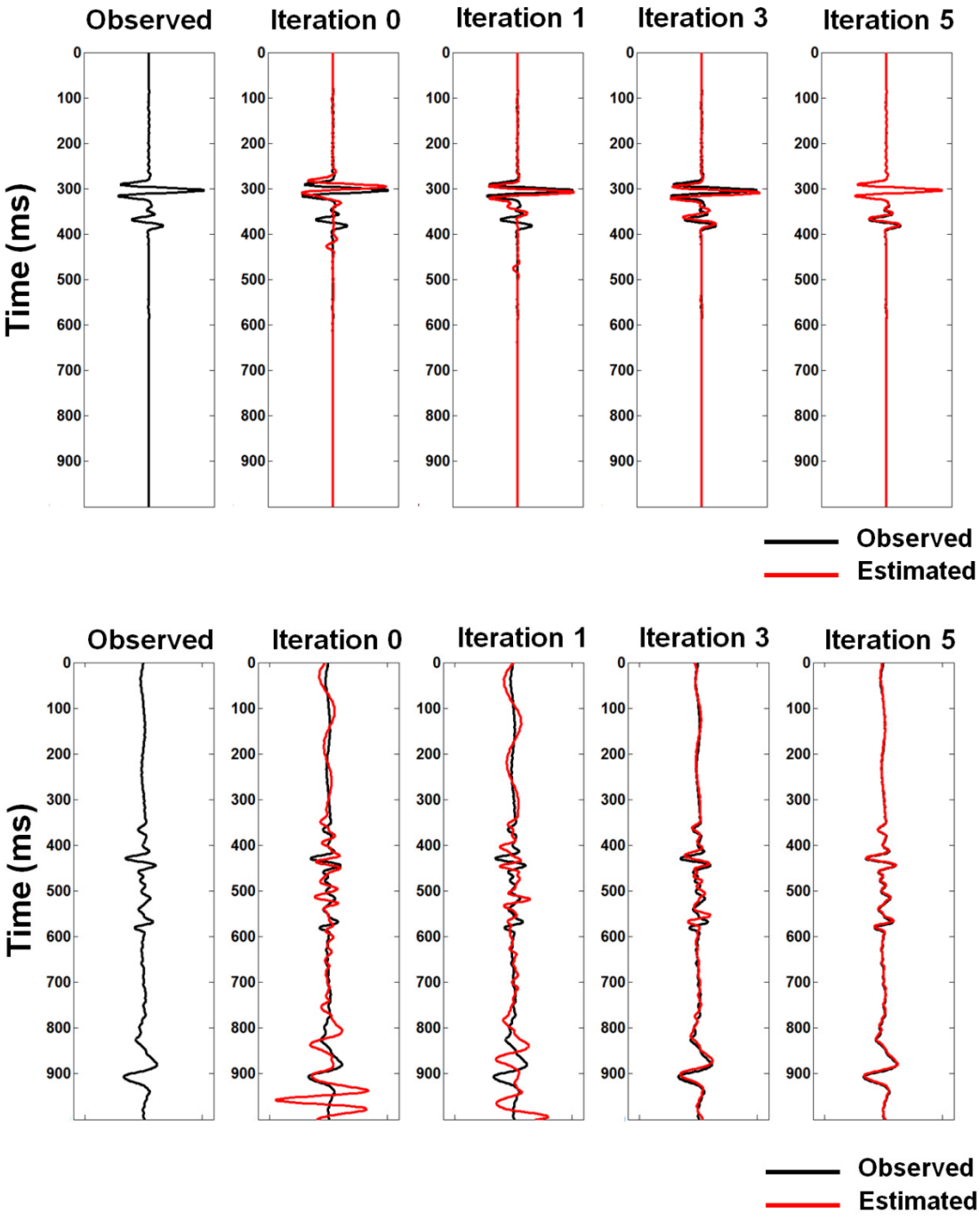

Figure 5.8. The figure shows the convergence of the estimated traces for near-offset (upper) and far-offset (lower) cases for few iterations for Model 1. A good match has been achieved after five iterations.

a)

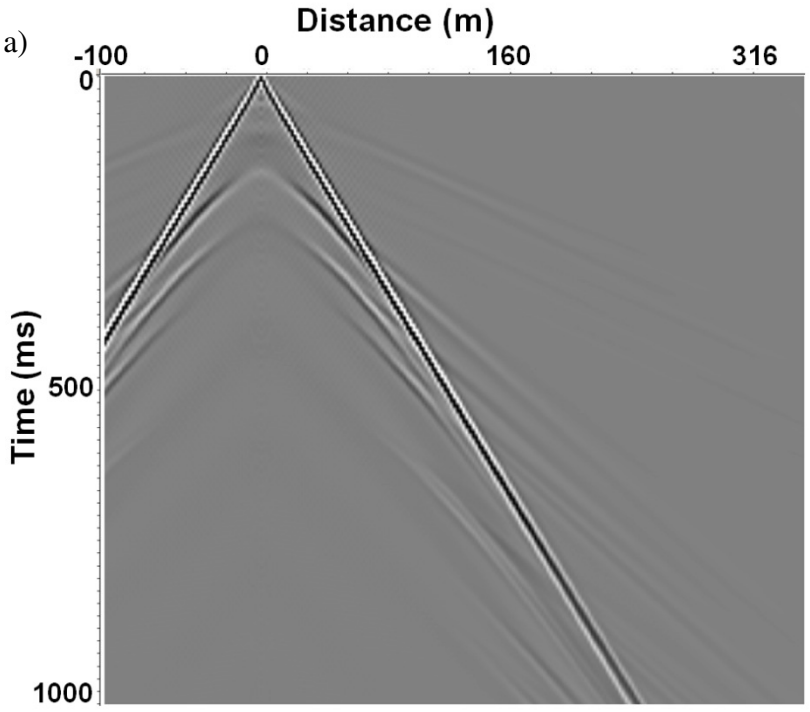
Distance (m)
-100
0
160
316
0
500
1000
Time (ms)

b)

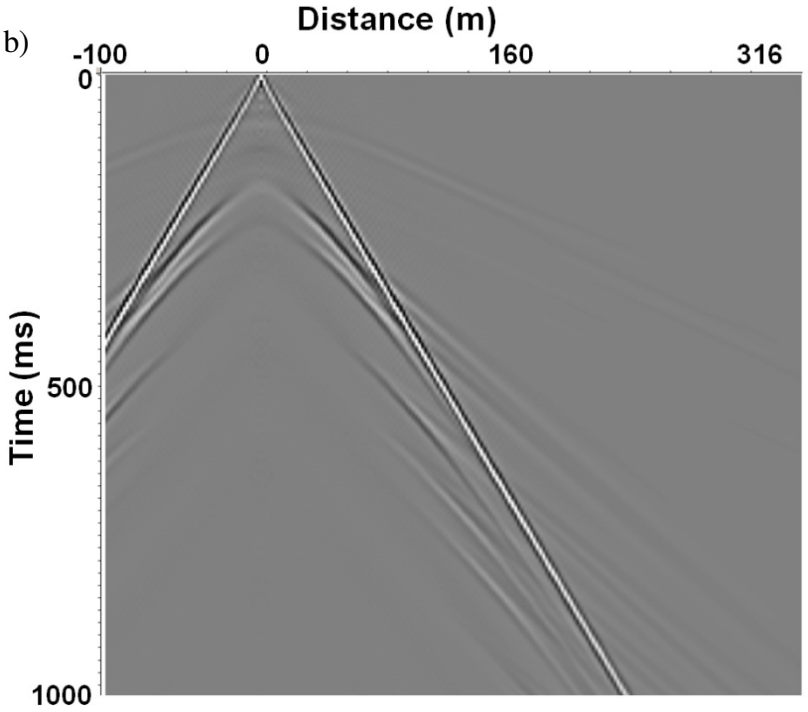
Distance (m)
-100
0
160
316
0
500
1000
Time (ms)

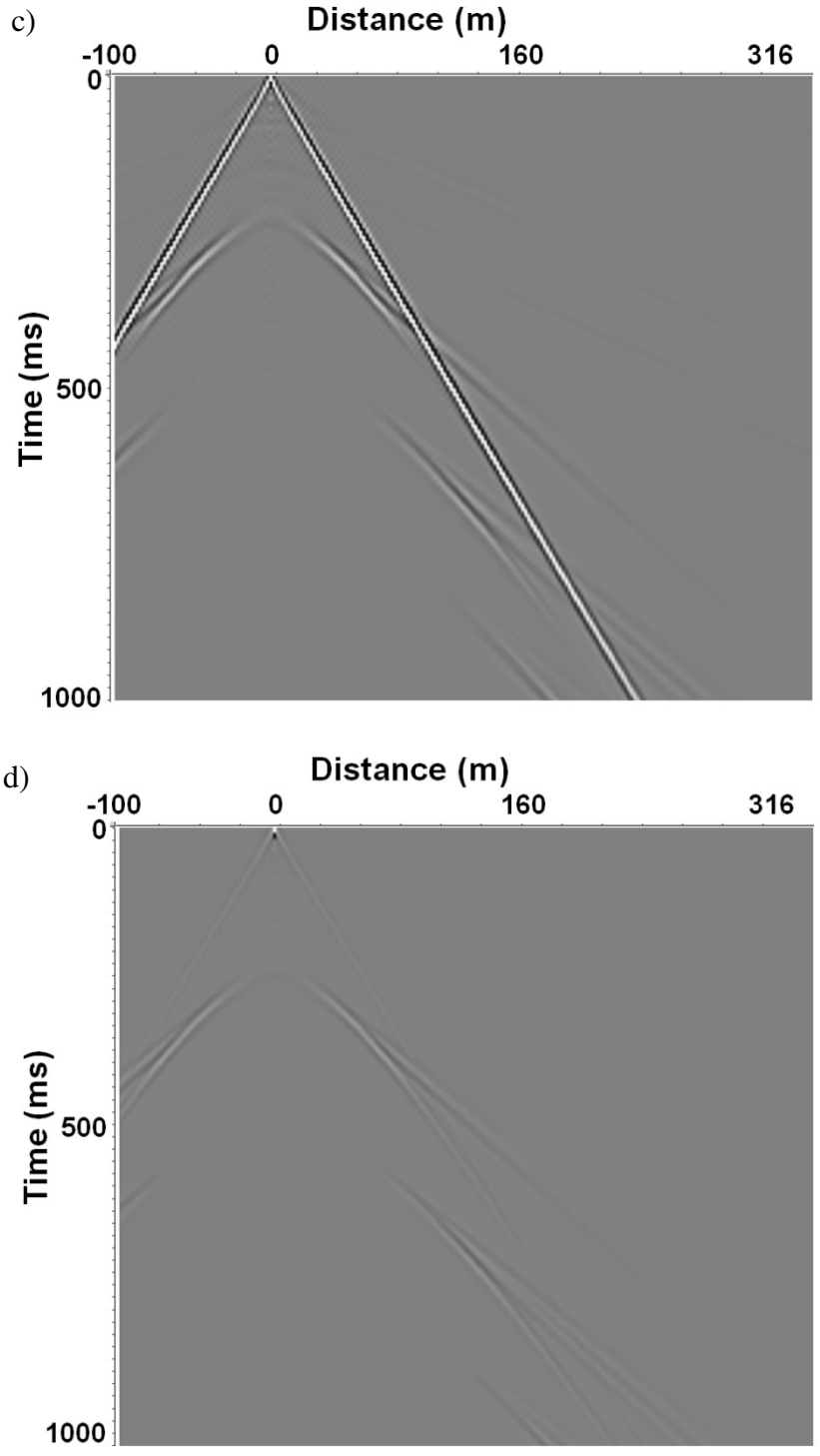

Figure 5.9. The figure shows the data residuals for Model 1 – a) initial, b) after iteration 1, c) after iteration 3, and d) after iteration 5 or final residual.

5.4.2 Laterally heterogeneous case

The bigger challenge is to evaluate the FWI scheme for laterally heterogeneous media. We used a very simple laterally heterogeneous model (Model 2) shown in Figure 5.10. The parameters of Model 2 are similar to the physical model experiment discussed in Chapter 4. The left part of Model 2 is similar to Plexiglas material and the right part of Model 2 is similar to Aluminum material. Figure 5.11 shows the synthetic seismic data for Model 2 generated using MATLAB code (Manning, 2007). Then, S-wave velocities for Model 2 have been calculated using MASW method and used as starting model. The calculated S-wave velocity from MASW for layer 1 is 1280 m/s (actual value is 1380 m/s) and that for layer 2 is 2900 m/s (actual value is 3100 m/s). Then the initial dataset (Figure 5.12) is estimated using the S-wave velocities from MASW as the starting parameters. Next, the FWI scheme is applied as discussed before. In this case, we have updated two parameters – S-wave velocity of layer 1 (Plexiglas) and of layer 2 (Aluminum). But, for first few iterations, only layer 1 S-wave velocity is updated with low-frequency and nearer offsets. Then, two parameters are updated simultaneously and higher frequencies and far offsets have also been incorporated. Figure 5.13 shows different individual observed and estimated traces showing convergence with iterations. Figure 5.14 shows how the data residuals change with iterations and finally residuals become almost zero i.e. observed and estimated datasets have been matched completely. In this way, we have tried this brute-force FWI for both laterally homogenous and heterogeneous media which shows a good convergence.

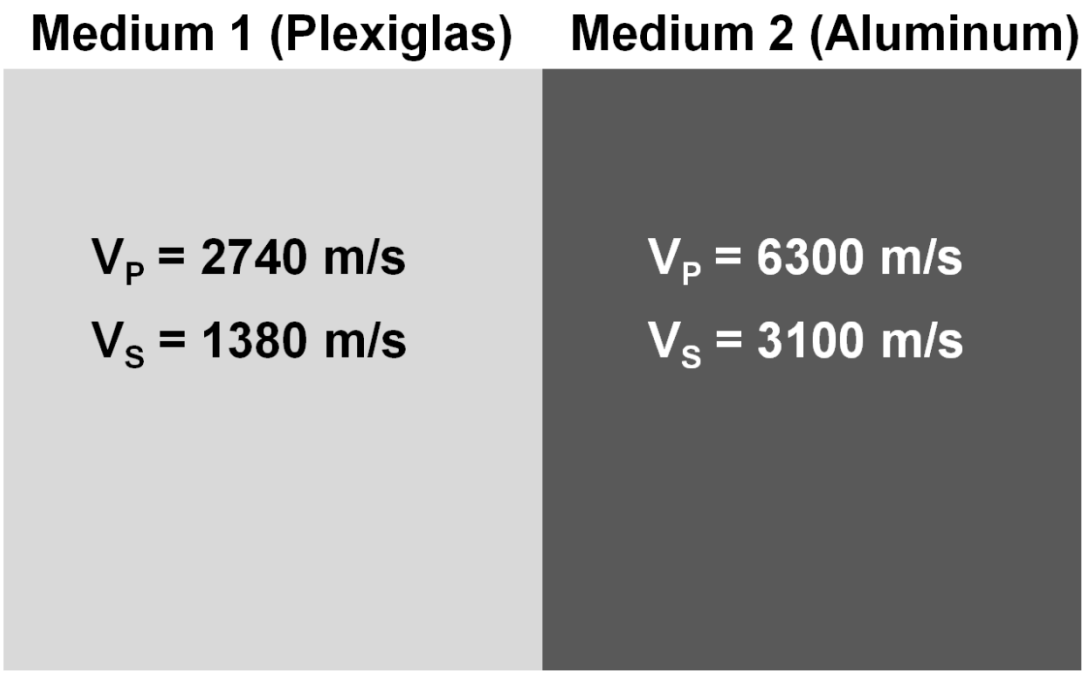

Figure 5.10. The schematic diagram shows the laterally heterogeneous Model 2 used in this study.

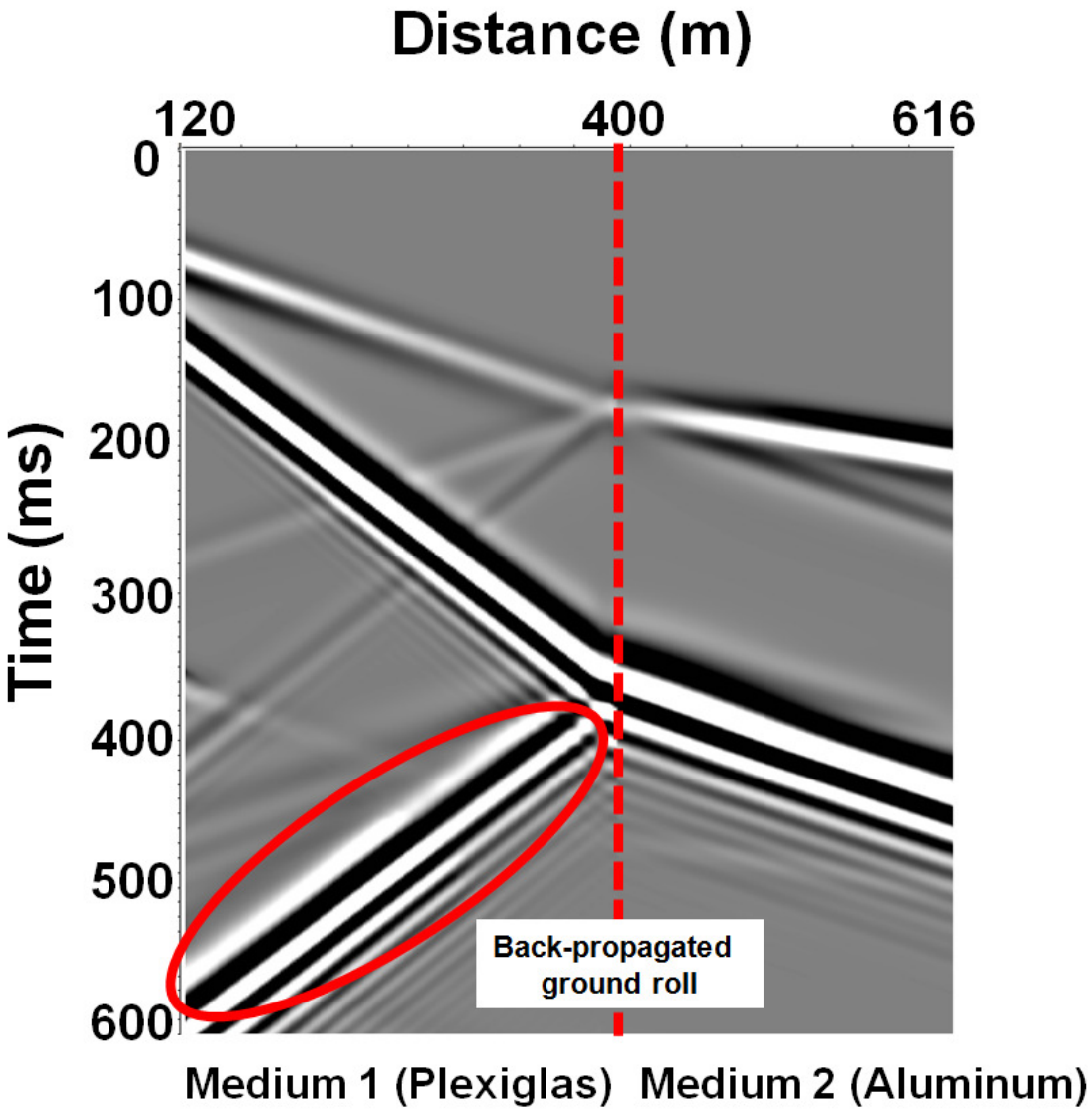

Figure 5.11. The synthetic dataset (observed data) from Model 2 generated using MATLAB code (Manning, 2007).

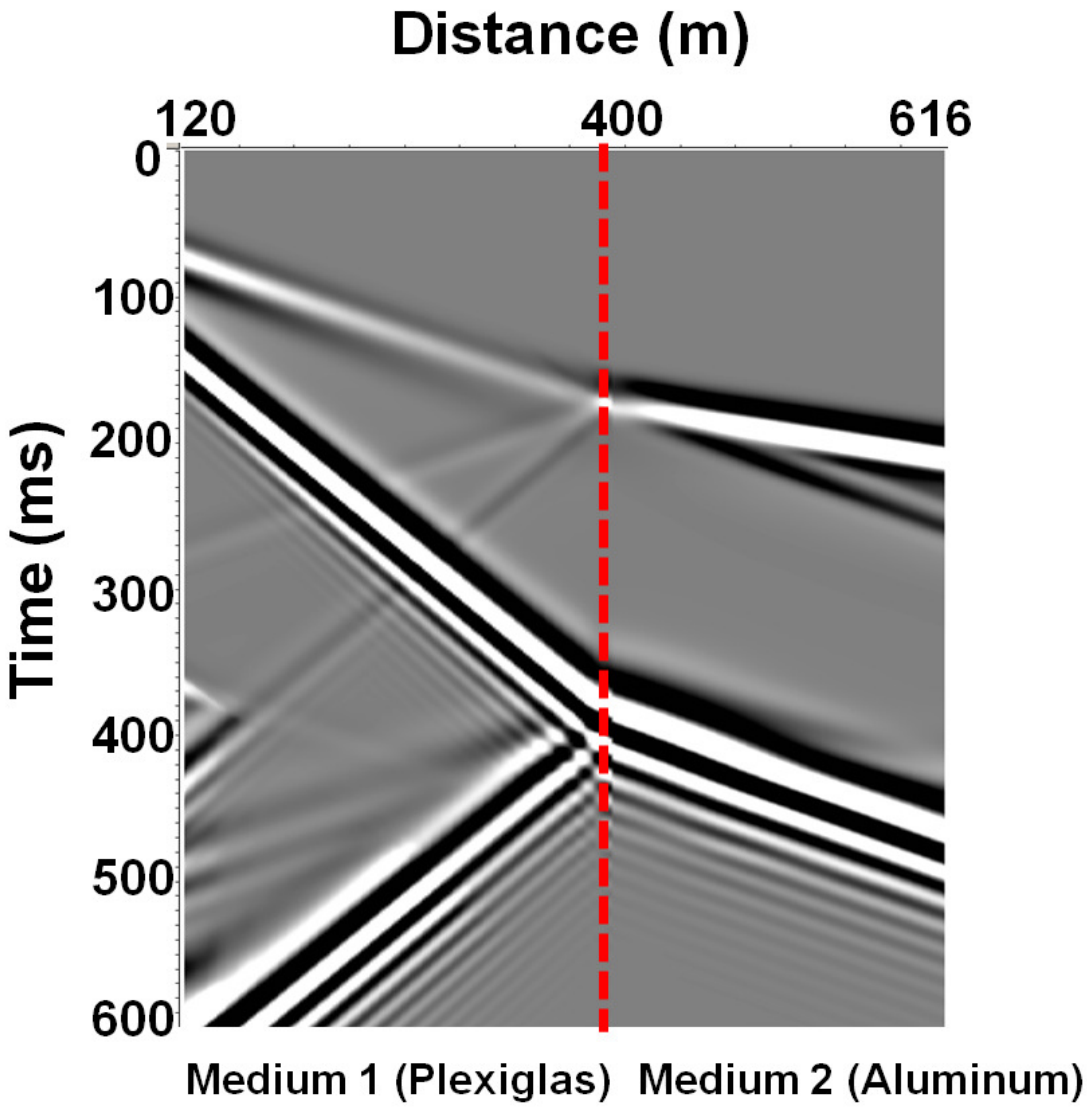

Figure 5.12. The initial estimated dataset with the starting S-wave velocity model obtained from MASW (generated using MATLAB code by Manning, 2007).

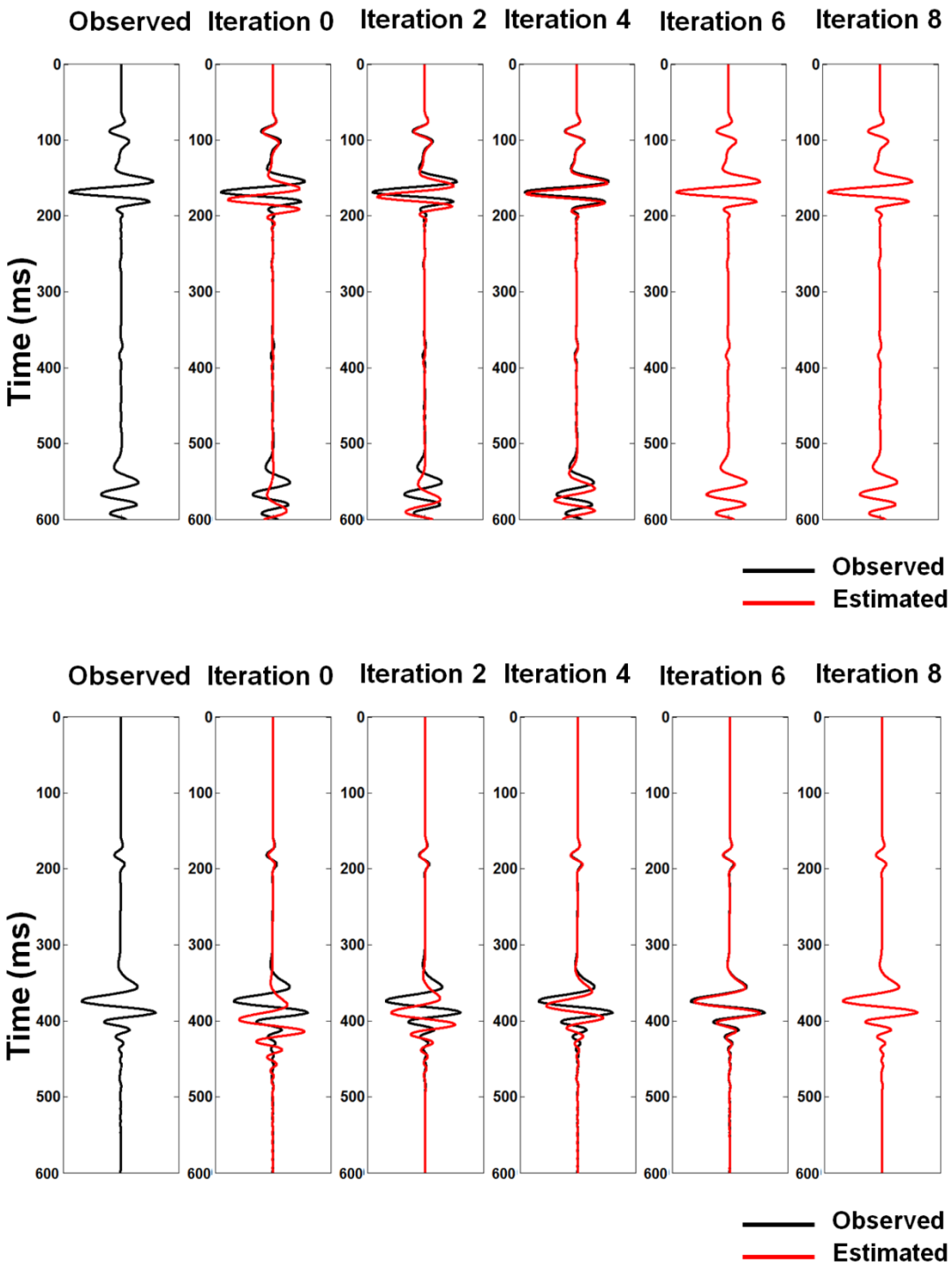

Figure 5.13. The figure shows the convergence of the estimated traces for near offset (upper) and far offset (lower) cases for few iterations for Model 2. A good match has been achieved after eight iterations.

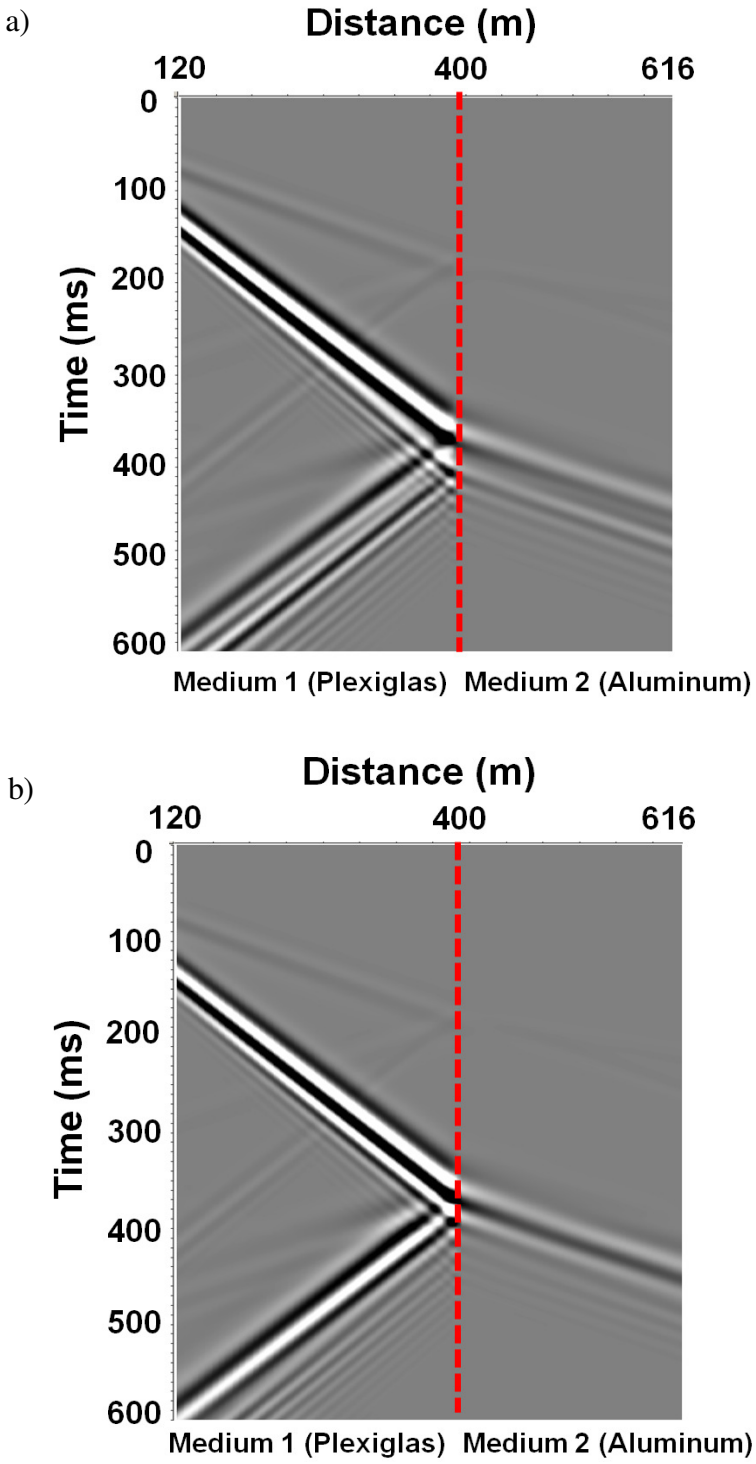

Figure 5.14. The figure shows the data residuals for Model 2 – a) initial, b) after iteration 2.

c)

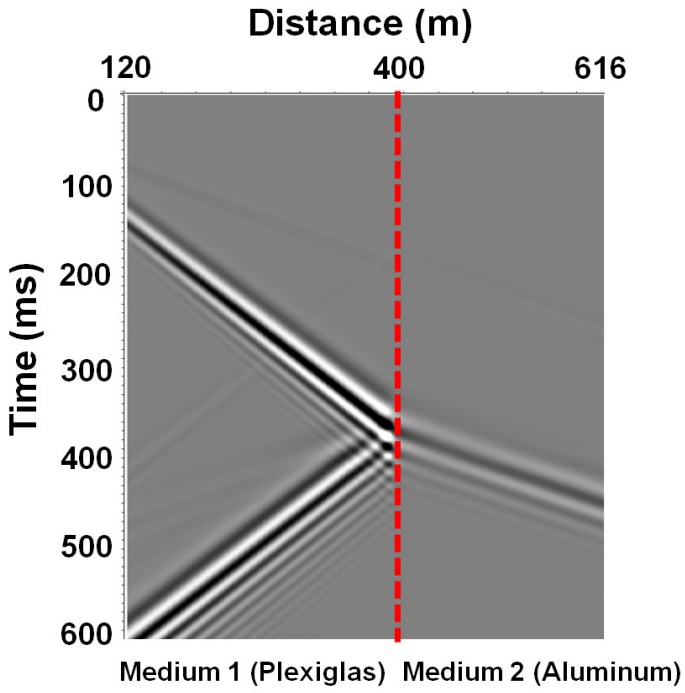

d)

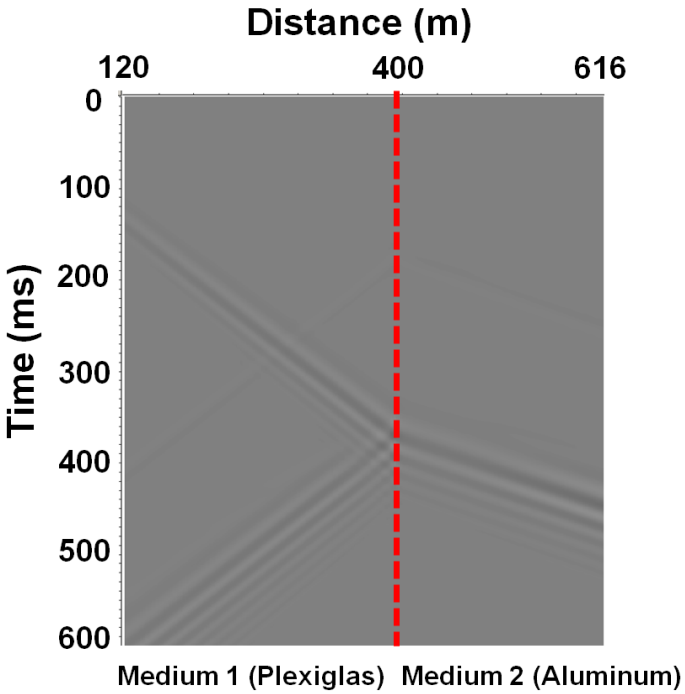

Figure 5.14 (cont.). The figure shows the data residuals for Model 2 – c) after iteration 4, d) after iteration 6.

e)

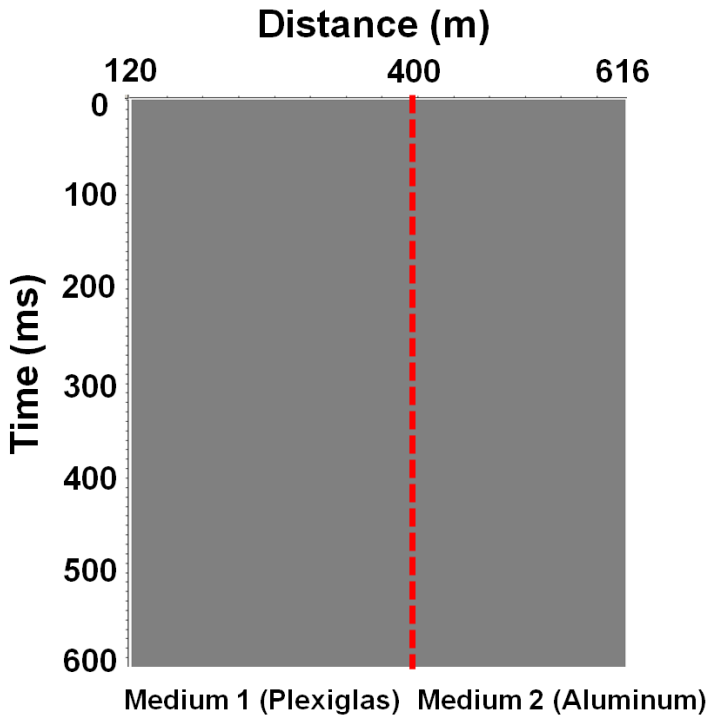

Figure 5.14 (cont.). The figure shows the data residuals for Model 2 – e) after iteration 8 or final residual.

5.5 Conclusions

We have evaluated the feasibility of using S-wave velocities from MASW as the starting model for a simple FWI method. The brute-force forward difference based FWI worked reasonably well with the synthetic datasets. The formulation of the scheme has the potential to use this FWI as a multi-parameter, multi-component, elastic process. Though the main aim is to use it for the near-surface – to model ground-roll, first-break picks etc.; still theoretically it should handle some later events as well. We have tested the method with synthetic datasets for laterally homogeneous

as well as laterally heterogeneous media. For Model 1, initial S-wave velocity was 257 m/s (actual: 250 m/s) and thickness was 20 m (actual: 30 m) for the first layer. For Model 2, initial S-wave velocity for medium 1 was 1280 m/s (actual: 1380 m/s) and for medium 2 it was 2900 m/s (actual: 3100 m/s). So, the starting S-wave velocities from MASW are close to the actual values but still have errors of 2.8 % (for Model 1) to 7.25 % (for Model 2). We have achieved a good match after 6-10 iterations for each model. The FWI method has worked well for the laterally heterogeneous case (Model 2 case) as well which was the main goal of this study. We have started with these values and achieve a good match. We have followed a multi-stage strategy where data input was low-frequency and near-offset for earlier iterations with gradual incorporation of far offsets and higher frequency. Basically, we have not used any attenuation (e.g. Q=100) and the synthetic data is noise free. This makes it easier to use the FWI scheme. An immediate future scope is to use this scheme for a good quality real data to further test the robustness of the method.

Chapter 6

Shear-wave statics from surface-wave inversion (MASW)

6.1 Introduction

The near-surface often consists of unconsolidated, low-velocity layers (LVL) which can cause time delays or static shifts in passing seismic waves. The variations in the topography add further fluctuations in travel times leading to elevation statics. The combined effect of LVL and elevation statics can severely distort the acquired seismic data and affect refraction and reflection events. If not properly rectified in the early stages of seismic processing, statics problems can lead to incorrect final migrated sections. For many land seismic datasets, static-correction is often a challenge to seismic processors. Even for many marine seismic datasets, processors act cautiously for static-corrections (Bansal et al., 2009).

Both compressional (P) - and shear (S) -wave statics are important. But the fact that S-wave velocities are much lower compared to P-wave velocities in the near-surface makes S-wave static-correction even more important for multicomponent seismic analysis. With the increasing use of multicomponent seismic data, the S-wave static-correction problem is also looming large. Hence, it is necessary to obtain a detailed

near-surface S-wave velocity structure to obtain proper S-wave statics. For the S-wave statics calculation, the common practice among seismic processors is to: i) assume a fixed $\frac{V_P}{V_S}$ for the near-surface, and ii) use the PP image to deduce the S-wave statics. But, this approach is probably too simplistic because: i) the near-surface S-wave velocities are often very low and consequently $\frac{V_P}{V_S}$ is large, ii) the near-surface S-wave velocities may vary laterally so as $\frac{V_P}{V_S}$, and iii) S-wave velocities are less (or not) affected by the water table as compared to P-wave velocities (Cary and Eaton, 1993) and hence those should not be directly correlated (Figure 6.1).

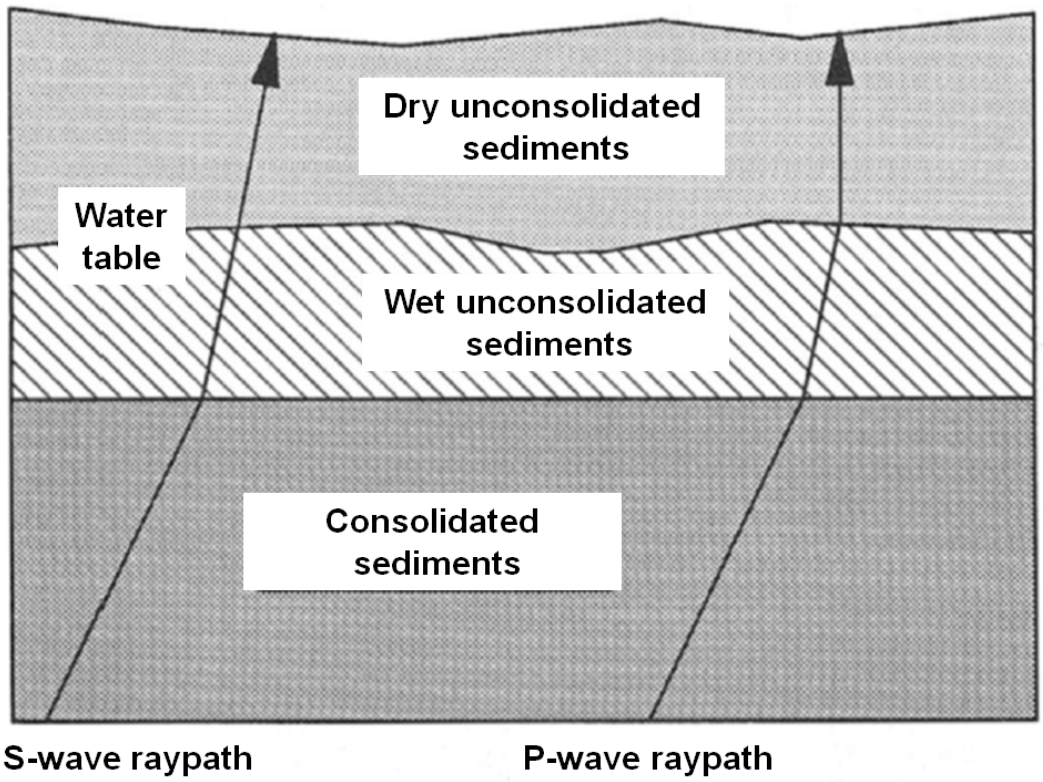

Figure 6.1. A schematic diagram showing P-wave velocities affected by the presence of the water table, but not S-wave velocities. Hence, P- and S-wave statics might not be correlated directly (Cary and Eaton, 1993).

6.2 Methodology for S-wave receiver statics calculation

In this study, the surface-wave inversion method (MASW) has been used to estimate the near-surface multi-layered S-wave velocity model varying with depth. Then this model will be used to calculate the time delays (LVL statics) in a surface consistent manner. For the purpose of this study, the main focus is on the calculation of S-wave LVL statics for only receiver (not shot) locations (Figure 6.2). The S-wave LVL statics can be calculated by summing the time delays in individual layers up to the base of LVL zone (Figure 6.3 and Equation 6.1). These statics are part of the S-wave receiver static originating in the low-velocity layers:

$$t_S^{LVL} = \sum_{i=1}^{n} \frac{\Delta Z_i^{LVL}}{\Delta V_{Si}^{LVL}} \tag{6.1}$$

where, t_S^{LVL} stands for S-wave LVL statics for *n*-layered near-surface S-wave velocity model for the LVL zone where ΔZ_i^{LVL} is the thickness and ΔV_{Si}^{LVL} is the S-wave velocity of the individual layers for the same model. Now, to obtain the total S-wave receiver statics, it is necessary to add the elevation statics as well. In this S-wave statics study, the two-step calculation has been performed:

i) To calculate the above mentioned S-wave LVL statics for each receiver (Equation 6.1) which virtually brings the receiver down to the base of LVL zone (Figure 6.4).

ii) To add the effect of topography i.e. including the weathering layer thickness along with elevation difference for each individual receiver location and bringing the

receiver back to a fixed flat floating datum (Figure 6.4 and Equation 6.2). Now, the fixed datum may be below the base of LVL zone or above the LVL zone. In this study, the case related to the datum above the LVL zone has only been shown:

$$t_S^{Elevation} = \frac{(Fixed\ datum\ elevation - Receiver\ elevation) + Z^{LVL}}{S - wave\ replacement\ velocity} \tag{6.2}$$

where, $Z^{LVL} = \Delta Z_1^{LVL} + \Delta Z_2^{LVL} + \ldots + \Delta Z_n^{LVL}$ i.e. the total thickness of the LVL zone and S-wave replacement velocity is a velocity which is close (or greater) than the S-wave velocity at the base of the LVL zone. This S-wave replacement velocity is assumed to bring the receiver back on the flat datum if no LVL zone and topography would have been present. Finally, Equation 6.1 is subtracted from Equation 6.2 to obtain the final S-wave receiver statics (Equation 6.3) for the case where datum is above the weathered layer (Cox, 1999):

$$t_S^{Final} = t_S^{Elevation} - t_S^{LVL} \tag{6.3}$$

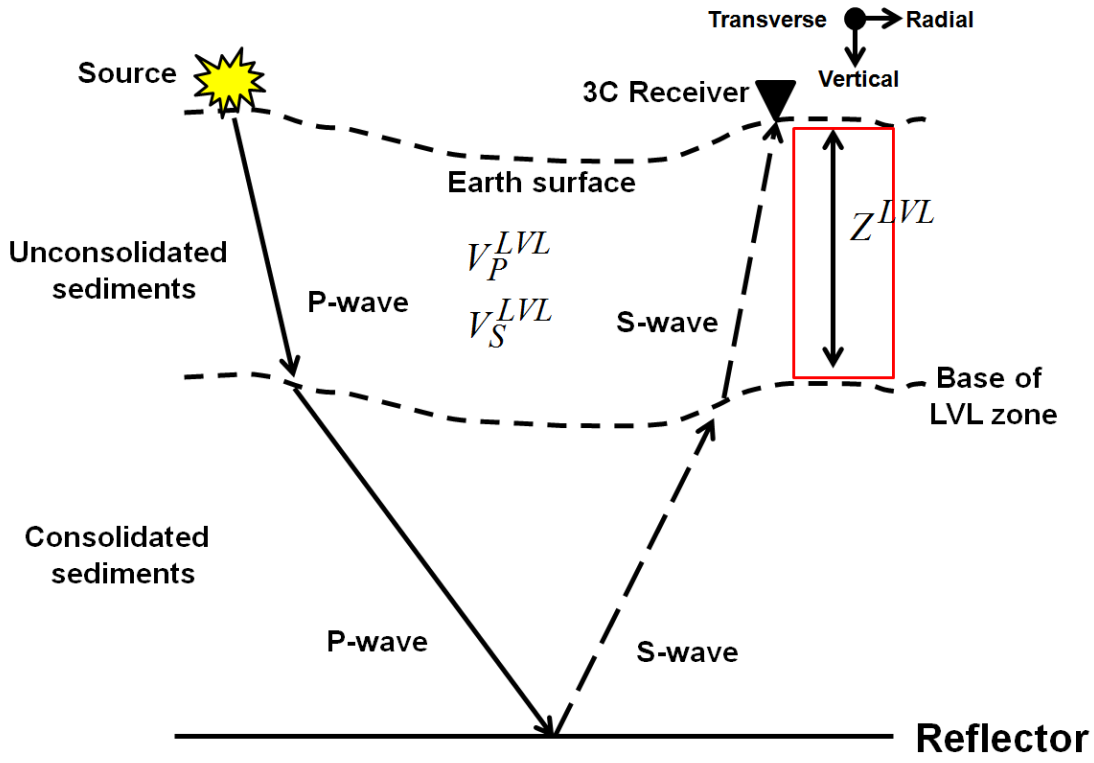

Figure 6.2. A schematic diagram showing the ray paths of P- and S-waves in the presence of a LVL zone where V_P^{LVL} and V_S^{LVL} are respectively P- and S-wave velocities of the LVL zone and Z^{LVL} is the LVL zone thickness.

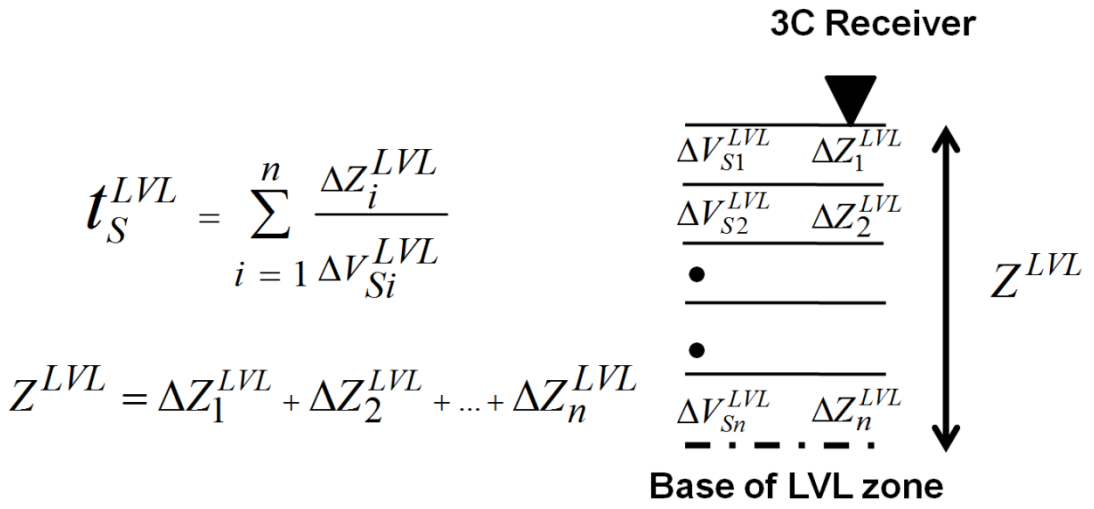

Figure 6.3. A schematic diagram showing the calculation of S-wave LVL statics (t_S^{LVL}) for the red box portion in Figure 6.2 and following Equation 6.1.

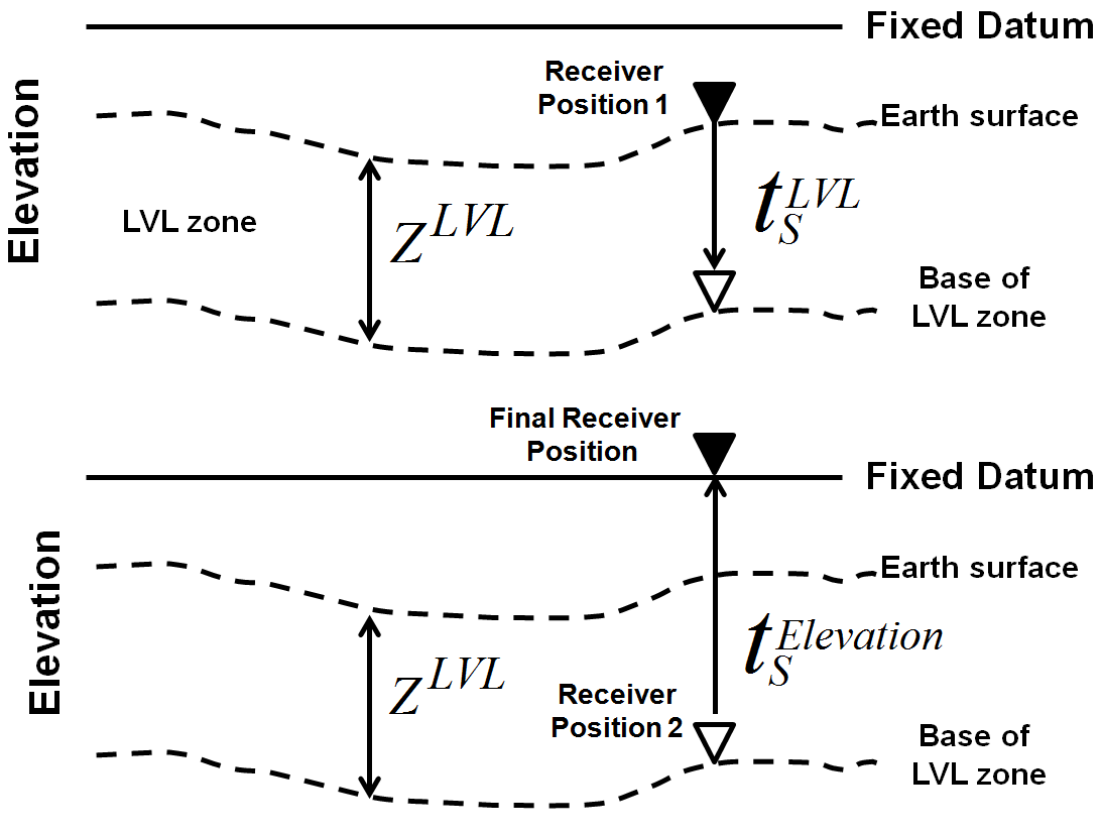

Figure 6.4. A schematic diagram which shows the steps to calculate total S-wave receiver statics. The top diagram shows the application of the S-wave LVL statics (t_S^{LVL}) to bring the receiver down to the base of the LVL zone. The bottom figure shows the application of the elevation statics ($t_S^{Elevation}$) to bring the receiver at a flat datum for further processing (Cox, 1999).

Generally, S-wave statics are several times greater than P-wave statics. Figure 6.12 (for a 2D line) and Figure 6.13 and Figure 6.14 (for a 3D survey) in the later sections show the example from Bradford 3D-3C survey (discussed in details in the next section) that the provided S-wave statics are significantly larger than P-wave statics and they also vary a lot along a 2D line and 3D region. This shows again that proper caution should be taken for the estimation of S-wave statics. Some initial attempts

had been made to calculate and apply S-wave statics using the surface-wave inversion method (Al Dulaijan, 2008 and Roy et al., 2010). The S-wave statics can vary significantly in different survey sites depending on the near-surface S-wave velocities based on geological settings (Roy et al., 2010). In this study, careful analyses have been performed to estimate the near-surface S-wave velocities and S-wave statics from the surface-wave inversion (MASW) method for the Bradford 3D-3C survey. The dataset has generously been provided by GeoKinetics.

6.3 Bradford 3D-3C survey

The Marcellus shale play (Figure 6.5) is one of the largest unconventional plays in the USA. The Middle Devonian Marcellus shale extends from Ohio and West Virginia, northeast into Maryland, Pennsylvania and New York (Koesoemadinata et al., 2011). A 3D-3C wide-azimuth seismic dataset from the Marcellus shale play in Bradford county in Pennsylvania, USA (Figure 6.6) has been used in this study for calculating S-wave statics for horizontal (radial and transverse) receivers using the surface-wave inversion method. The seismic acquisition geometry is shown in Figure 6.7 where the area of 3C receivers is approximately 4 $mile^2$ (10.36 km^2) and the area of sources is approximately 25 $mile^2$ (64.8 km^2). Every receiver line has approximately 96-97 receivers with the receiver interval of 110 ft (33.53 m). The total number of receiver lines is 13 with 880 ft (268 m) of line interval. Since this was a complex survey, the mentioned acquisition parameters are ideal and in reality they are very close but not

exact. The source was 2.2 lb of dynamite at 20 ft depth and a brick source pattern was employed. For the purpose of this study, only the first receiver line (Receiver line: 9001) has been used (Figure 6.8). So, effectively this study has been performed along a 2D line with 96 receivers (3C) and 110 ft of receiver interval (Figure 6.8). The shot gathers have been sorted from the entire 3D dataset for sources along (red solid circles in Figure 6.8) or very close (green solid triangles in Figure 6.8) to the 2D line.

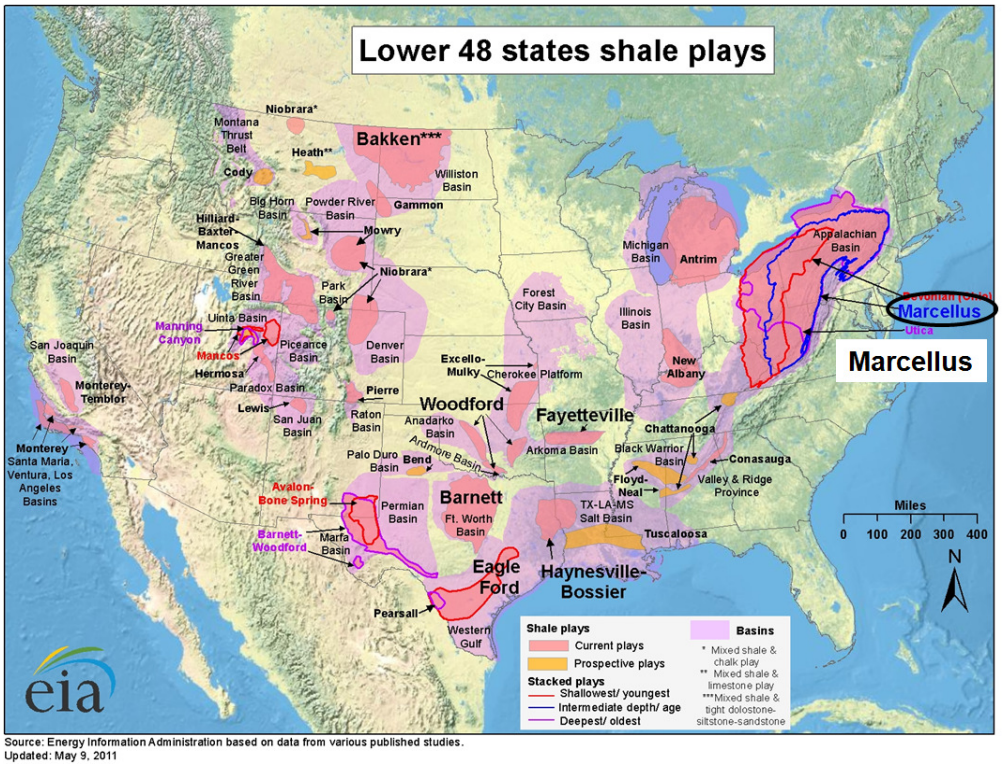

Figure 6.5. The location of the Marcellus shale play in the North America (source: U.S. Energy Information Administration, 2011).

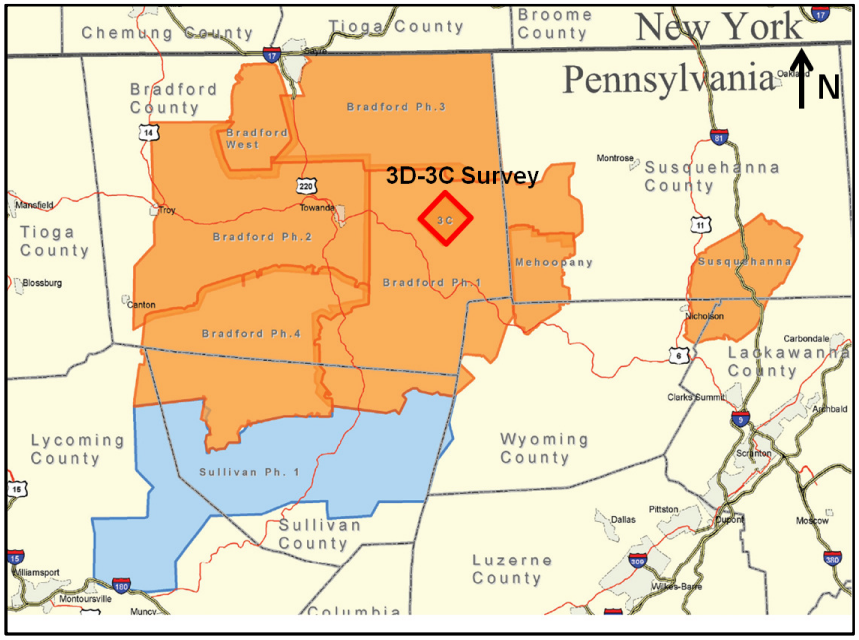

Figure 6.6. The location of the Bradford 3D-3C seismic survey in Pennsylvania, USA (Seismic data source: GeoKinetics).

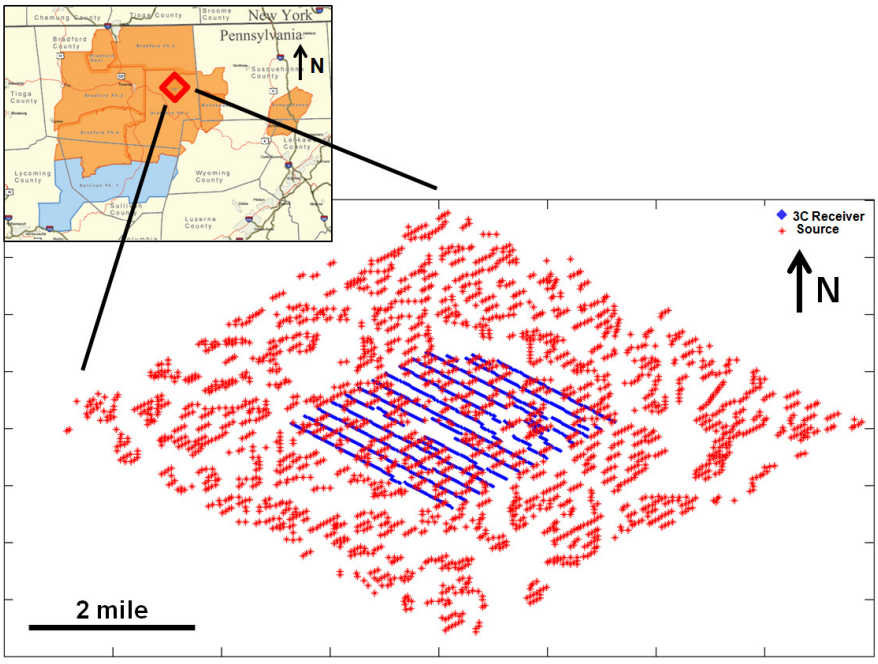

Figure 6.7. The Bradford 3D-3C seismic acquisition pattern showing dynamite sources and 3C receivers.

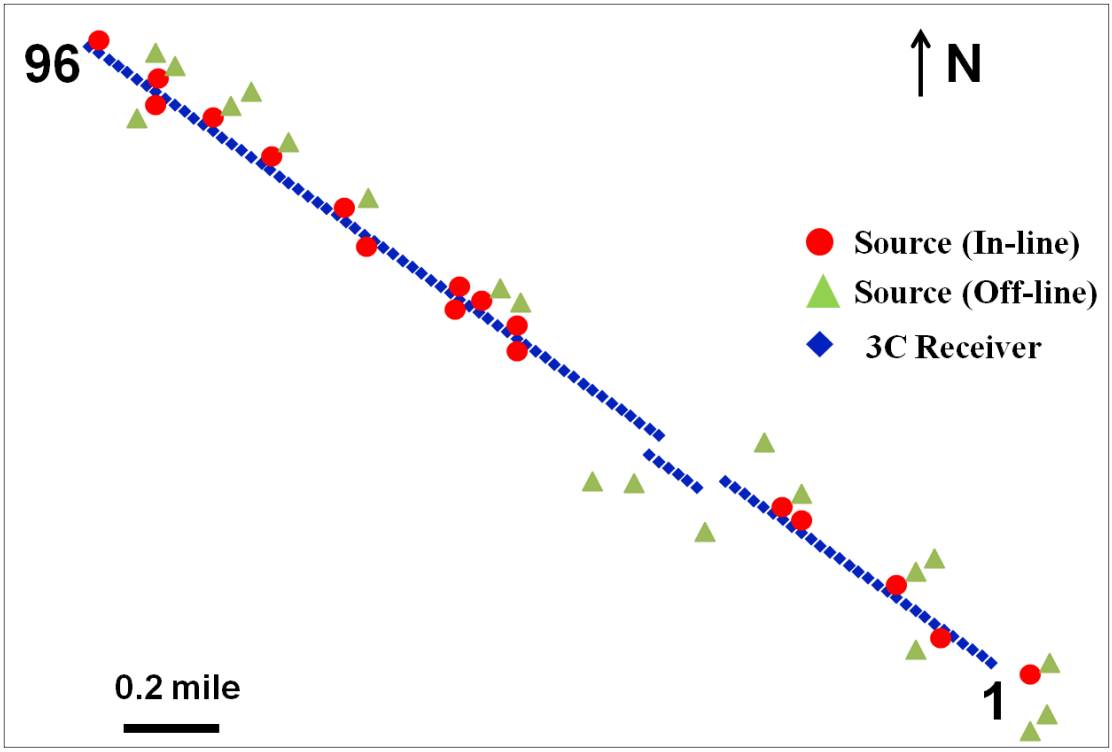

Figure 6.8. The 2D receiver line used in this study showing 3C receivers and dynamite sources. The solid red circles show in-line sources whereas solid triangles show slightly off-line sources.

The survey area has complex near-surface and topography and consequently strong near-surface statics. So, the poor modeling of the near-surface and statics can hinder the study related to azimuthal velocity and S-wave splitting to characterize fracture sets (Gaiser et al., 2011). Originally (as processed by GeoKinetics), common receiver gather (CRG) stacks have been used to estimate long wavelength S-wave statics (Gaiser et al., 2011) along with two passes of PS reflection receiver residual statics. Also, elevation statics have been added using a fixed datum of 1600 ft (488 m) and S-wave replacement velocity of 7700 ft/s (2347 m/s) to obtain the final S-wave receiver

statics. Figure 6.9 shows the elevation profile along the 2D line and Figure 6.10 shows the 3D distribution of elevations for the entire receiver patch. The elevation varies significantly from 1100 ft (335.3 m) to 1450 ft (442 m) from SE to NW along the 2D line as shown in Figure 6.9. Hence, Figure 6.11 shows the strong S-wave elevation statics using flat datum at 1600 ft (488 m) and S-wave replacement velocity of 7700 ft/s (2347 m/s). Figure 6.12 shows the P-wave receiver statics (vary from 15-35 ms) and the S-wave receiver statics (vary from 5-60 ms) together for the 2D line. Figure 6.13 shows the 3D distribution of P- wave receiver statics and Figure 6.14 shows the 3D distribution of S-wave statics. All these statics are plotted using the header values of from the dataset provided by GeoKinetics. Though only 2D line has been used for this survey, still the 3D distributions of elevations and statics provides an overall idea about the survey region.

The steps used in calculating S-wave statics by the data provider are common practice in industry. During this estimation, often a fixed average $\frac{V_P}{V_S}$ is assumed. The goal of this study is to use the surface-wave inversion method for the estimation of S-wave statics and to compare with the provided S-wave statics values estimated in traditional way. The S-wave statics estimated from the surface-wave inversion are not dependent on any PP image or any assumed $\frac{V_P}{V_S}$. They are calculated through a stand-alone process.

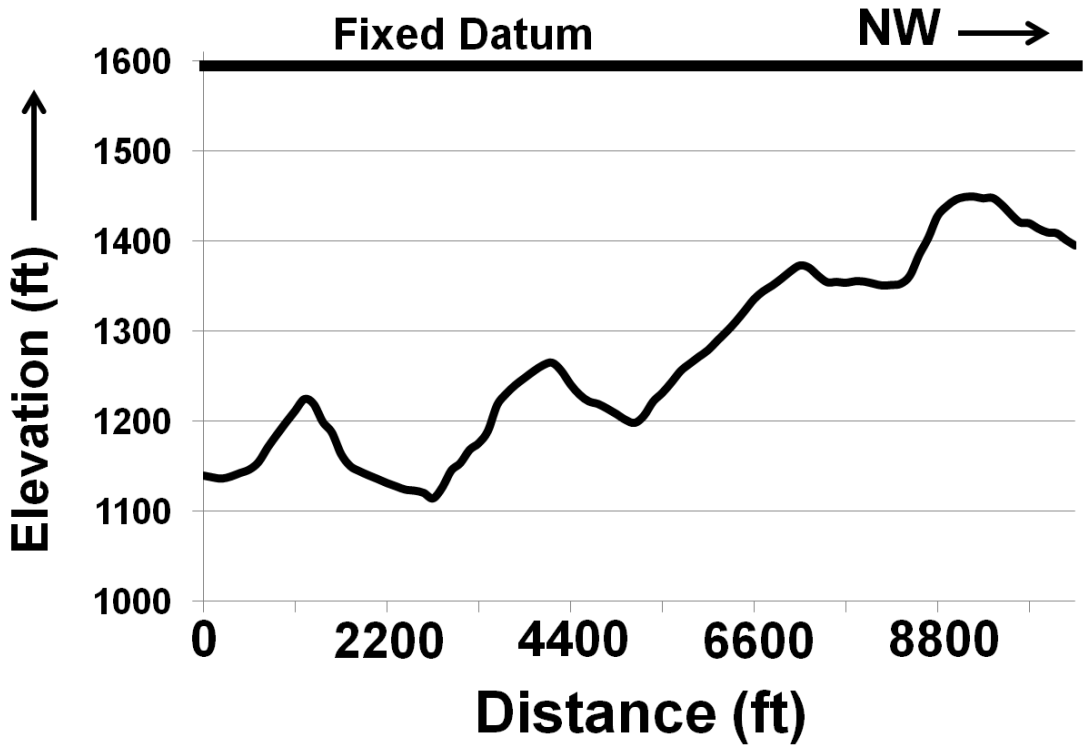

Figure 6.9. The elevation profile for the 2D line used in this study with the fixed flat datum used for further processing steps.

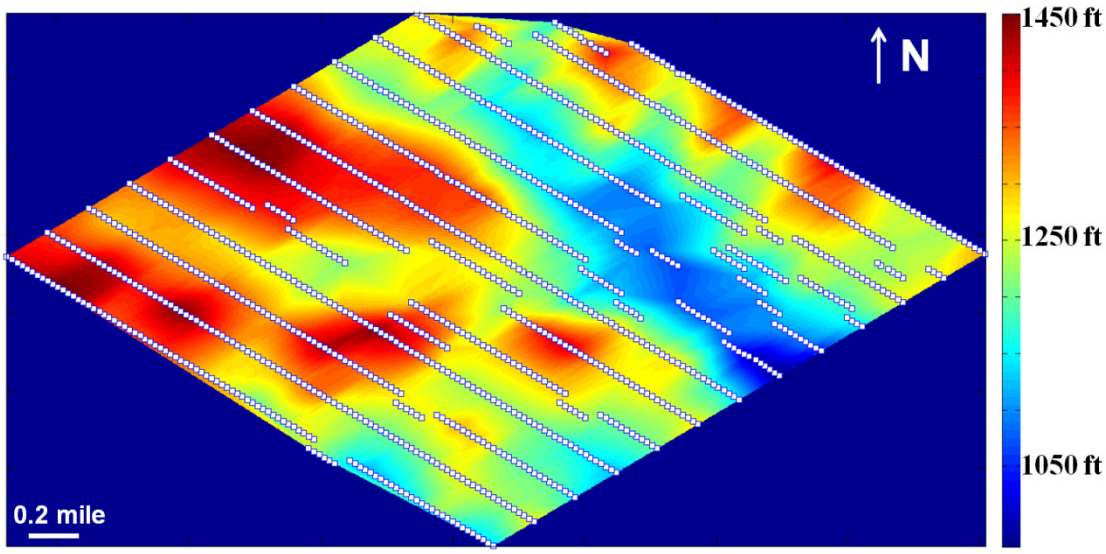

Figure 6.10. The 3D elevation distribution for the entire receiver patch (white squares represent 3C receivers).

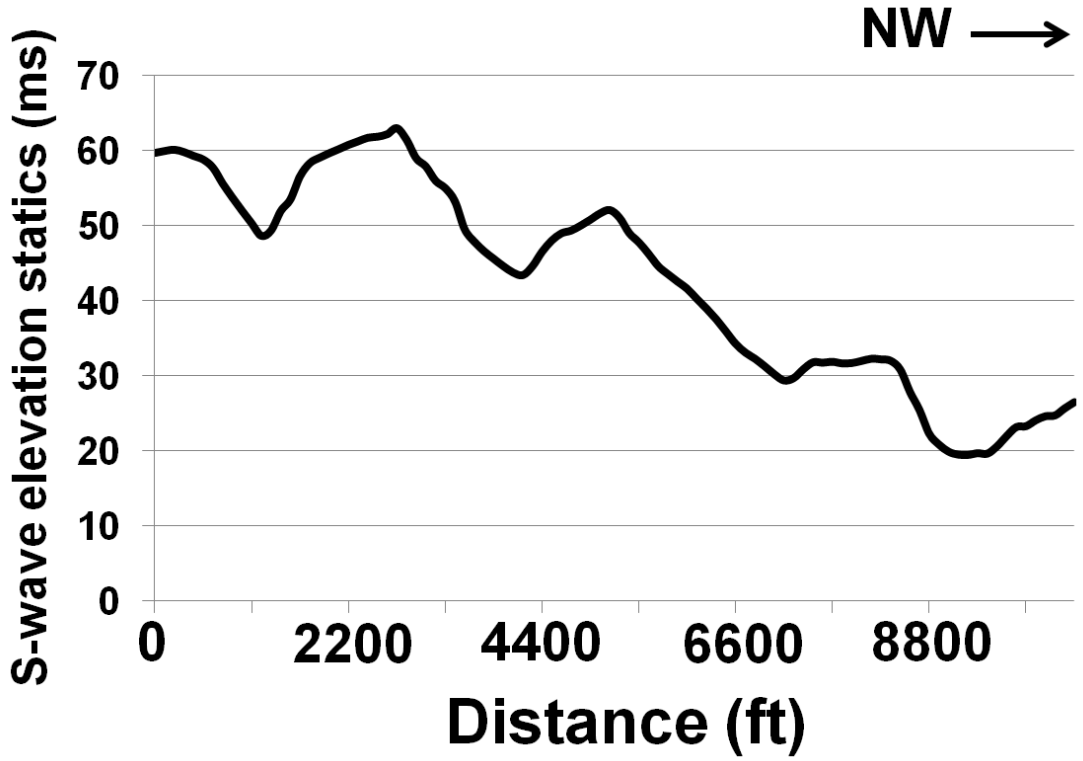

Figure 6.11. The S-wave elevation statics along the 2D line using fixed flat datum of 1600 ft (488 m) and S-wave replacement velocity of 7700 ft/s (2347 m/s).

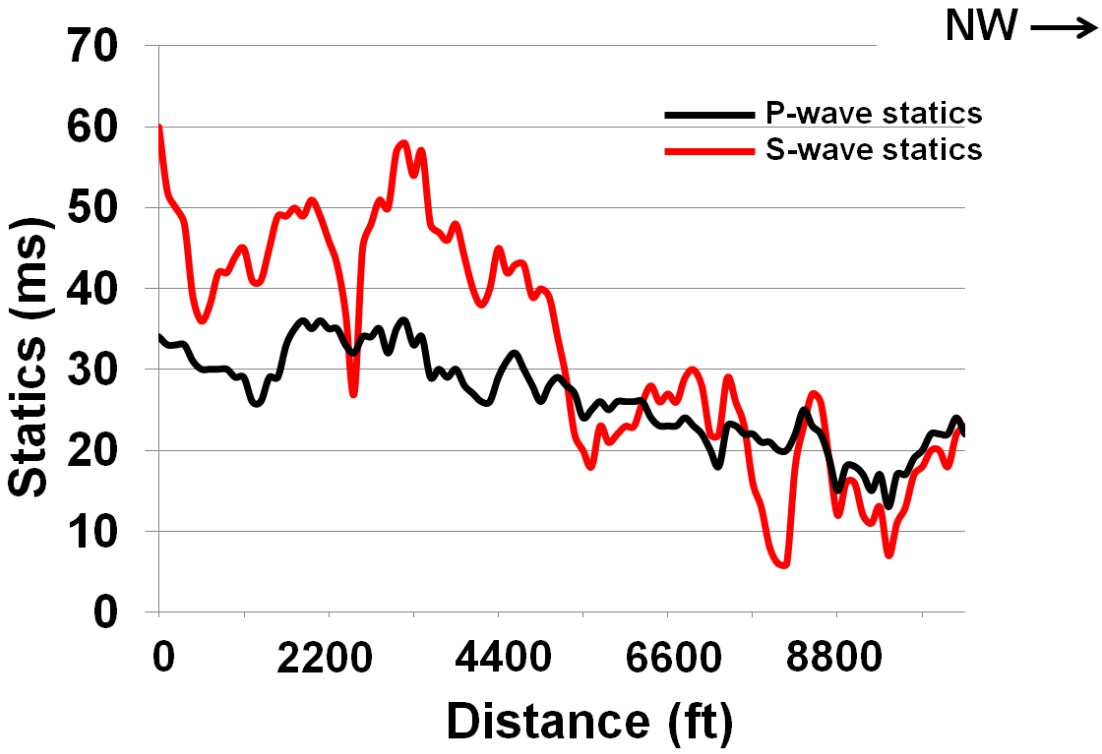

Figure 6.12. The P- and S-wave receiver statics along the 2D line.

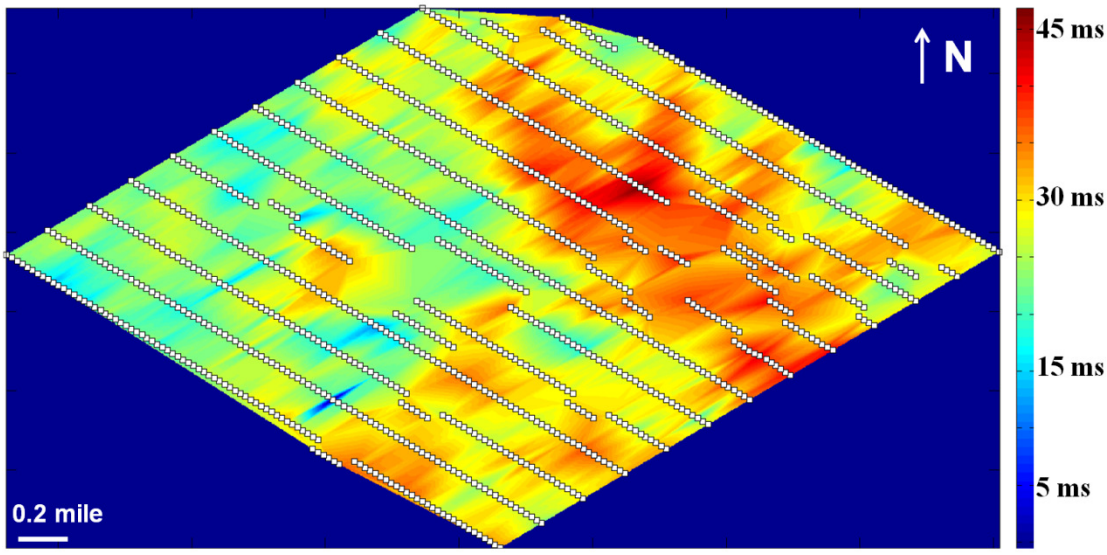

Figure 6.13. The 3D distribution of P-wave receiver statics for the entire receiver patch (white squares represent 3C receivers).

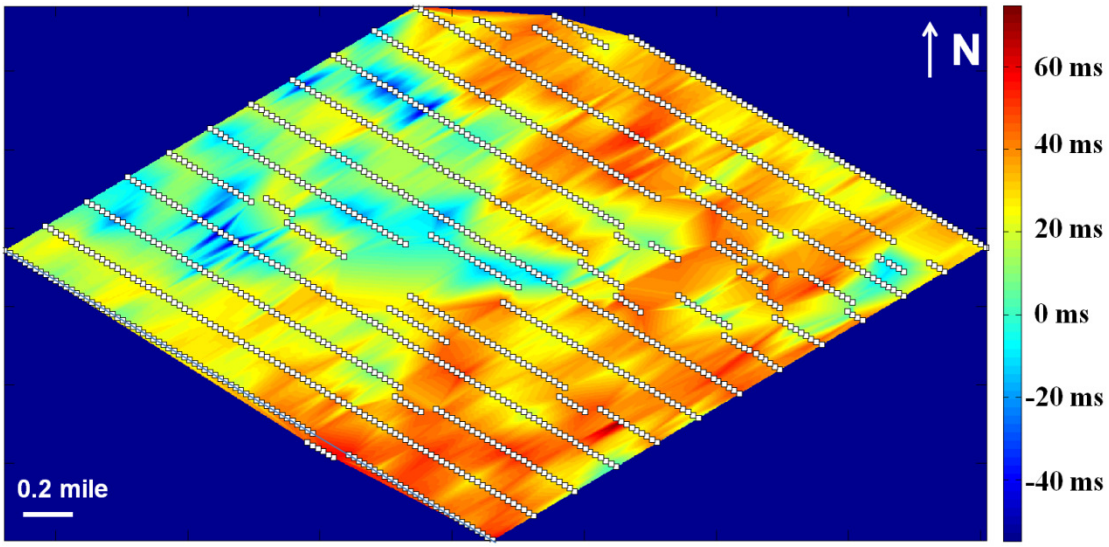

Figure 6.14. The 3D distribution of S-wave receiver statics.

6.4 MASW analysis for Bradford survey

The traditional MASW analysis is applied on the raw shot gathers along the 2D line (Figure 6.8). But due to the lack of in-line shots, there are some irregularities in trace selection for the generation dispersion curves. The number of traces for dispersion analysis varied from 12 to 31 (out of 96 traces) for different shot gathers. Since the survey has 3C receivers, an initial dispersion analysis has been performed for all the components. The available shot gather components are – one vertical (Z), two horizontals (X and Y), and two horizontals after rotation (radial and transverse). Figure 6.15 shows a series of dispersion curves for all these components. As anticipated, the vertical component (Figure 6.15a) shows the most energy for the surface-wave (Rayleigh-wave). The X and radial components show the same range of phase velocities for Rayleigh waves as the vertical component. The phase velocities

vary from 5000–6500 ft/s (1524–1981 m/s). The dispersion curve for the Y component shows the same range of velocities, but after rotation no energy is found for that velocity range (6000±500 ft/s or 1829±152 m/s) for the transverse component. This shows that after rotation the Rayleigh-wave energy has been removed from the transverse component as one should expect only Love-wave for the transverse component and not Rayleigh-wave. This shows that still the vertical component is the best for MASW analysis. But the resultant S-wave velocities can be used for radial and transverse component analysis. For the rest of the analysis, the traditional MASW analysis for vertical component data has been carried out. Though, one can use radial component also to reinforce the vertical component result.

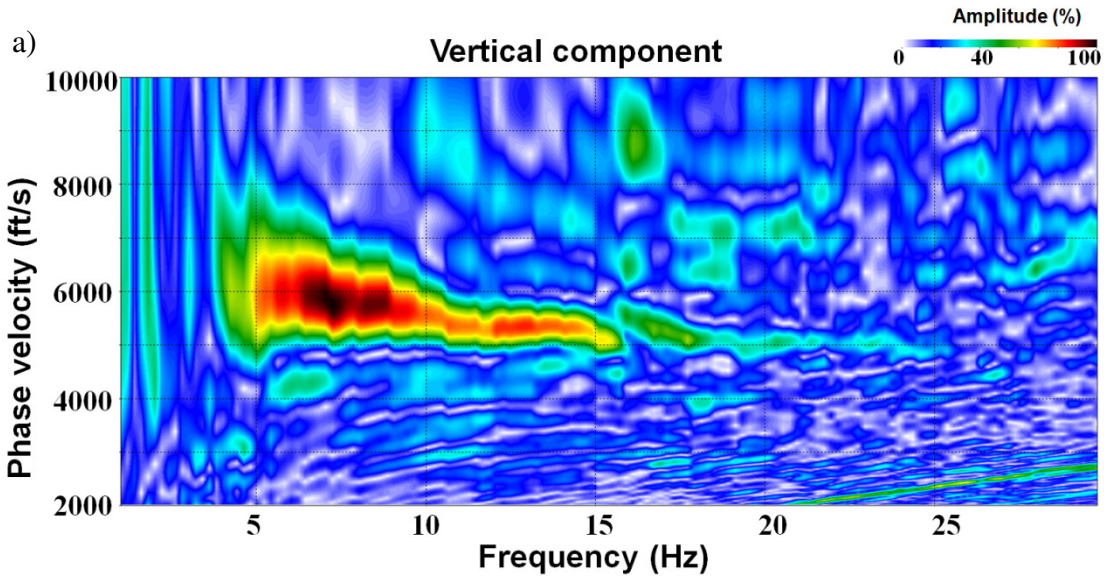

Figure 6.15. The figure shows the dispersion curves for an in-line shot gather related to: a) vertical components.

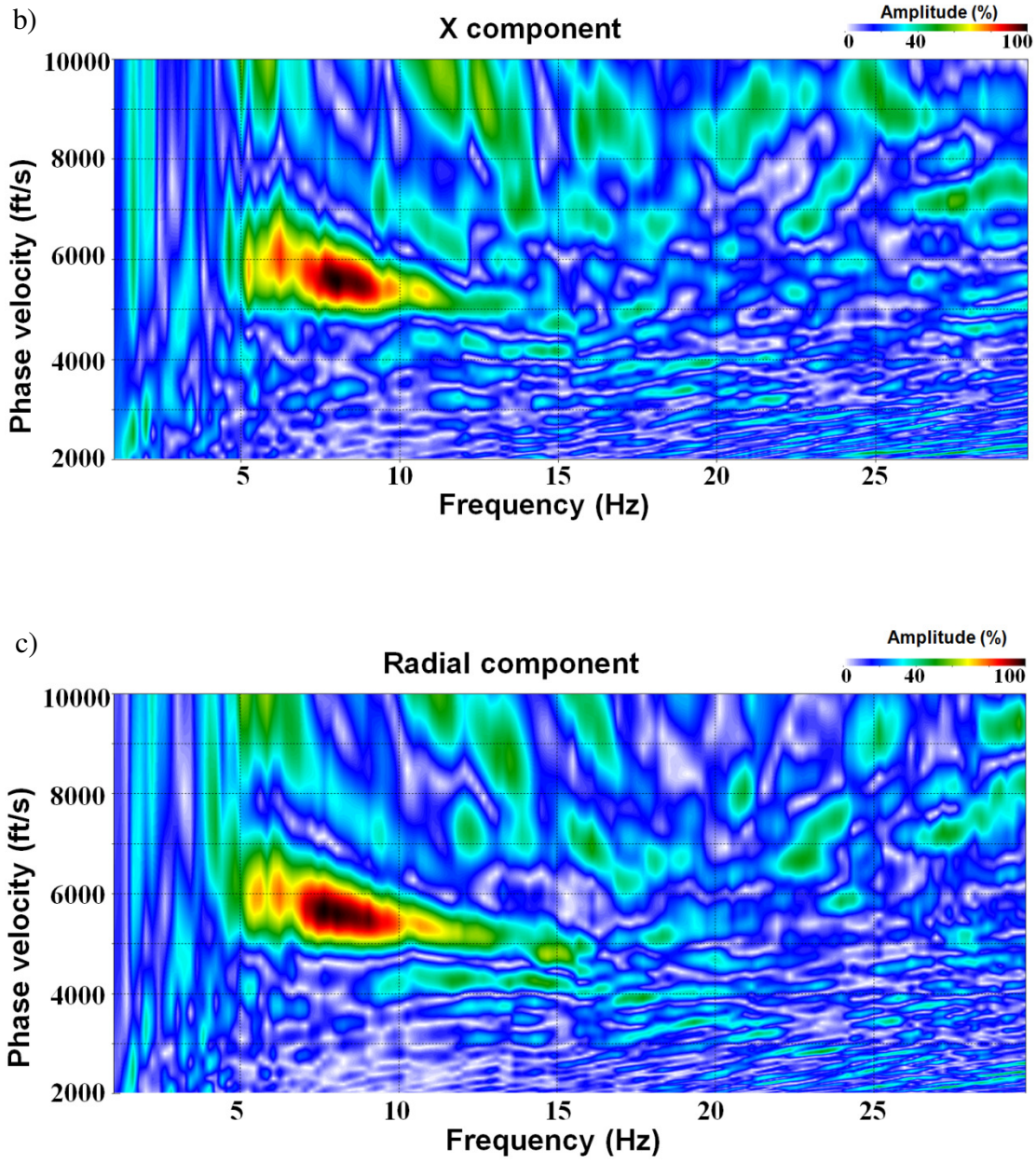

Figure 6.15 (cont.). The figure shows the dispersion curves for an in-line shot gather related to: b) X, c) radial components.

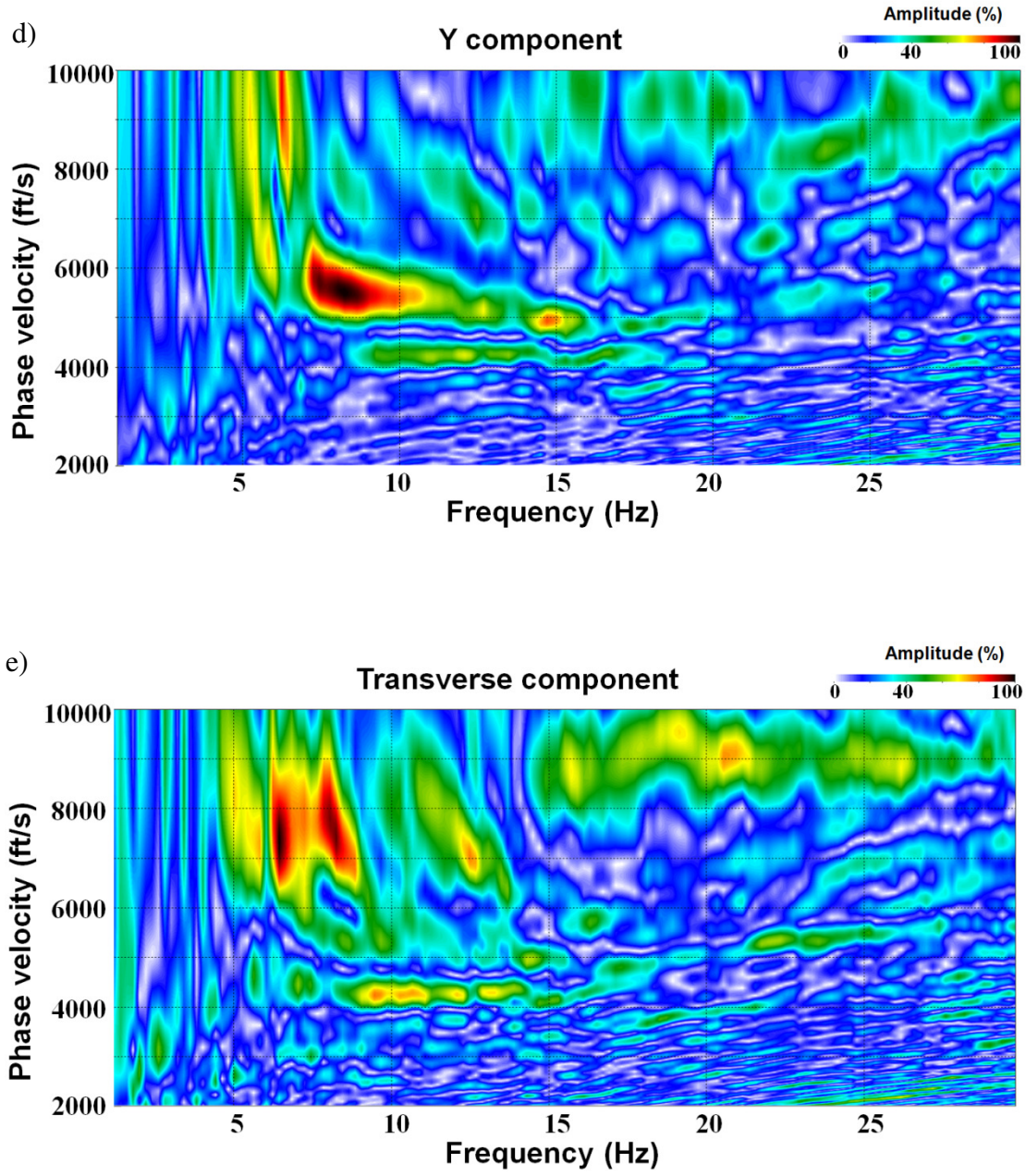

Figure 6.15 (cont.). The figure shows the dispersion curves for an in-line shot gather related to: d) Y, and e) transverse components.

Apart from the scarcity of shots, another practical problem has been encountered for this study which is related to offset distribution for off-line shots. Figure 6.16 shows an off-line shot gather plots with actual source-receiver offset as well as traditional shot gather plot assuming regular offset distribution. The traces plotted with actual offset show the irregularity in trace distribution. The commercial software used for MASW analysis is best suited for the in-line end-on type of shots with regular receiver interval. So, only in-line (or very close to in-line) shots are used for this study (Figure 6.8). To handle this problem in future, a MATLAB code has been written to generate dispersion curves following the same theory of MASW (Park et al., 1998). The advantage of this code is that one can directly input the exact source-receiver offset value (regular or irregular) from seismic data headers or observer's log for the calculation of dispersion curves compared to regular offset only. Figure 6.17 shows the comparison of dispersion curves related to a slightly off-line shot (black circle in Figure 6.16a) for vertical component using the traditional software and the new code. The results show that the new code is not only more practical but the results are more meaningful. The range of phase velocities from the new code is similar to the in-line shot results (Figure 6.15a); but that from the commercial MASW software is inaccurate (phase velocities are almost 16 % higher). The reason is the wrong input of offset (or receiver interval) for the software which is forced to be regular whereas the actual offset is irregular. This comparison shows that even for a slightly off-line shot, the results may vary if proper offset is not used. The new MATLAB code can be used for other future analyses when several off-line shots are

present, especially for a complex 3D survey like Bradford. But at the same time, one should be careful of using too much of off-line shots because out of the X-Z plane energy for Rayleigh waves may intrude for 2D lines. The extraction of the surface-wave dispersion curves from 3D survey (Boiero et al., 2011) is critical and more attention is required in future.

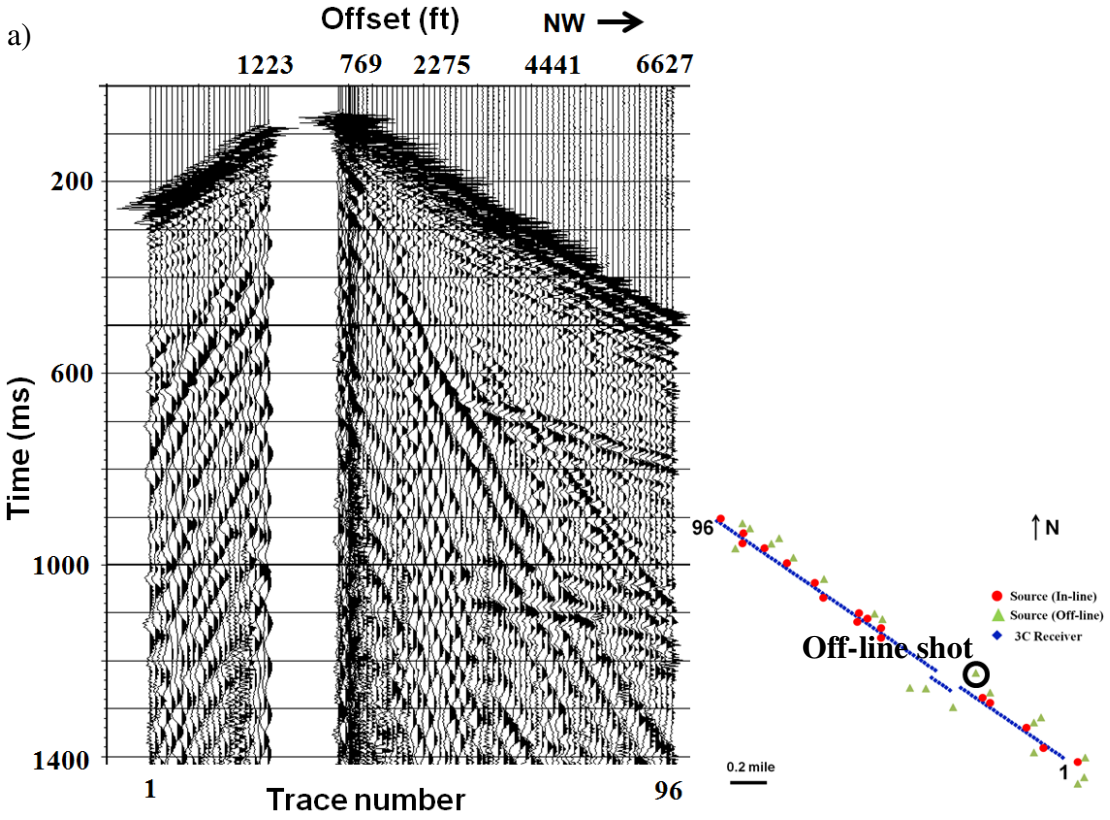

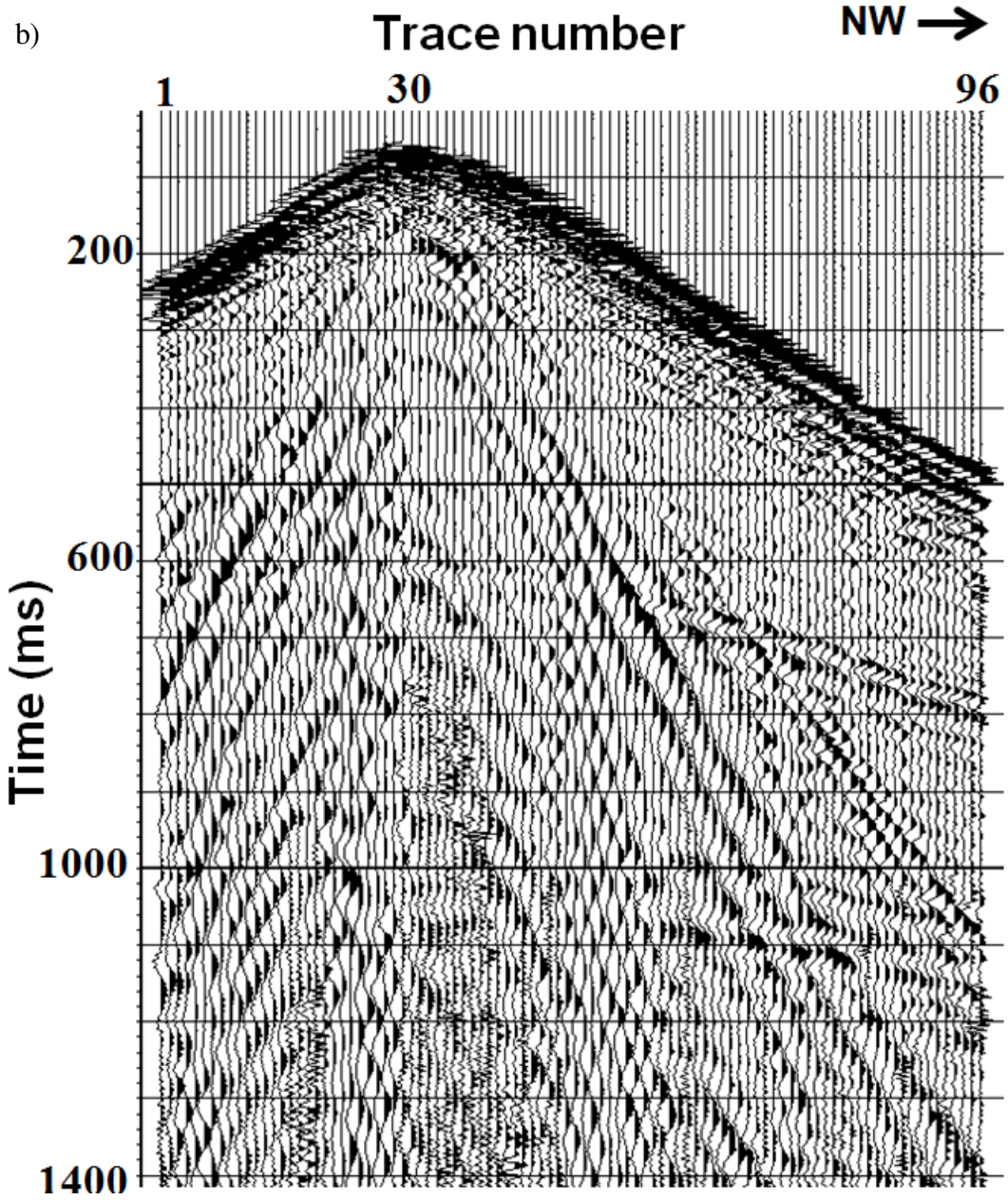

Figure 6.16. The raw shot gather from an off-line shot (black circle in the inset figure) plotted with- a) actual source-receiver offset, and b) traditional plot assuming regular offset distribution (AGC applied for display purposes).

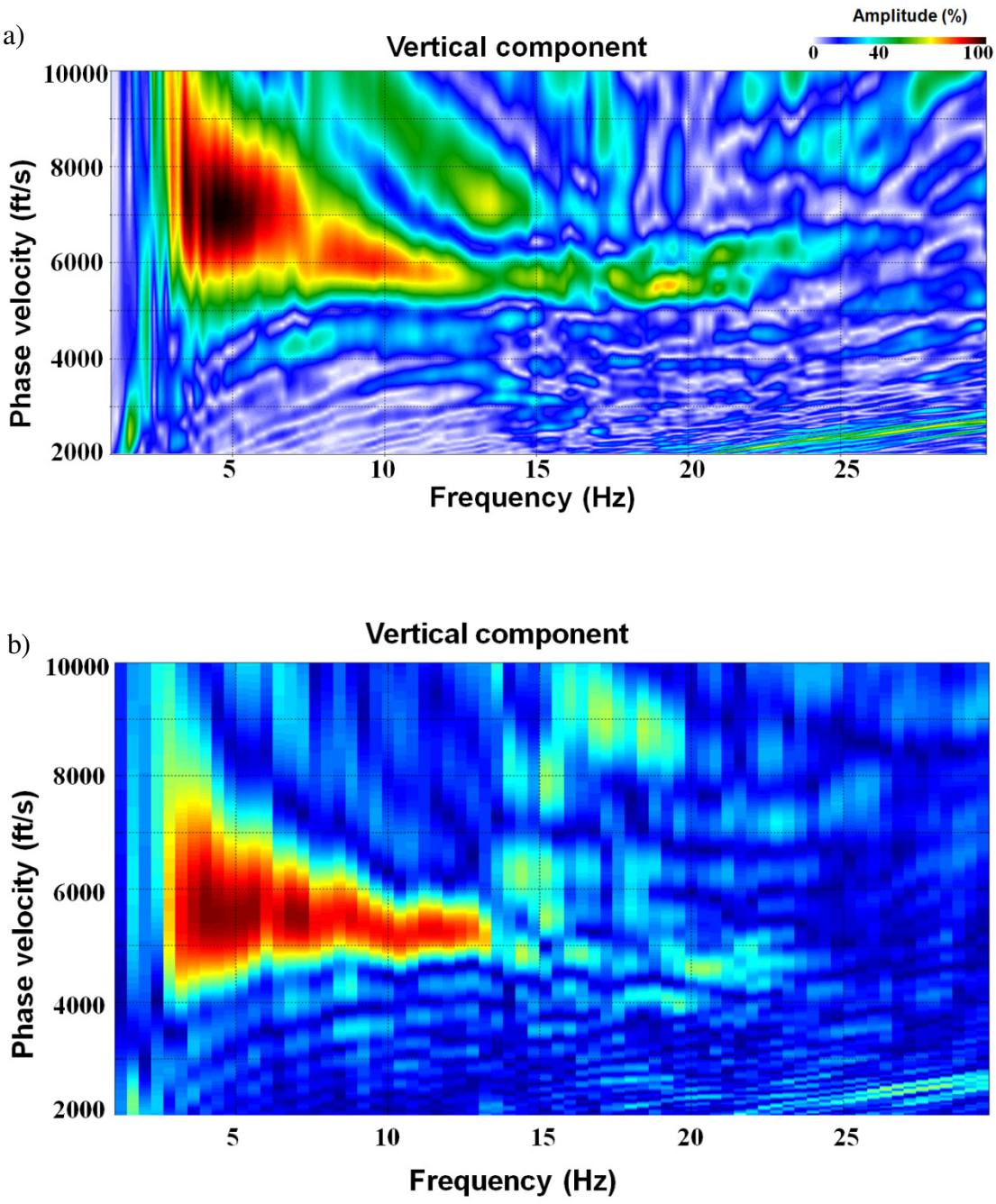

Figure 6.17. Dispersion curves for the same shot gather in Figure 6.16 using- a) traditional software with regular offsets, and b) MATLAB code with actual source-receiver offset.

The traditional MASW analysis has been continued along the 2D line for the vertical component and the resultant 2D S-wave velocity structure is shown in Figure 6.18. The estimated S-wave velocities vary from 5200-7200 ft/s (1585-2194.56 m/s) for a 530 ft (161.5 m) deep earth model. A sharp change from lower to higher velocities has been observed at around 200 ft (61 m) depth. I have considered that boundary as the base of LVL zone. Then equations 6.1 – 6.3 have been applied to obtain the final S-wave receiver statics from the surface-wave inversion (MASW). The S-wave velocities obtained from the MASW method are always smooth as the velocity at each receiver location is the representative average velocity of the used receiver offset spread (or number of traces). For some shot gathers in this study, even thirty traces (i.e. 3300-3400 ft or 1006-1036 m of offset spread) have been used to construct an acceptable dispersion curve with high S/N. So, the estimated S-wave velocity model is a smooth one. Hence, the calculated S-wave LVL statics and consequently the total S-wave receiver statics should represent a smooth long-wavelength statics. Figure 6.19 shows the comparison between the S-wave receiver statics provided by GeoKinetics (solid red line) and that generated via MASW analysis (solid blue line). But, both these statics include elevation statics part. As shown in Figure 6.9, there is a significant change in topography along the 2D line. So, a strong influence of the elevation statics is present and hence the elevation statics part has been decoupled from the total S-wave receiver statics. Figure 6.20 shows S-wave elevation statics in green (using 1600 ft (488 m) flat datum, S-wave replacement velocity of 7700 ft/s (2347 m/s) and LVL zone thickness of 170 ft or 52 m), S-wave LVL statics in black

(varying from 25-42 ms), and the total S-wave receiver statics in blue (varying from 10-55 ms) which are all estimated in this study. As anticipated, a smooth S-wave LVL statics has been observed as the input S-wave velocities from MASW are smooth averaged velocities. Figure 6.21 shows the comparison between the S-wave LVL statics from this study and a smoothed S-wave LVL statics (a moving average has been applied for 25 points i.e. 2640 ft or 805 m) from GeoKinetics (with a bulk shift of 20 ms). Since both are averaged now, they show good correlation. Given the fact, that only few shots have been used for the 2D line and a smoothed velocity has been used, the results are encouraging. The full use of 3D geometry and more number of shots in future may result in better estimation. Figure 6.22 shows S-wave LVL statics example from the Meteor Crater study (Chapter 3) where we have shot in-between every receiver along a 2D line. The offset range used for each shot during the MASW analysis for the Meteor Crater survey was around 72 m. So, the resultant S-wave velocities and hence LVL statics are less smooth compared to the Bradford study. Consequently, the LVL statics show higher resolution. In addition, the smooth velocity results from MASW can be further updated (as discussed in Chapter 4 and 5) to get sharper velocity structures and hence S-wave statics. Nevertheless, we recommend using these S-wave statics obtained from current analysis primarily in the multicomponent processing flow followed by residual statics corrections, stacking and migration for the future work.

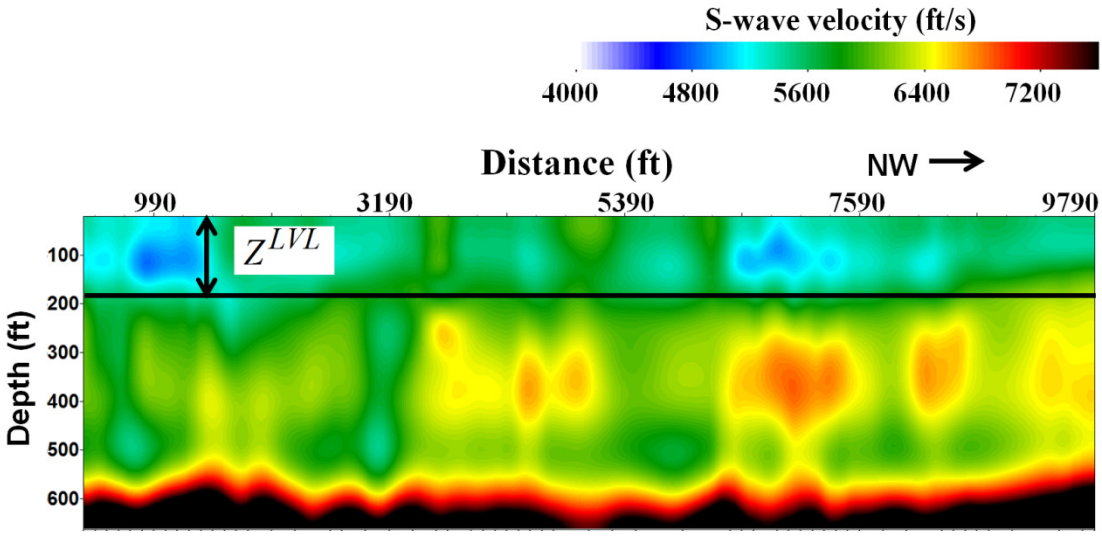

Figure 6.18. The 2D S-wave velocity model (plotted from the ground surface: 0 m) from surface-wave inversion (MASW).

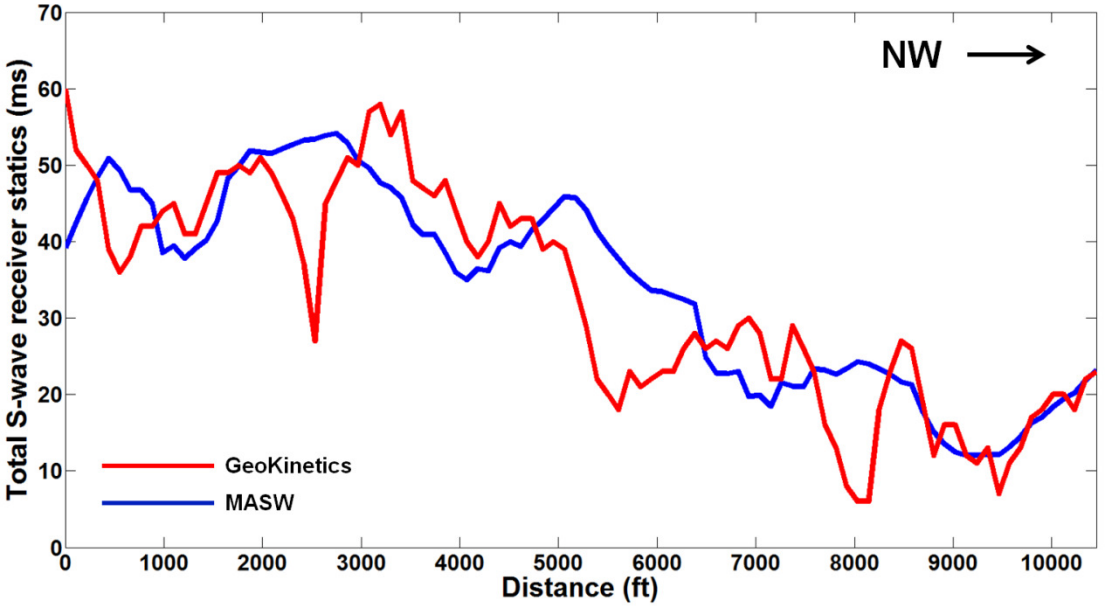

Figure 6.19. The total S-wave receiver statics from GeoKinetics (solid red line) and from this study (solid blue line).

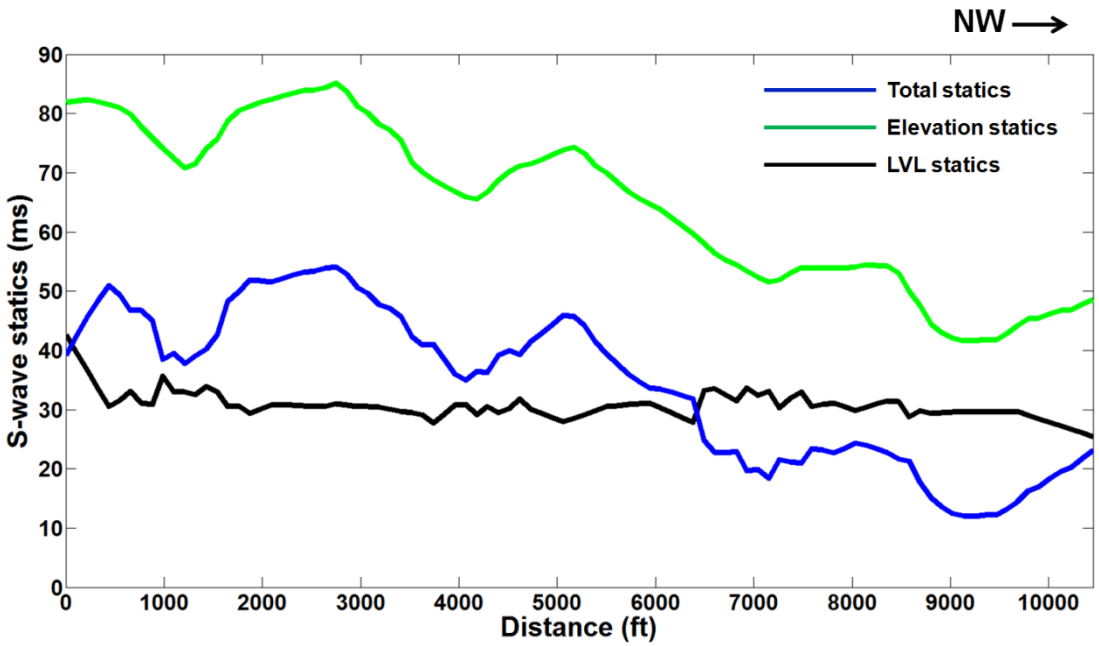

Figure 6.20. The S-wave elevation (green), LVL (black), and total receiver statics (blue) estimated using surface-wave inversion (MASW) method and equations 6.1-6.3.

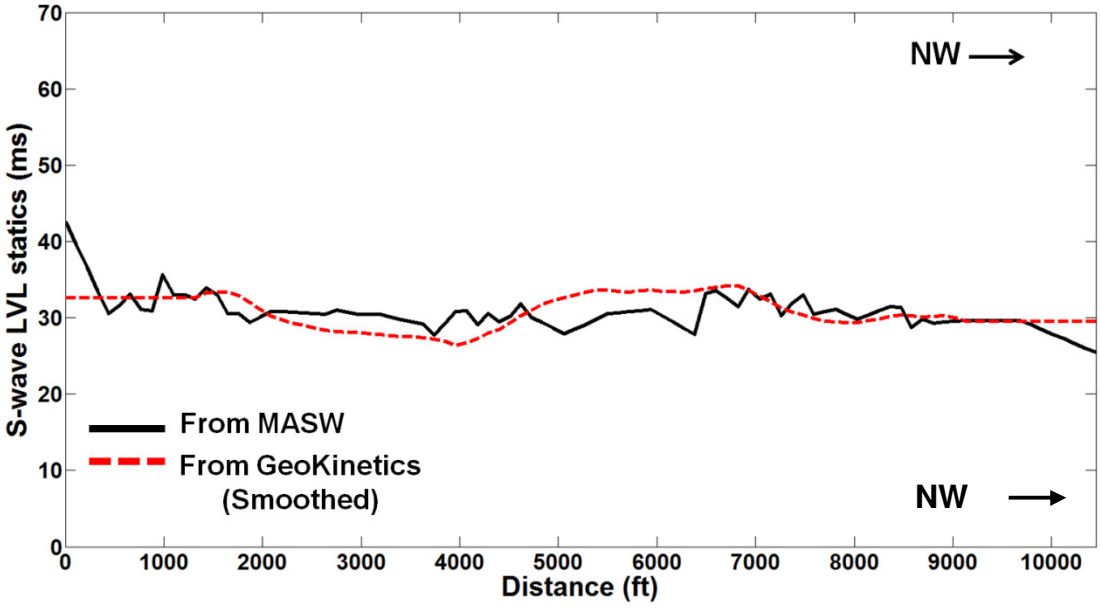

Figure 6.21. The figure shows S-wave LVL statics - from the surface-wave inversion (MASW) method (solid black line) and from GeoKinetics after applying a smoothing operator (dashed red line).

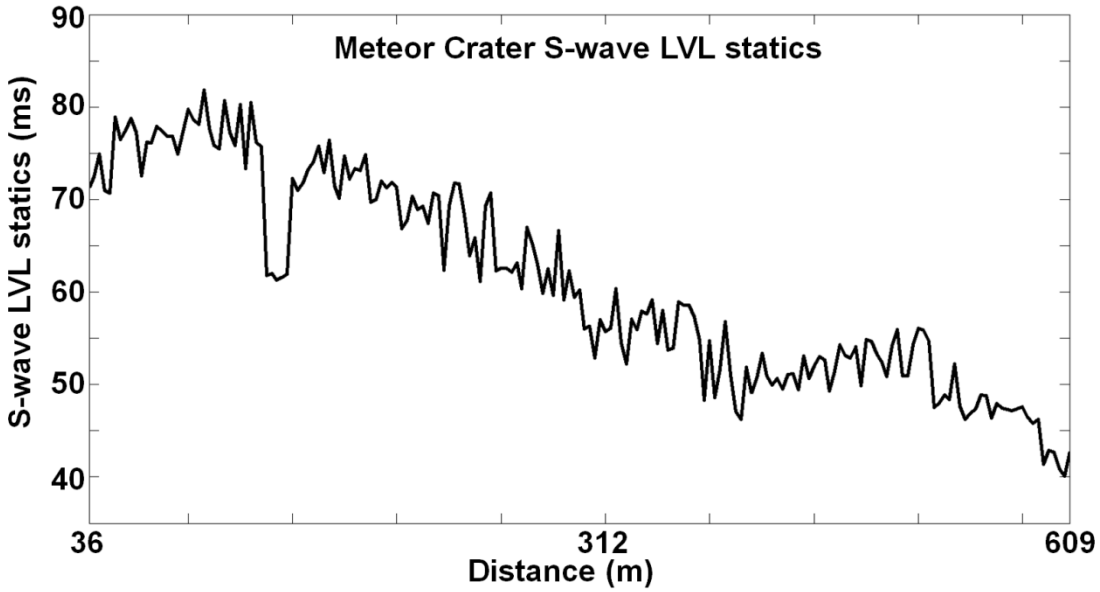

Figure 6.22. The S-wave LVL statics (using MASW) for a 2D line from the Meteor Crater survey.

6.5 Conclusions

The seismic datasets from the Bradford 3D-3C survey have been analyzed to estimate the near-surface S-wave velocity structure using a surface-wave inversion (MASW) method. For the purpose of this study, only a 2D line has been used. The S-wave velocities vary from 5200-7200 ft/s (1585-2194.56 m/s) for a 530 ft (161.5 m) deep model. Then, the resultant S-wave velocity structure has been used to estimate the S-wave receiver statics. First, the S-wave LVL statics is calculated which is in the range of 25-42 ms. Then the LVL statics is subtracted from the elevation statics to obtain the final total S-wave receiver statics which vary from 10-55 ms. The results are then compared with the S-wave receiver statics provided by GeoKinetics (for both total and LVL statics). A 2640 ft (805 m) smoothing is applied to the GeoKinetics S-wave LVL statics to compare with the LVL statics from MASW. The results correlate well

showing that the statics obtained in this study is a smooth long-wavelength type of statics. The S-wave statics calculation discussed in this chapter is a stand-alone process and is not dependent on any PP imaging or results.

Chapter 7

Density prediction from shear–wave velocities

7.1 Introduction

We continuously seek better seismic velocities (both P- and S-waves) and densities for different purposes (calculating accurate synthetic seismograms, better initial models or constraint for inversion, estimating rock properties, fluid factors). Sometimes both seismic velocities and bulk densities are available from the well log or other available sources (drill cores, previous works etc.). But sometimes this is not the case. Gardner et al. (1974) provided a popular empirical relationship to relate bulk density (ρ) to P-wave velocity (V_P). This is the standard relationship in the industry to predict an unknown density. But, only few attempts had been made (Miller and Stewart, 1990; Dey and Stewart, 1997; Potter and Stewart, 1998) to test the relationship between density and S-wave velocities (V_S). V_S should be useful to predict densities from the S-wave as it is a good indicator of lithologies and not affected significantly by fluid saturation compared to P-waves. In this paper, a modified Gardner's relationship (Potter and Stewart, 1998) has been used to predict bulk densities from S-wave velocities. The modified relationship has first been verified with deep well-log datasets from Bradford survey (Marcellus shale), Pennsylvania.

Then, seismic data sets have been analyzed from significantly different settings to estimate S-wave velocities (from surface-wave inversion [MASW]) and followed by the density prediction. I have used varied seismic datasets such as – a) synthetic data from finite-difference modeling for layered elastic media; b) physical modeling data for a uniform blank glass block using ultrasonic measurement facilities at the Allied Geophysical Laboratories (AGL), University of Houston; and field data from- c) the Yellowstone-Bighorn Research Association (YBRA) field camp at Red Lodge, Montana; and d) the Barringer (Meteor) Crater, Arizona. Modeling data are useful to test the density prediction using surface-wave inversion method (MASW) as all properties (V_P, V_S, and ρ) are known. The density prediction from seismic velocities is more used and dependable for deeper lithologies. The goal of this study is to test density-velocity relationships for the near-surface also. The field data used in this study is perfect to test the dependability of these relationships for the near-surface as well as for varied geological settings and rock properties.

7.2 Density prediction from seismic velocities

Gardner et al. (1974) established an empirical relationship (Figure 7.1 and Equation 7.1) based on a broad range of P-wave velocities and relatively narrower range of bulk densities for the dominant sedimentary rocks throughout wide range of geological settings. The range of data samples contained depths less than 25000 ft (7622 m) and P-wave velocities more than 5000 ft/s (1524 m/s) i.e. more than P-wave velocity in water. The Gardner's relationship can be represented as:

$$\rho = aV_P^b \tag{7.1}$$

$$\log_{10}\rho = \log_{10} a + b \log_{10} V_P \tag{7.2}$$

where, ρ is the bulk density in gm/cc, a and b are empirical parameters and V_P is the P-wave velocity in m/s or ft/s. The value of a = 0.23 when V_P is in ft/s and the exponent b = 0.25. Densities for most of the common sedimentary rocks fall in the neighborhood of the Gardner's line with exceptions such as coals and evaporites.

On the other hand, the use of multicomponent data and increasing availability of S-wave velocities have opened up the avenue to use S-wave velocities also for predicting bulk densities. Also, S-wave velocities can be used when P-wave velocities are unavailable or affected by the presence of any fluid (e.g. water-table, gas cloud etc.). A modified Gardner's relation for S-wave velocities was provided by Potter and Stewart (1998) where a = 0.37, b = 0.22, and V_S (instead of V_P) in ft/s (Equation 7.3) where V_S is again greater than 5000 ft/s (1524 m/s). So, the modified Gardner's equation for V_S can be expressed as:

$$\rho = 0.37V_S^{0.22} \tag{7.3}$$

$$log_{10}\,\rho = \; log_{10}(0.37) + \; 0.22\, log_{10}\, V_S \tag{7.4}$$

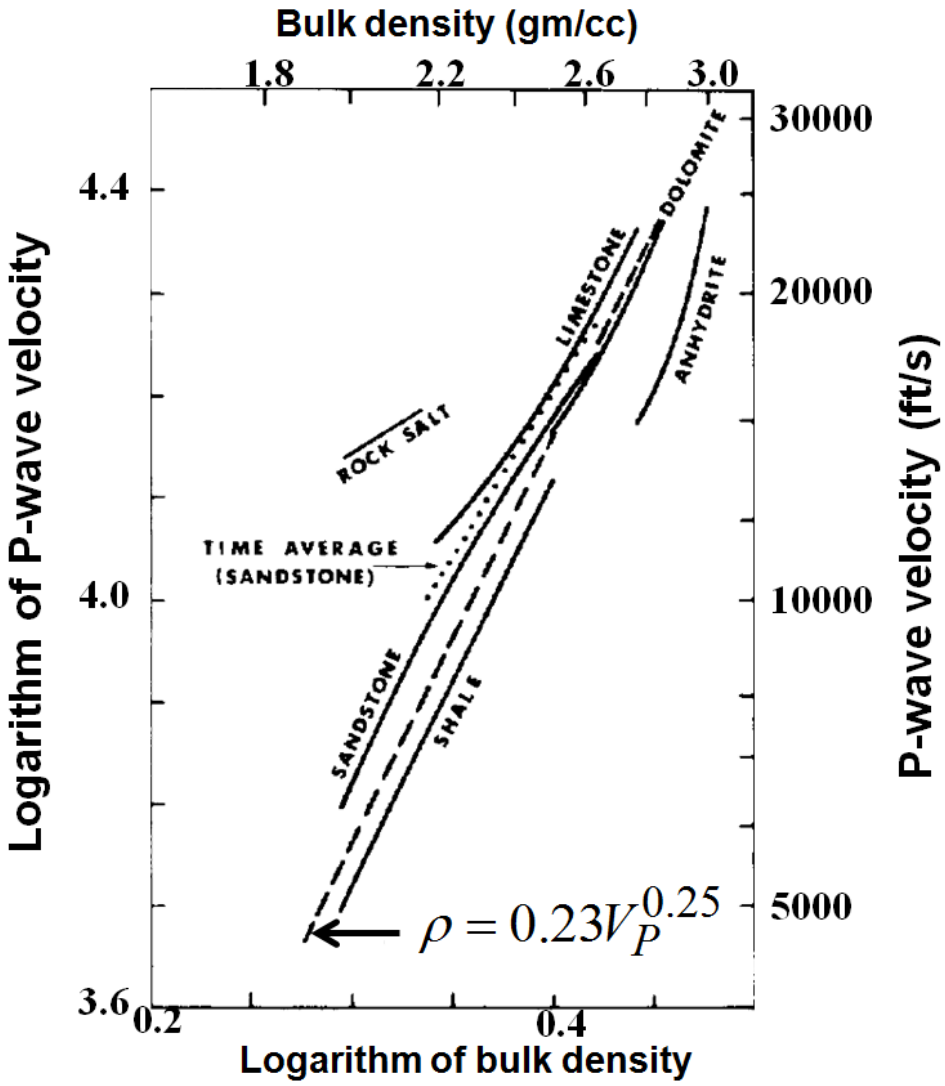

Figure 7.1. The original Gardner's equation for P-wave velocities greater than 5000 ft/s or 1524 m/s (modified from Gardner et al., 1974).

The above mentioned study used the well log data from the Blackfoot field located near Strathmore, Alberta, Canada with the focus on the Glauconitic member of the lower Cretaceous. The formation includes a shale-filled channel and a porous sand-filled channel (Potter and Stewart, 1998). Based on their analyses, the paper proposed the modified Gardner's equation (Equation 7.3).

We first tested the proposed relationship (Equation 7.3) with deep well-log data from Bradford survey at Pennsylvania. The well log datasets were generously provided by GeoKinetics and Anadarko. The well was situated at the center of a 3D-3C seismic survey at Bradford, Pennsylvania (Figure 7.2). The key intervals are the Tully limestone, Upper and lower Marcellus black shale with thin Cherry Valley limestone sandwiched in between (Figure 7.3). The well log dataset contains P- and S-wave sonic logs, gamma ray log, neutron porosity, and density log. Figure 7.4 shows all of these logs together along with $\frac{V_P}{V_S}$ for all intervals. Then, gamma ray, V_P, V_S, and density logs have been plotted for individual intervals only. For the Tully limestone and Cherry Valley limestone intervals, we note the low gamma ray values and high velocities; whereas for the upper and lower Marcellus shale, high gamma ray values and low velocities have been observed (Figure 7.5 and Figure 7.6). The density logs show higher values for limestone intervals and lower values for shale (Figure 7.7 and Figure 7.8). These log properties help to recognize the individual formations. Then, the modified Gardner's equation has been applied on the S-wave sonic log for each interval and plotted with actual estimated density log (Figure 7.7 and Figure 7.8). The

predicted densities from V_P have also been plotted in the same figure. Next, we tried different b values to predict densities from S-wave velocities to find better match for different lithological intervals. For the Tully limestone interval, $b = 0.218$ worked better (Figure 7.7) whereas for the Marcellus shale formation $b = 0.22$ was enough to provide a good match (Figure 7.8). The modified Gardner's relation (Equation 7.3) worked well for all these intervals with an error in b values of -0.002 (1%). The predicted densities from P-wave velocities actually show more error (or bulk shift in density values) than that from S-wave velocities for shale intervals. These tests with real well-log data encouraged us to continue the application of the modified Gardner's equation related to S-wave velocities for seismic datasets, especially to test it for the near-surface with velocities less than 5000 ft/s (1524 m/s). The S-wave velocities applied in the following sections have been estimated from seismic datasets using the surface-wave inversion (MASW).

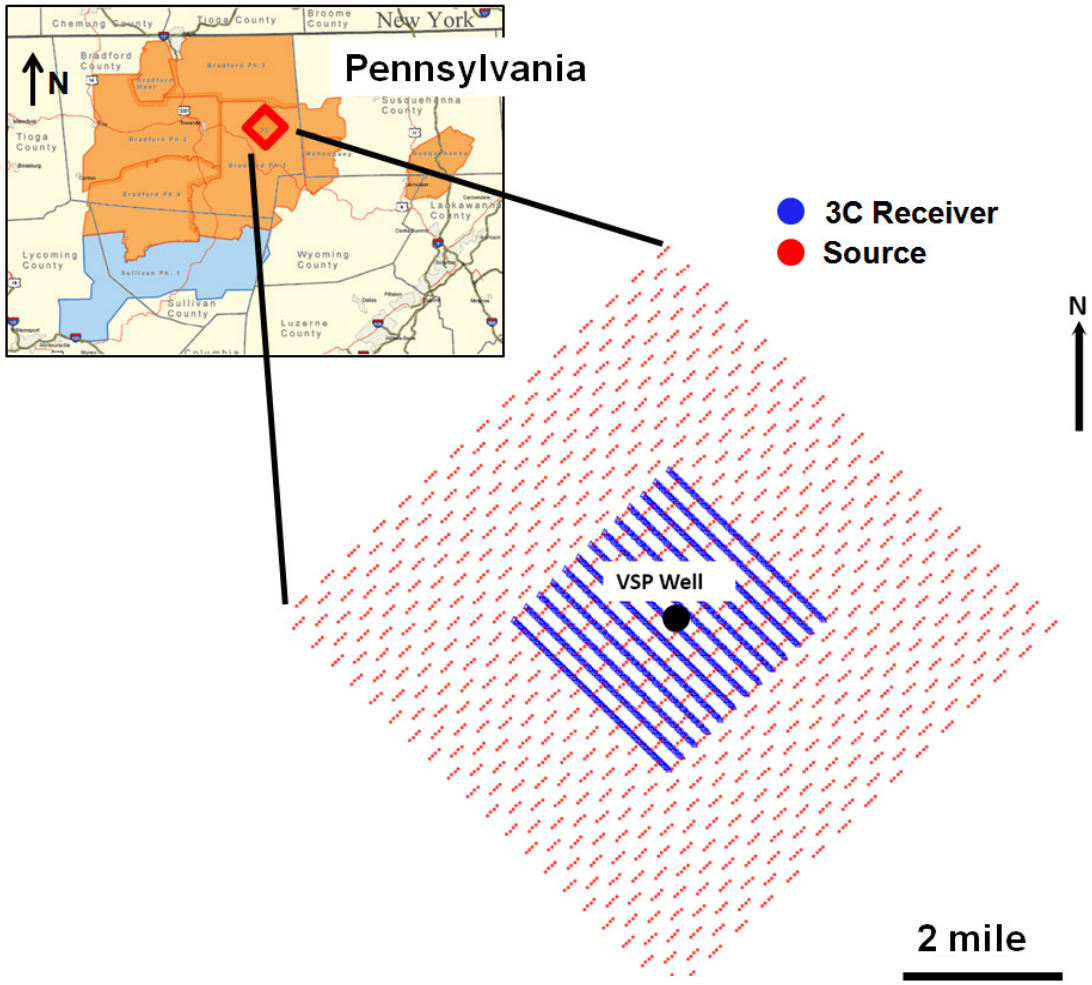

Figure 7.2. The well (solid black circle) used in this study situated at the middle of receiver spread of Bradford 3D-3C seismic survey (modified from Hardage et al., 2011).

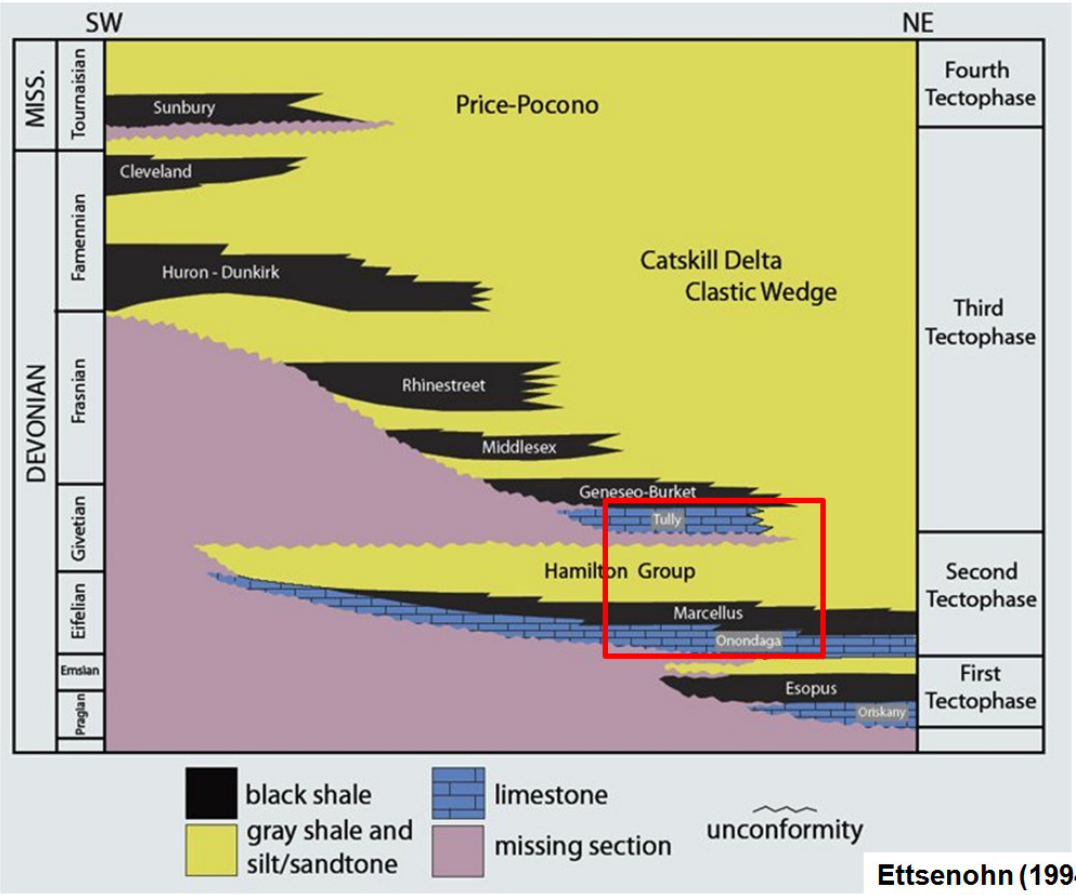

Figure 7.3. The generalized stratigraphy showing key intervals (Tully limestone, Marcellus shale) within red box related to Bradford survey (modified after Ettsenohn, 1994).

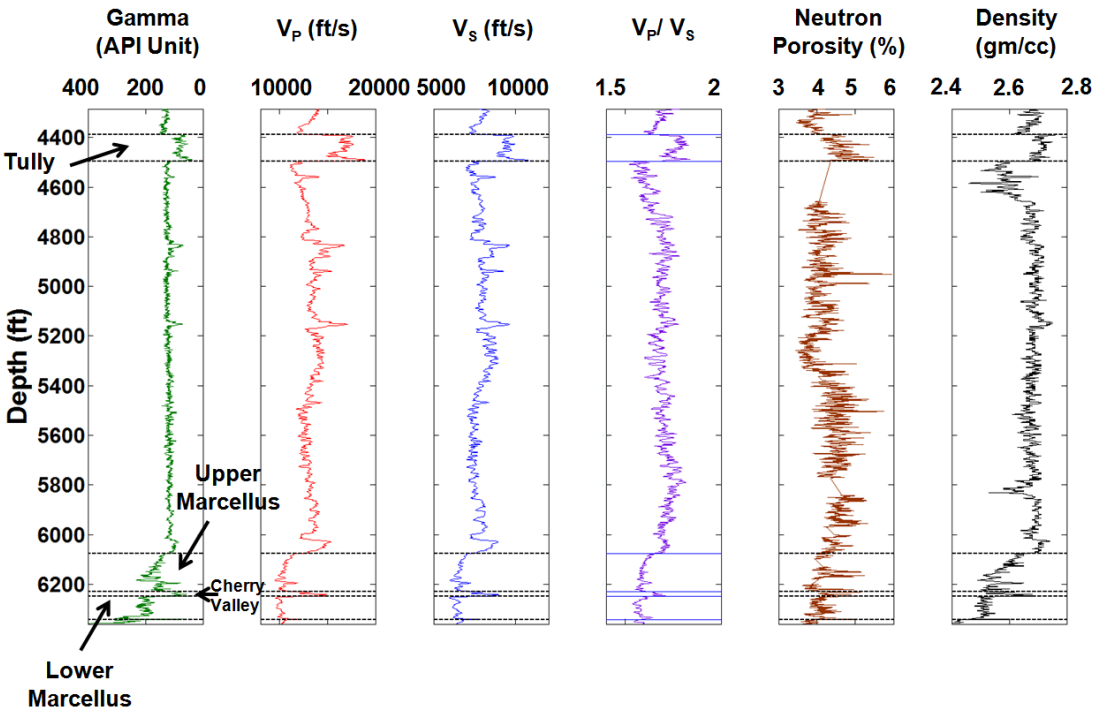

Figure 7.4. The well logs showing gamma ray log, P-wave and S-wave sonic logs, $\frac{V_P}{V_S}$, neutron porosity, and density log from left to right for all intervals.

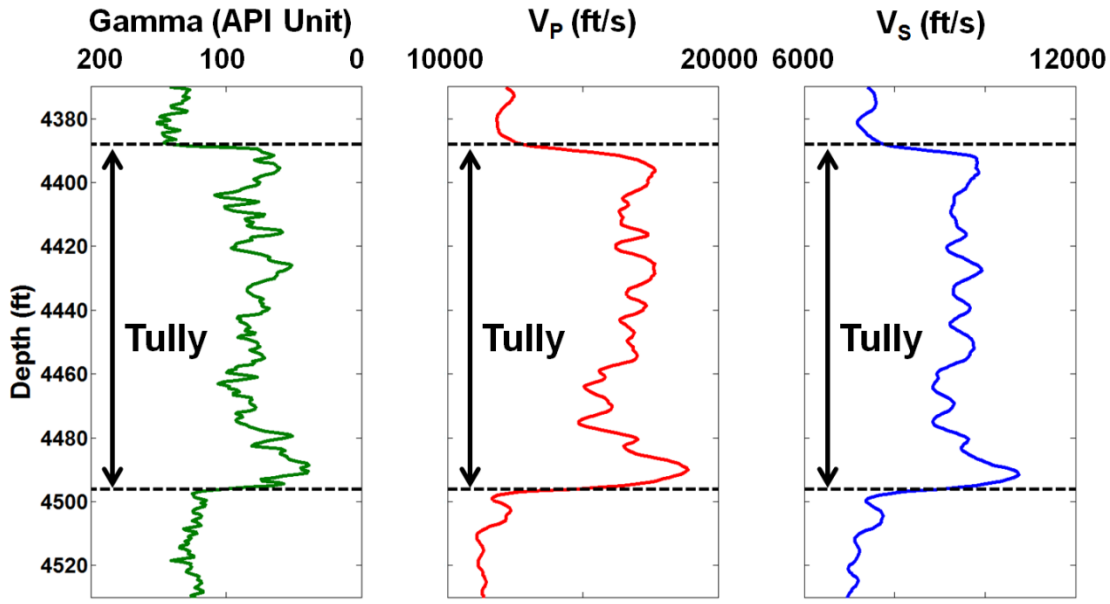

Figure 7.5. The figure shows gamma ray log (solid green line), P-wave sonic log (solid red line), and S-wave sonic log (solid blue line) for the Tully limestone interval.

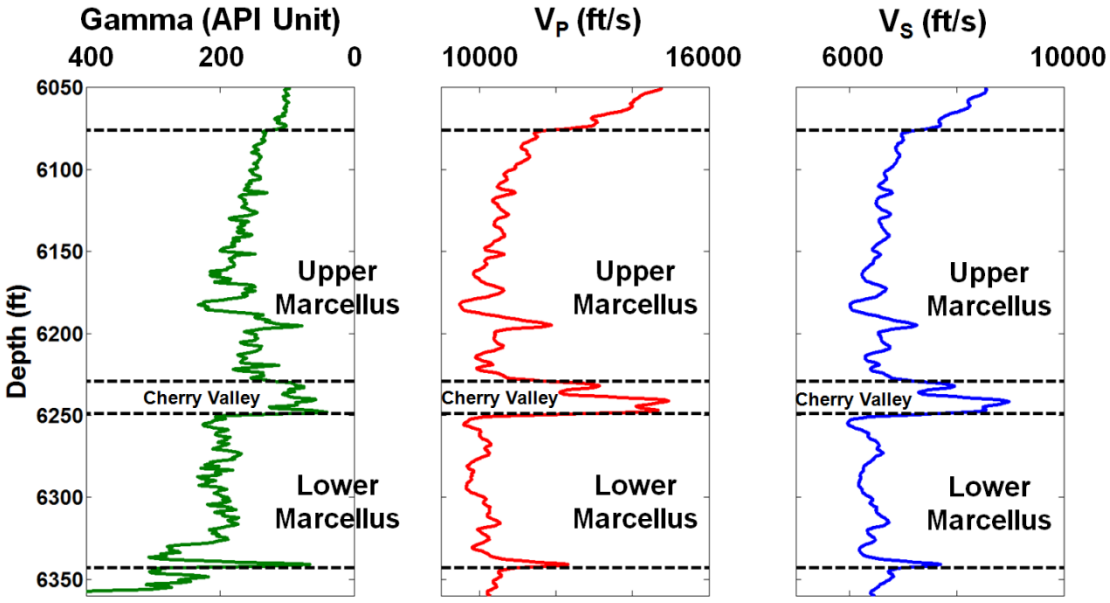

Figure 7.6. The figure shows gamma ray log (solid green line), P-wave sonic log (solid red line), and S-wave sonic log (solid blue line) for the upper and lower Marcellus black shale and Cherry Valley limestone.

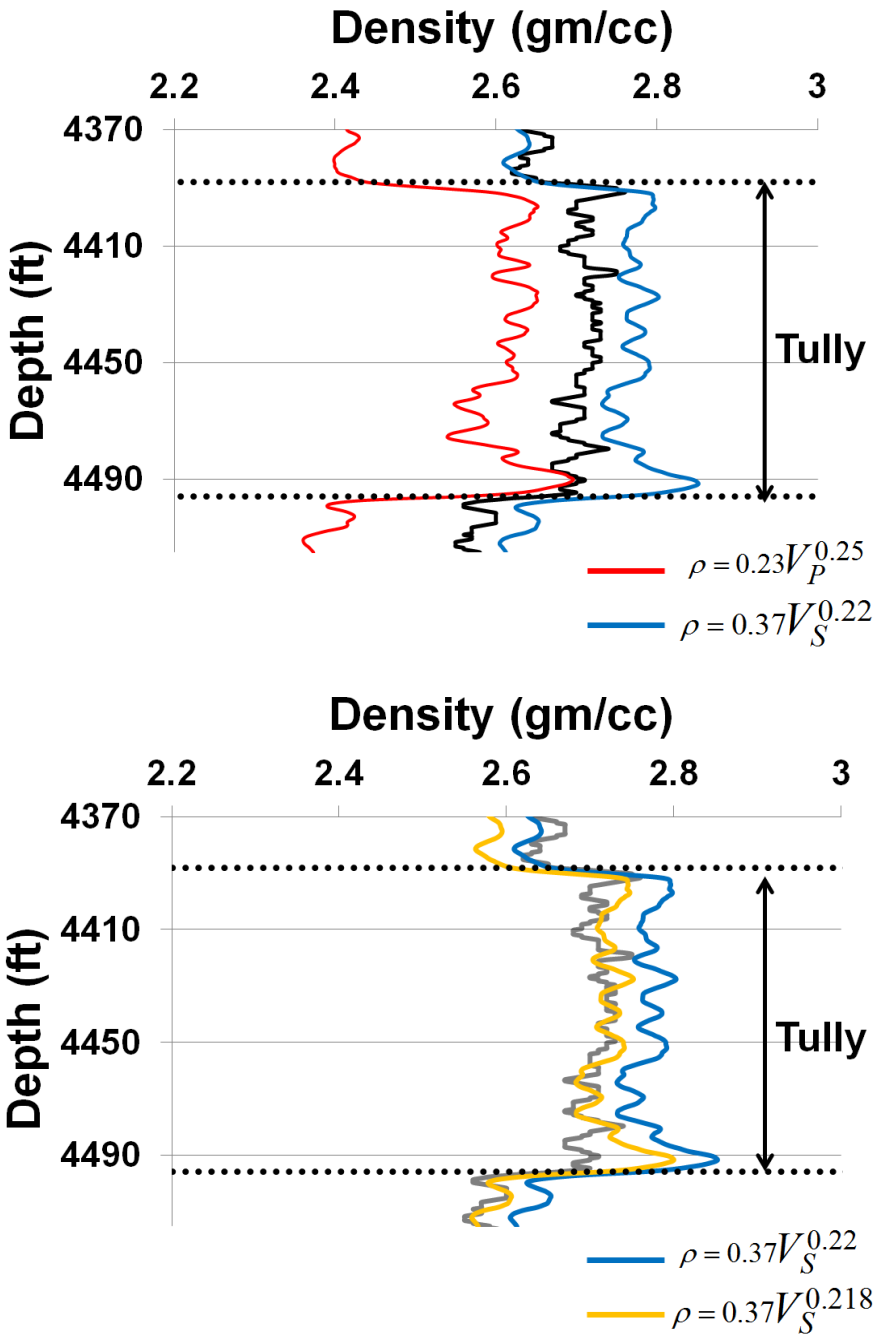

Figure 7.7. The figure shows - a) the original density log (solid black line), the predicted densities from P-wave velocities (solid red line) and S-wave velocities (solid blue line), and b) the predicted densities from S-wave velocities with different exponent values $b = 0.22$ (solid blue line) and $b = 0.218$ (solid yellow line) along with the original density log (solid grey line) for the Tully limestone interval.

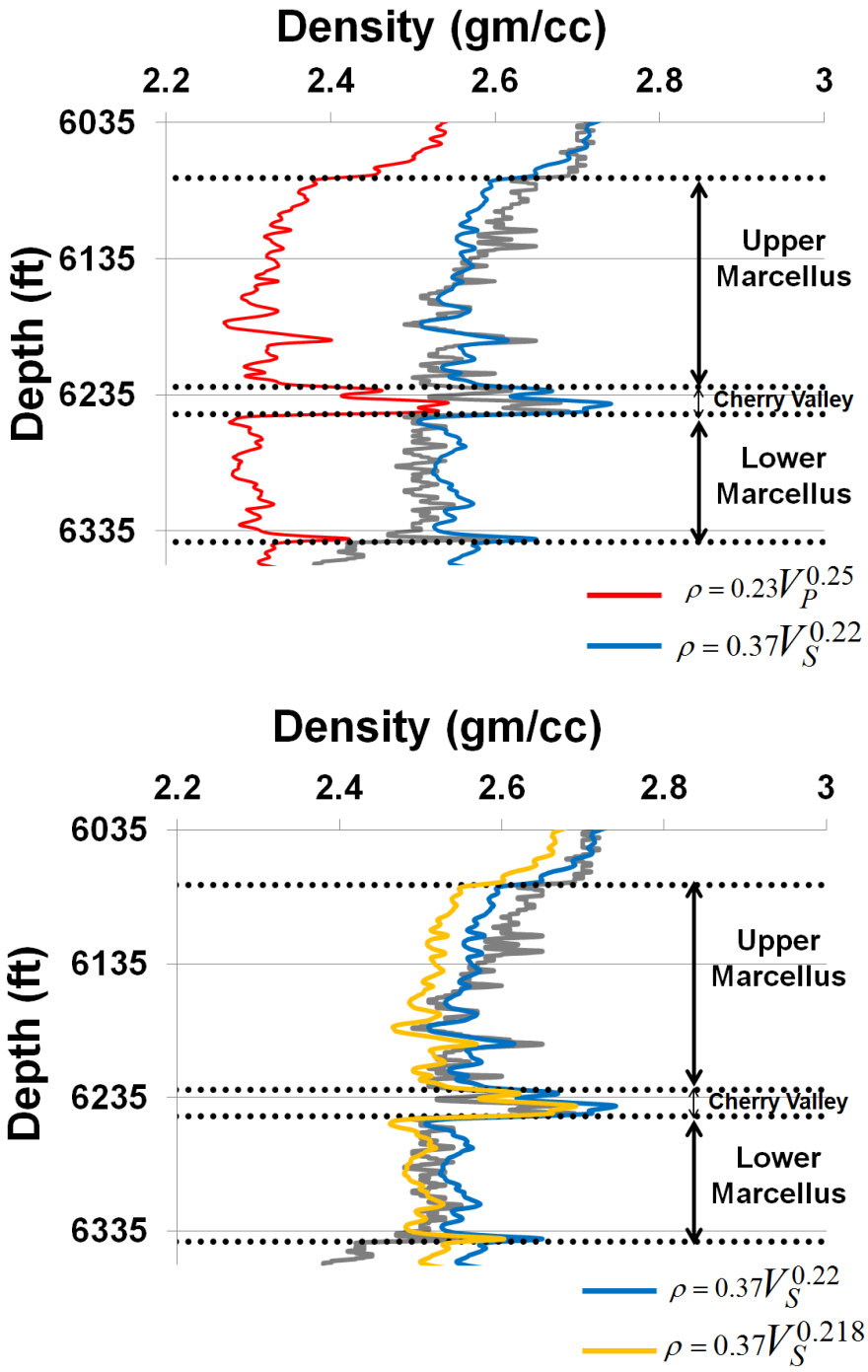

Figure 7.8. The figure shows - a) the original density log (solid grey line), the predicted densities from P-wave velocities (solid red line) and S-wave velocities (solid blue line), and b) the predicted densities from S-wave velocities with different exponent values b = 0.22 (solid blue line) and b = 0.218 (solid yellow line) along with the original density log (solid grey line) for the Marcellus shale interval.

7.3 Density prediction: Physical modeling results

A uniform velocity blank glass model was used as a known sample to test the equation for the density prediction from S-wave velocities. The blank glass model has V_P ~ 5804 m/s (19037 ft/s), V_S ~ 3447 m/s (11306 ft/s) and density ~ 2.6 gm/cc. The modified Gardner's equation for V_S has first been applied to predict the density for the known blank glass model. Using the modified Gardner's relation with a = 0.37 and b = 0.22, we estimated bulk density = 2.8836 gm/cc. The estimate shows an error of 0.2836 gm/cc (10.91 %) compared to the known density of 2.6 gm/cc. But, when the exponent b is changed to 0.209 (5 %), the predicted density provides almost the exact match - 2.6022 gm/cc. On the other hand, the traditional Gardner's relationship (for V_P) predicted the density as 2.7 gm/cc with an error of 0.1 gm/cc (3.85 %). This shows that a small change in exponent (b) value (~0.01 or 5%) for the modified Gardner's relationship for S-wave reduces the error by almost 11 % producing a near perfect match (even better than the traditional one using V_P).

Then, the surface-wave inversion (MASW) method was applied for the seismic dataset acquired over the blank glass model (Figure 7.9) using the ultrasonic measurement systems at AGL, University of Houston. Vertical contact transducers of 1 MHz central frequency were used as source and receivers. The receiver interval is 0.4 mm (i.e. 4 m when scaled by the ultrasonic-seismic factor of 10000) with 26 receivers, source-to-receiver offset of 16 mm (160 m), and shot interval of 0.4 mm (4 m). The traditional MASW analysis first produced the dispersion curve for each shot

gather. The blank glass model consists of only a uniform layer. Hence, the dispersion curve (Figure 7.10) is relatively flat. Then, the 2D S-wave velocity model has been estimated for up to a 90 m deep model (Figure 7.11). The velocities vary from 3400-3500 m/s. Equation 7.3 has been used to predict densities from S-wave velocities with b = 0.21. The predicted densities vary from 2.6-2.625 gm/cc compared to 2.6 gm/cc (Figure 7.12). So, the density prediction from S-wave velocities worked well for the physical modeling data.

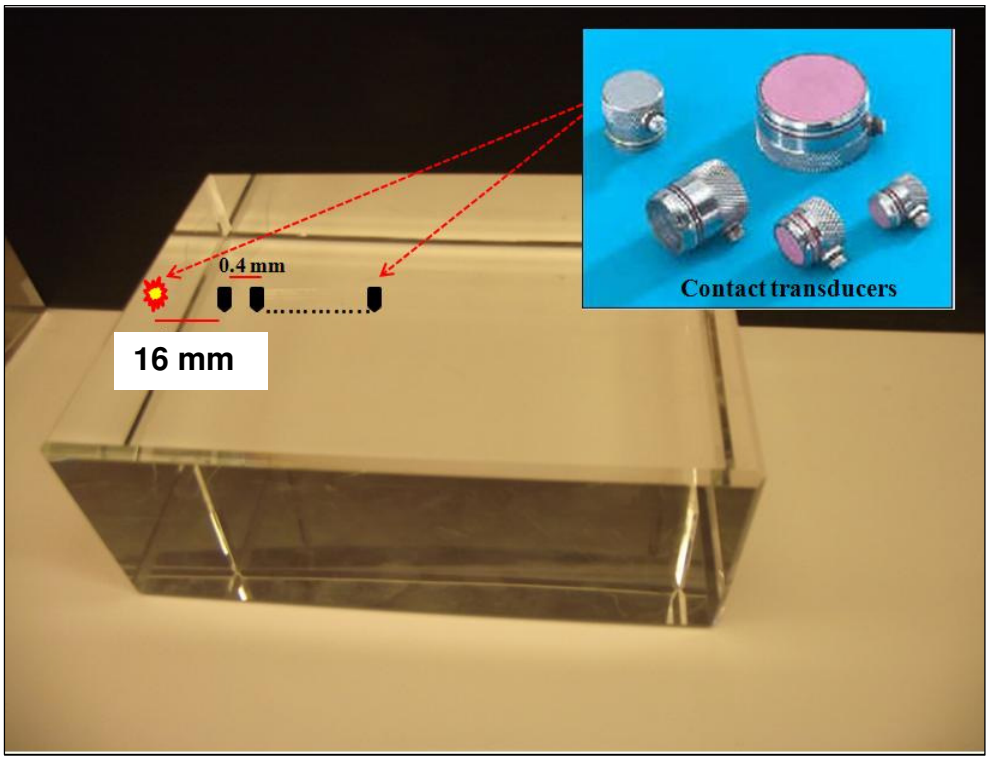

Figure 7.9. The figure shows a blank glass model with the ultrasonic measurement facilities (contact transducers) in inset at AGL, University of Houston. The shot-receiver offset is 160 m (16 mm x10000) and receiver interval is 4 m (0.4 mm x10000). Total 26 receivers were used per shot.

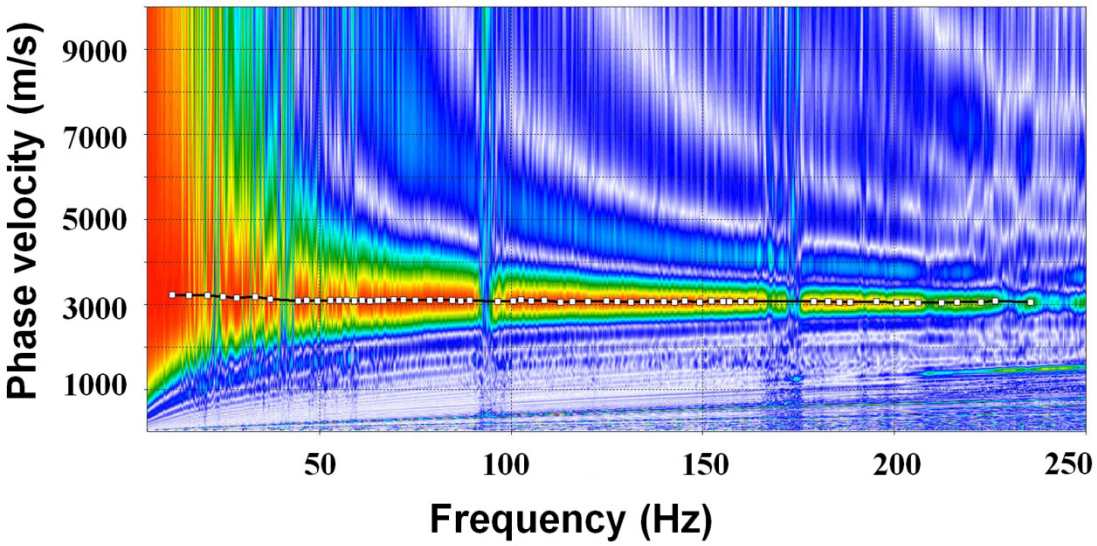

Figure 7.10. A flat dispersion curve for the homogeneous blank glass model.

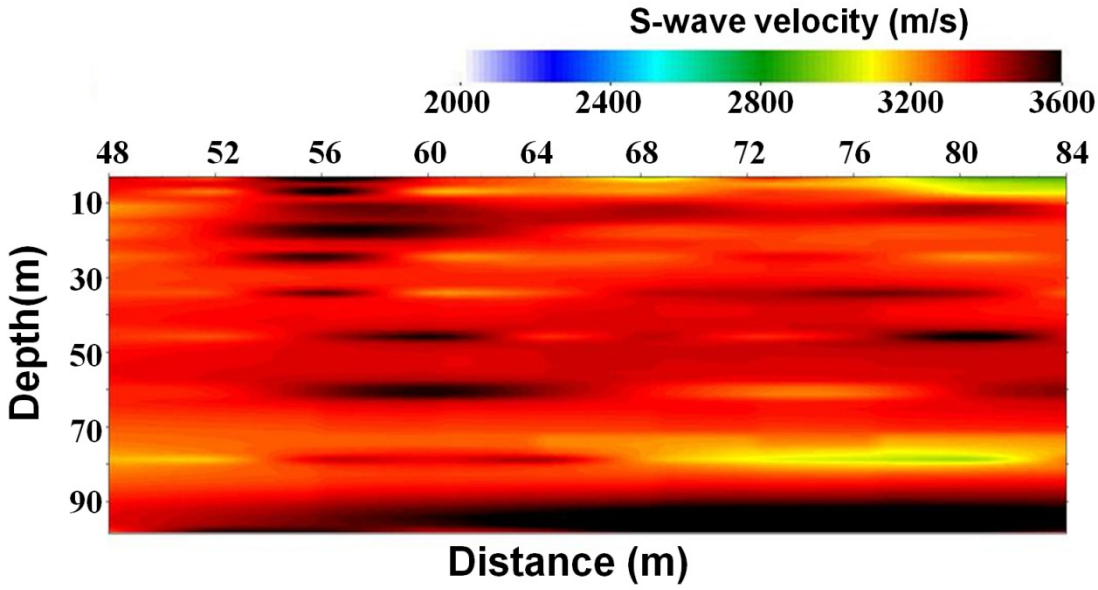

Figure 7.11. 2D S-wave velocity model for the uniform blank model estimated from the surface-wave inversion method (MASW).

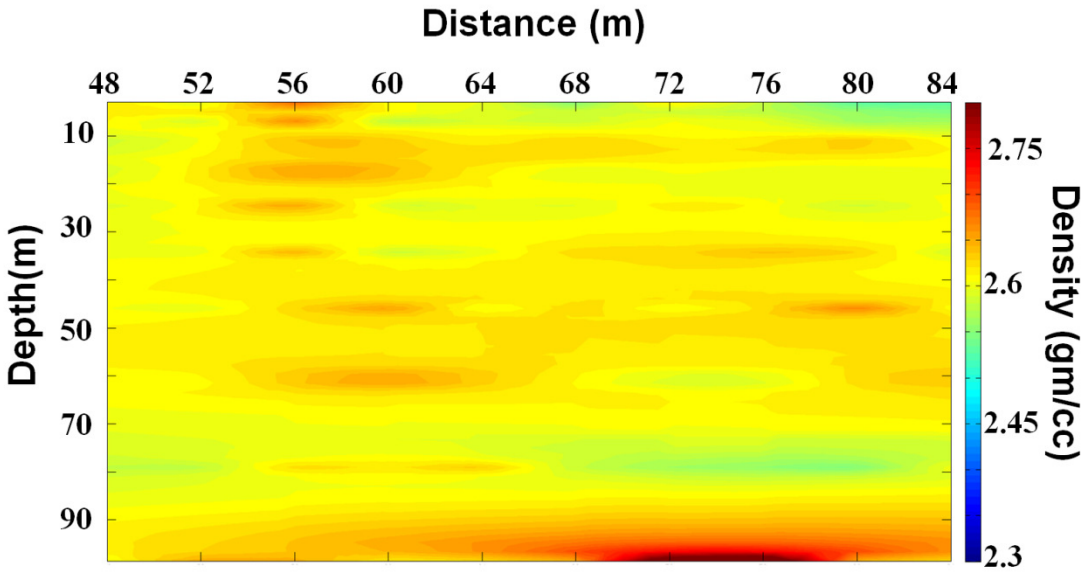

Figure 7.12. 2D S-wave density model for the uniform blank model predicted from S-wave velocities (Figure 7.11) using the Equation 7.3 with exponent b = 0.21.

7.4 Density prediction: Numerical modeling results

Synthetic seismic datasets for a three-layered model (two layers over a half-space) with 45º dipping interface between layer 1 and layer 2 have been generated using a elastic finite-difference numerical modeling code for a layered isotropic medium (Manning, 2007 and Al Dulaijan, 2008). We used the code written by Manning (2007) using the MATLAB programming environment. The physical properties of the model were given as – Layer 1: V_P = 1800 m/s, V_S = 900 m/s, density = 2.00 gm/cc, thickness = 22 m, Layer 2: V_P = 2500 m/s, V_S = 1250 m/s, density = 2.2 gm/cc followed by a half-space (Figure 7.13). We kept the S-wave velocities less than 5000 ft/s (i.e. 1524 m/s) which is often the case for the near-surface. The densities were assigned using the popular Gardner's equation for P-wave velocities. Then, the

traditional MASW method was applied to the dataset to estimate the 2D S-wave velocity structure (Figure 7.14) followed by the prediction of the densities from those estimated S-wave velocities using the exponent value $b = 0.22$. Figure 7.15 shows the predicted 2D density structure which indicates a transition in density values from around 2.00 – 2.25 gm/cc which is very close to the original model – 2.00 gm/cc in layer 1 to 2.2 gm/cc in layer 2. The results show that the density prediction from S-wave velocities (estimated using MASW method) has worked well for the synthetic dataset.

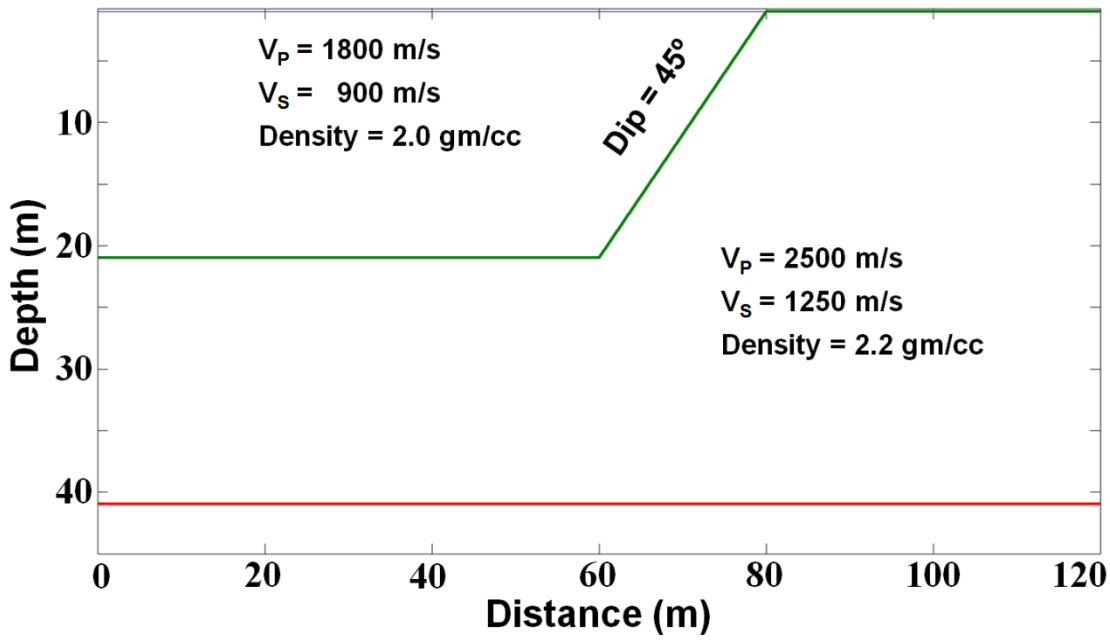

Figure 7.13. A schematic diagram showing the input model for the numerical modeling experiment with a 45° dipping interface.

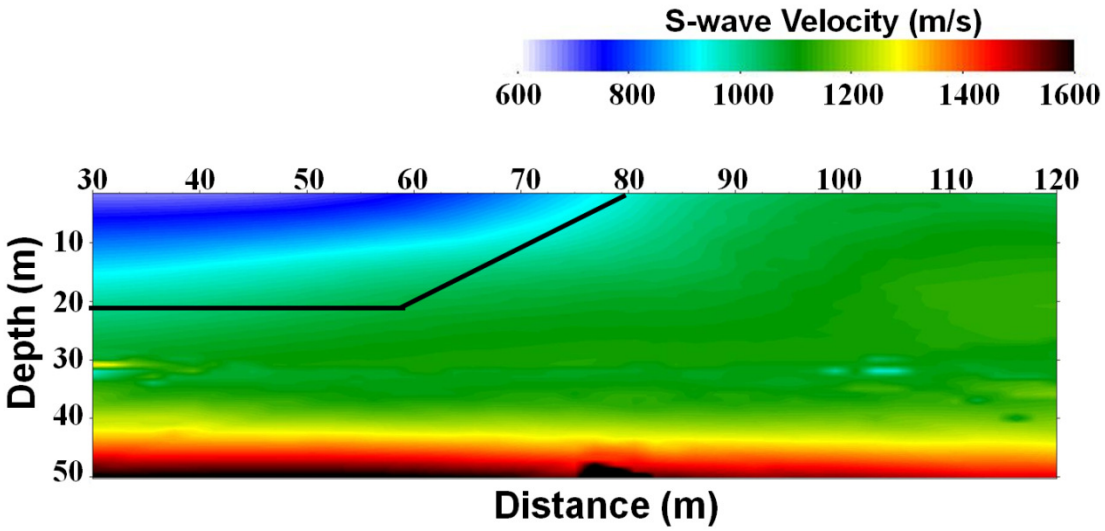

Figure 7.14. The 2D S-wave velocity structure estimated from the surface-wave inversion (MASW) method for the input model in Figure 7.13.

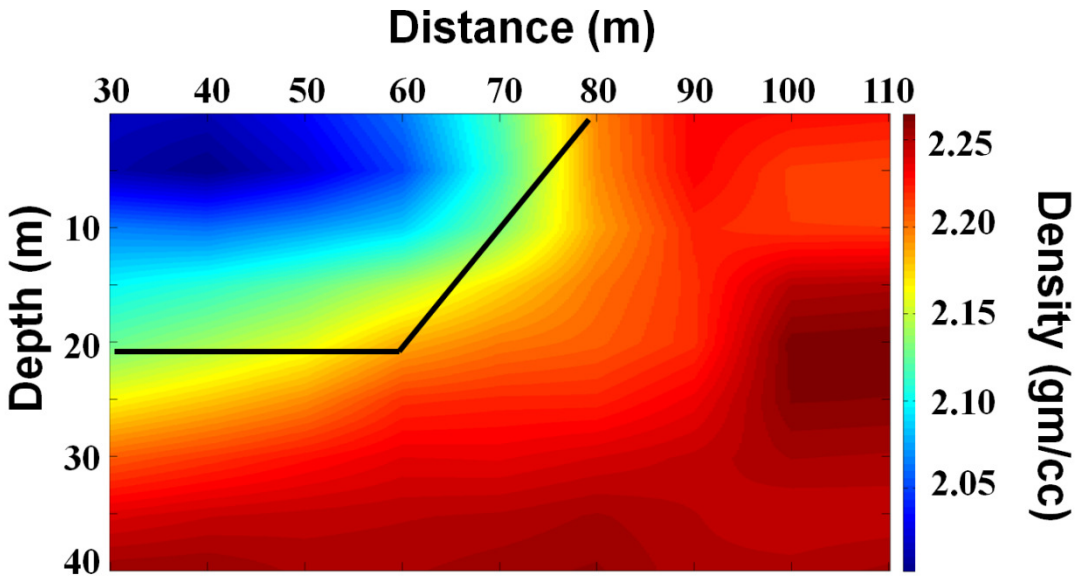

Figure 7.15. The 2D density structure predicted from the S-wave velocities in Figure 7.14.

7.5 Density prediction: YBRA, Montana field camp results

Next, we used a field seismic dataset from the YBRA field camp site in Montana. The site is situated on a highly complex structural set up in the Beartooth Mountain range with overturned beds and a tear fault involving the Mississippian Madison limestone and younger strata (Mukherjee and Stewart, 2013). An east-west-trending 2D seismic line was shot along the tear fault with a truck mounted accelerated weight drop (AWD) as source and vertical planted geophones as receivers. We used both shot and receiver intervals of 3 m while shot location is in between receivers. Two shallow wells (YB1-30 m and YB2-60 m) were also drilled very near to the seismic line (Figure 7.16) at the tear zone and different geophysical loggings (sonic, density, natural gamma, resistivity, full-waveform sonic, acoustic televiewer, and neutron porosity) and VSP surveys were performed.

First, the seismic dataset was used for the surface-wave inversion (MASW) method to estimate S-wave velocities. Then, those S-wave velocities are used to predict the densities. We tried different values of the exponent and b = 0.23 worked better. Figure 7.17 shows the original density log from 60 m deep YB2 well along with the predicted densities for 10-layer 1D structures (all plotted together) from the MASW analysis. The predicted densities are broadly in the range of the original densities with exception at around 35 m depth. The 1D result shows that the predicted densities can not directly match any well-log experiment as the resolution (or frequency) is too

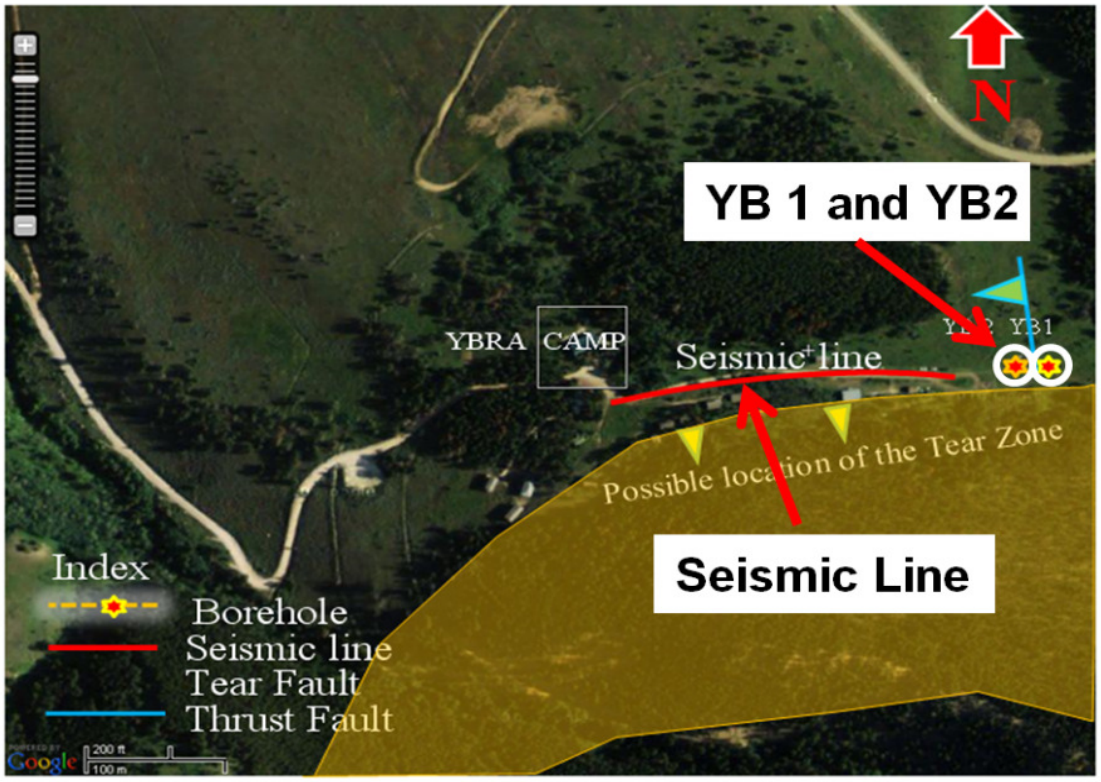

Figure 7.16. Location map of the YBRA field camp (Mukherjee and Stewart, 2013).

high for the well logs. But, predicted densities from S-wave velocities can provide an initial idea of the average densities, especially if there is no density log available which the often the case for the near-surface. Also, P-wave velocities are strongly affected by the water-table in the near-surface; whereas the S-wave velocities will not be affected that strongly. So, for the near-surface, it is conceivable that the density prediction will be better from S-wave velocities. Finally, Figure 7.18 shows the 2D S-wave velocity structure for the seismic line and Figure 7.19 shows the predicted densities (same as 1D densities in Figure 7.17 but now plotted in actual 2D) with the original density log overlaid on it. The densities for the original well log vary mostly

from 1.8-2.4 gm/cc. At around 35 m, the densities go abnormally low of 1.6 gm/cc and less. This is thought to be some problem during the acquisition. Except for this part, Figure 7.19 shows that the predicted densities worked reasonably well. So, it shows that the S-wave velocities for the near-surface (<5000 ft/s or 1524 m/s) estimated from the surface-wave inversion (and/or S-wave refraction analysis) can be used as a tool to predict densities where no (or very few) wells are available.

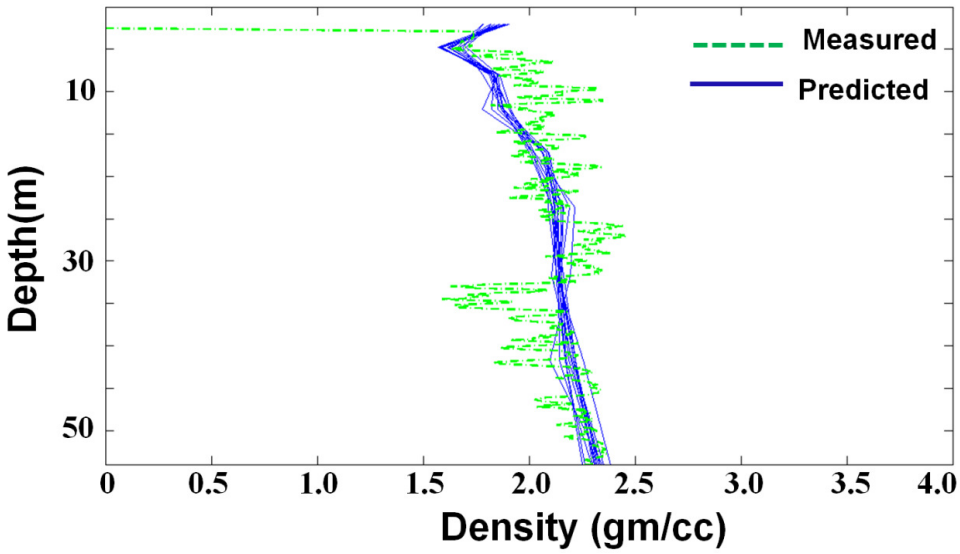

Figure 7.17. The predicted 1D densities (in blue) from the S-wave velocities all plotted together with the original density log (in green).

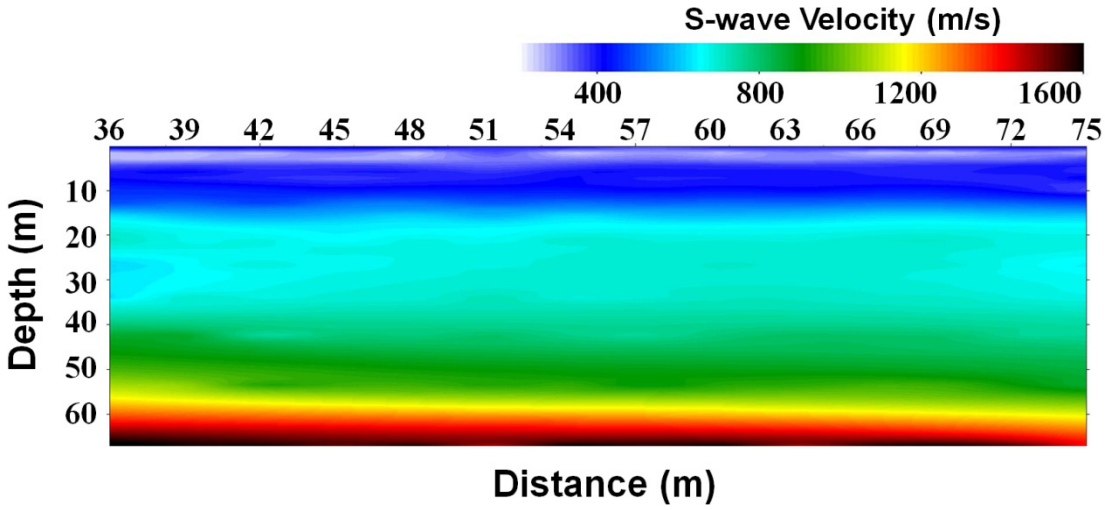

Figure 7.18. 2D S-wave velocity structure estimated from the surface-wave inversion (MASW) method for the seismic line at the YBRA field site (plotted from the ground surface: 0 m).

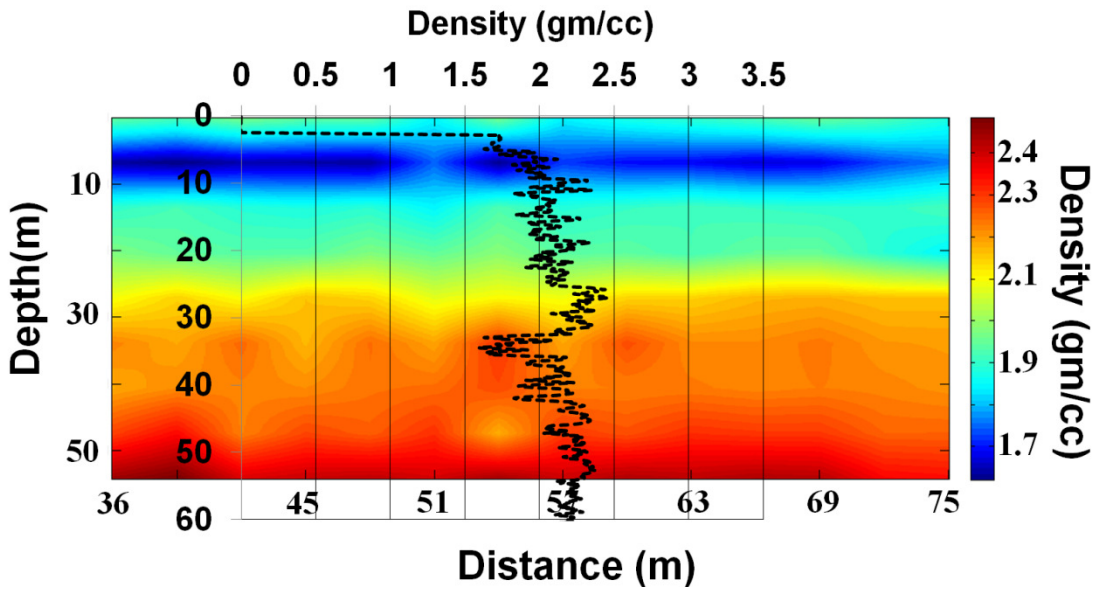

Figure 7.19. 2D density structure predicted from the S-wave velocities in Figure 7.18. The original density log is overlain on the 2D density structure.

7.6 Conclusions

We have assessed a modification to Gardner's relationship to predict density from S-wave velocity. It provides some reasonable results for deep S-wave sonic logs from the Bradford survey. We then used a noninvasive method (MASW) to predict bulk densities from S-wave velocities and compared with known densities. All predicted densities are consistent with known values with a maximum error of 6%. We also changed the exponent values to minimize the error. The exponent *b* varies from 0.209 to 0.23 compared to suggested value of 0.22 with a deviation of 4.5-5 %. The method worked well for low velocities (<5000 ft/s or 1524 m/s) also. Though, experiments with even more data points are required to establish the modified Gardner's relation for regular use.

Chapter 8

Summary

A detailed study has been performed in this thesis to characterize the near-surface. It is important to identify shallow material properties (velocities, densities) and structures. A special emphasis is placed on estimating the near-surface S-wave velocities for this study. The estimated S-wave velocities can be used for exploration seismology as well as geotechnical purposes; and even for planetary studies. A frequency-based surface-wave (Rayleigh-wave or ground-roll) inversion method (MASW: Multichannel Analysis of Surface Waves) has been used to estimate 1D and 2D S-wave velocities. MASW method has been applied on varied seismic datasets related to numerical simulation, physical modeling, and field surveys. We have used field seismic datasets from different geological settings and geographical locations: 1) La Marque, Texas, 2) Barringer (Meteor) Crater, Arizona, 3) YBRA field camp, Montana, 4) Hockley fault survey, Texas, and 5) Bradford, Pennsylvania.

The estimated S-wave velocity results encountered in this thesis vary from as low as 100 m/s for La Marque survey to as large as 3400-3500 m/s for a physical modeling experiment (blank glass block). A detailed case study related to the Barringer (Meteor) Crater has been performed. We found P-wave velocities (from travel-time

tomography) varying from 450 m/s to 2500 m/s for a 55 m deep earth model and S-wave velocities of 200-1000 m/s for 38 m deep earth model. A trend has been identified such as the low-velocity layers thin away from the crater which is interpreted as the expected thinning of the ejecta blanket. Drill-hole results show that the ejecta thickness is 15-20 m near the rim and decreases to 5m and less away from the rim. The velocity results correlate well with the thinning structure. Thus, the ejecta blanket structure has been determined based on P- and S-wave 2D velocity structures and calibrating them with drill-hole results. The P-wave velocities vary from 2700-6100 m/s and S-wave velocities vary from 1700-3300 m/s for the ultrasonic measurements. After incorporation of a straightforward porosity effect (10% air-filled porosity), the ultrasonic velocities are comparable to the seismic estimates. These results show that MASW method successfully estimates the near-surface S-wave velocities and identifies shallow structures.

Next, the effect of lateral heterogeneities on MASW analysis has been evaluated using numerical simulation, physical modeling experiment (vertically merged blocks of plexiglas and aluminum), and the Hockley fault survey, Texas. The resultant S-wave velocity structure for a gentle lateral heterogeneity case (numerical modeling) shows a smooth change in velocities from 250-300 m/s to 450-500 m/s for the actual change of 300 m/s to 500 m/s for the first two layers. A mild smearing of velocities is observed along the dipping surface. Still, the boundary is imaged properly along the dipping surface. We have found S-wave velocities of 1400 m/s for plexiglas (actual

value 1380 m/s) and 3000-3100 m/s for aluminum (actual value 3100 m/s) in the final S-wave velocity structure after full MASW analysis. But, the velocities are mixed across the vertical boundary between two blocks. Similarly, S-wave velocity structure (varying from 200-325 m/s for 10 m deep model) shows noisy, mixed velocity values near the main fault area for Hockley fault survey. So, it is observed that the MASW method can identify the zones of lateral variations spatially but resultant S-wave velocities around those zones are smeared.

The feasibility of using S-wave velocities from MASW as the starting model for a simple FWI method has been evaluated. Another aim is to provide a better solution when the MASW method is affected by lateral heterogeneity. The FWI method has been tested for laterally homogeneous as well as heterogeneous cases. The starting S-wave velocities from MASW are close to the actual values but still have errors of 2.8 % (for laterally homogeneous) to 7.25 % (for laterally heterogeneous). We have achieved a good match after 6-10 iterations for each model. The FWI method has worked well for the laterally heterogeneous case as well which was the main goal of this study. We have followed a multi-stage strategy where data input was low-frequency and near-offset for earlier iterations with gradual incorporation of far offsets and higher frequency.

The application of the estimated S-wave velocities for various purposes (S-wave statics calculation, density prediction) has been evaluated. The seismic datasets from

the Bradford 3D-3C survey have been analyzed to estimate the S-wave statics. The S-wave velocities for a 2D line vary from 5200-7200 ft/s (1585-2194.56 m/s) for a 530 ft (161.5 m) deep model. The S-wave LVL statics is calculated which is in the range of 25-42 ms. This result is then compared with the S-wave statics provided by GeoKinetics. The results correlate well showing that the statics obtained in this study (from MASW method) is a smooth long-wavelength type of statics. The S-wave statics calculation discussed in this chapter is a stand-alone process and is not dependent on any PP imaging or results.

We have finally assessed a modification to Gardner's relationship to predict density from S-wave velocity. It provides some reasonable results for deep S-wave sonic logs from the Bradford survey. We then used a noninvasive method (MASW) to predict bulk densities from S-wave velocities and compared with known densities. All predicted densities are consistent with known values with a maximum error of 6%. The exponent value varies from 0.209 to 0.23 compared to suggested value of 0.22 with a deviation of 4.5-5 %. The method worked well for low velocities (<5000 ft/s or 1524 m/s) also.

Appendix A

A short discussion on MASW methodology

A.1 Step 1 – generation of dispersion curves

As discussed earlier, the MASW method is a two-step procedure. Step 1 is to generate the dispersion curves (frequency vs. phase velocity plots) and step 2 is to perform the inversion of dispersion curves to estimate S-wave velocities. The generation of the dispersion curves in the MASW method is a wavefield transformation method (Park et al., 1998). MASW generates dispersion curves directly from the raw shot gathers. The raw shot gathers can be represented as – $u(x,t)$ i.e. a function of offset (x) and time (t). In MASW method, the offset-time domain data is first transformed to offset (x)-frequency (ω) domain through 1D Fourier transform. So, the data can now be expressed as a combination of amplitude and phase spectra –

$$U(x,\omega) = A(x,\omega)P(x,\omega) \quad \text{(A.1)}$$

where, $A(x,\omega)$ indicates amplitude spectrum and $P(x,\omega)$ indicates phase spectrum. The amplitude spectrum contains the information related to attenuation, spherical divergence etc. whereas phase spectrum contains the information about dispersion (Park et al., 1998). Here, the term dispersion indicates the change of Rayleigh-wave phase velocities with frequencies. The Rayleigh-wave phase velocity can be expressed as - $V_R = \frac{\omega}{k}$, where V_R is Rayleigh wave phase velocity, ω is angular

frequency, and k is the angular wavenumber. Now, the equation A.1 can further be written as:

$$U(x,\omega) = e^{-iKx}A(x,\omega) \quad \text{(A.2)}$$

where, $P(x,\omega) = e^{-iKx}$ and $K = \frac{\omega}{V_R}$. The MASW method is a frequency based phase-shift method. A phase-shift is applied on the data for each frequency which can be written as - e^{ikx} or $e^{i\frac{\omega}{V_R}x}$. Now, an integration is applied on $U(x,\omega)$, which sums the entire wavefield for an offset range for each frequency and for a series of phase velocities. This integral can be written as:

$$\int_{x1}^{x2} e^{ikx}U(x,\omega)dx = \int_{x1}^{x2} e^{ikx}e^{-iKx}A(x,\omega)dx = \int_{x1}^{x2} e^{-i(K-k)x}\left[\frac{A(x,\omega)}{|A(x,\omega)|}\right]dx \quad \text{(A.3)}$$

The integral result is nearly zero for most the cases except when the total phase itself is zero (Liner, 2012) i.e. when (K-k) x = 0 or $K = k = \frac{\omega}{V_R}$. So, when the integration is performed over the offset range for a particular frequency, we scan through a series of phase velocity values. There will be a particular phase velocity at that frequency which would yield the total phase as zero and consequently a large value of the integral (or peaks). Other velocities would yield a very small or zero value for the integral. The integration is repeated in the similar fashion for different frequencies. In this way, a phase velocity-frequency image matrix will be produced containing dispersion curves. The dispersion curves can be multi-modal i.e. for a particular frequency there may be more than one phase velocities which produce zero phase values or large integral values (or peaks). So, the phase velocity-frequency image

may contain a single dispersion curve (fundamental mode) or multiple curves (fundamental and higher modes). The higher modes have greater velocities than the fundamental mode at a particular frequency; hence, they have longer wavelengths and can penetrate deeper.

A.2 Step 2 – inversion of dispersion curves

Once a good quality dispersion curve is generated, an inversion scheme is applied to estimate the S-wave velocities from Rayleigh-wave (or ground-roll) phase velocities. For a homogeneous medium, it is commonly assumed that S-wave velocity (V_S) is related to the Rayleigh-wave velocity (V_R) through the linear relationship of - $V_R = 0.9194V_S$ for the Poisson's ratio of 0.25 (Sheriff and Geldart, 1982). For the inversion scheme, an analysis of the sensitivity matrix or Jacobian matrix shows that the Rayleigh-wave phase velocities or dispersion curves are mostly sensitive to S-wave velocities (Xia et al., 1999). So, the contributions from the P-wave velocity, density, and layer thickness have been ignored during the inversion scheme for the MASW method. In other words, only S-wave velocities regulate any change in Rayleigh-wave phase velocities.

First, an initial S-wave velocity model is derived based on the observed dispersion curve information. Then, a dispersion curve (model response) is estimated through

forward modeling from the initial S-wave velocity model. Let us assume that the observed data or dispersion curve is represented by - $b_{m\times1}^{obs}$ where m is the number of frequencies and the estimated dispersion curve is represented by - $b_{m\times1}^{est0}$. So, the difference between observed and estimated dispersion curve can be shown as - $\Delta b_{m\times1}$ i.e. a column vector of size $m\times1$. Now, let us assume that the S-wave velocity earth model consists of n-layers. So, a linearized matrix equation can be written as:

$$\Delta b = J\Delta x \tag{A.4}$$

where, J is the Jacobian matrix of $m\times n$ size, and Δx is the S-wave velocity update column vector for n layers i.e. the size of $n\times1$. The elements of the Jacobian matrix evaluates the sensitivity i.e. how a small change in S-wave velocity will affect the Rayleigh-wave phase velocity. Equation A.4 is solved in a least-square fashion using Levenberg-Marquardt and singular-value decomposition techniques. Once, the S-wave velocity updates are calculated, the process is repeated again (i.e. iteratively) unless the difference between observed and estimated dispersion curves are minimized. Figure A.1 shows a visual representation of the inversion scheme. More detailed information can be found in Xia et al., 1999.

The MASW method is always applied on individual raw shot gathers. So, one dispersion curve is generated from one shot gather. That single dispersion curve is inverted to estimate a 1D S-wave velocity structure. The 1D velocity structure for a shot gather is placed at the middle of the receiver spread related to that shot. So, the 1D S-wave velocity structure represents the averaged velocity of the active receiver

spread for one shot. Then, same analysis is performed for consecutive shot gathers. So, multiple 1D S-wave velocity structures are estimated and merged (using interpolation technique) to generate a 2D S-wave velocity structure (Figure A.2).

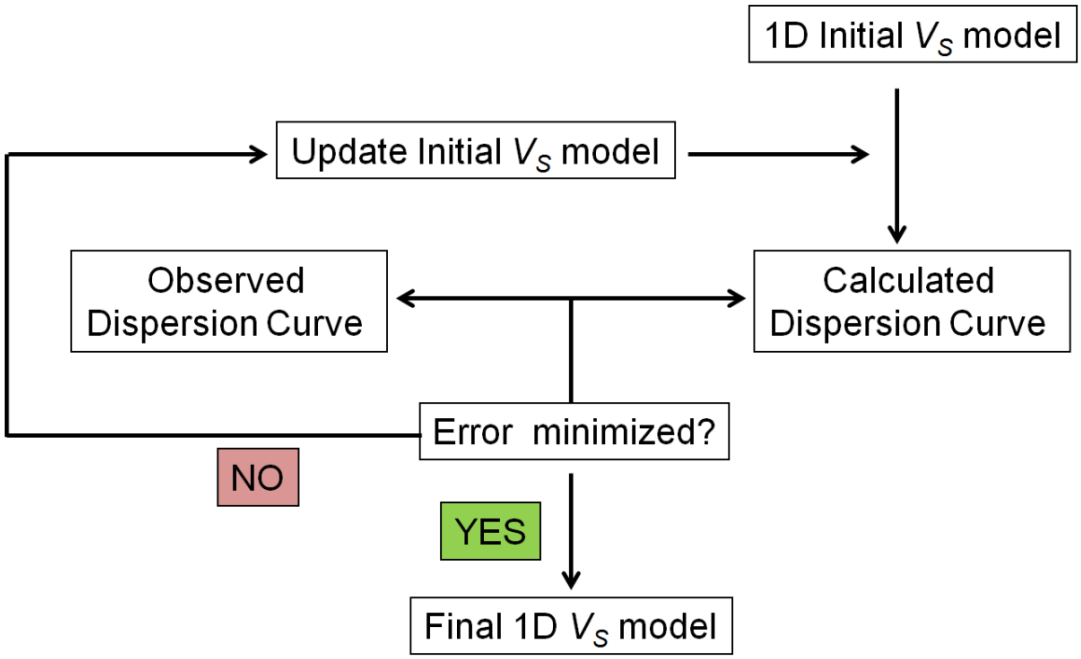

Figure A.1. The flow chart summarizes the iterative inversion (of dispersion curve) procedure used in the MASW method.

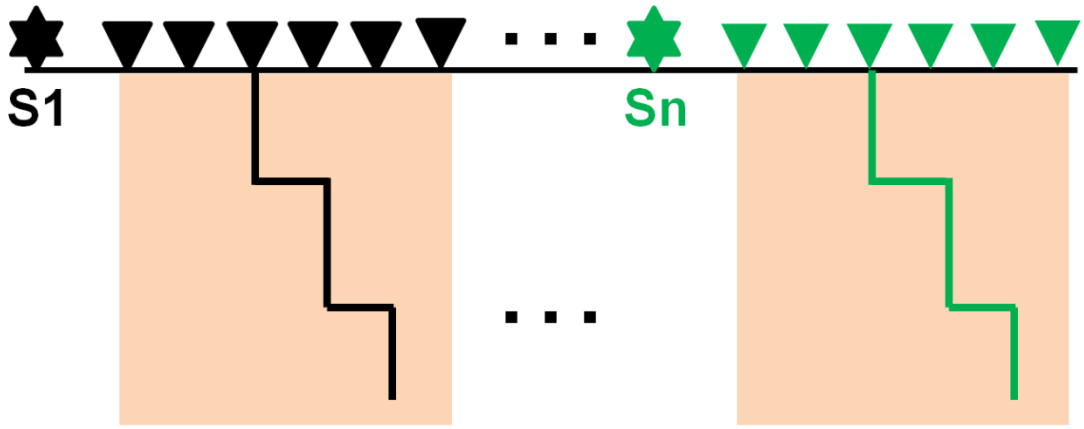

Figure A.2. The schematic diagram shows that in the MASW method the 1D S-wave velocity structure from a shot gather (S1) is placed at the middle of the receiver spread related to that shot. Multiple 1D S-wave velocity structures for consecutive shots (*n* number of shots: Sn) are then merged to generate the 2D S-wave velocity structure.

References

Anderson, D. L., 1984, Surface wave tomography, Eos, **65**, no. 16, 147-148.

Al Dulaijan, K., 2008, Near-surface characterization using seismic refraction and surface-wave methods: M. S. thesis, University of Calgary.

Bansal, R., W. Ross, S. Lee, M. Matheney, A. Martinez, T. Jenkinson, and A. Shatilo, 2009, A novel approach to estimating near-surface S-wave velocity and converted-wave receiver statics: 79th Annual International Meeting, SEG, Expanded Abstracts, 1192–1196.

Boiero, D., and L. V. Socco, 2010, retrieving lateral variations from surface wave dispersion curves: Geophysical Prospecting, **58**, 977-996.

Boiero, D., P. Bergamo, R. B. Rege, and L. V. Socco, 2011, Estimating surface-wave dispersion curves from 3D seismic acquisition schemes: Part 1 – 1D models: Geophysics, **76**, no. 6, G85-G93.

Capuano, R. M., and R. Z. Jan, 1996, In-situ hydraulic conductivity of clay and silty-clay fluvial-deltaic sediments: Ground Water, **34**, 545–551.

Cary, P. W., and D. W. S. Eaton, 1993, A simple method for resolving large converted-wave (P-SV) statics: Geophysics, **58**, 429-433.

Cox. M., 1999, Static Corrections for Seismic Reflection Surveys: Society of Exploration Geophysicists.

Dey, A. K., and R. R. Stewart, 1997, Predicting density using Vs and Gardner's relationship: CREWES Research Report, Ch. 9.

Engelkemeir, R., and S. Khan, 2007, Near-surface geophysical studies of Houston faults: The Leading Edge, **26**, No. 8, 1004-1008.

Ettensohn, F. R., 1994, Tectonic control on the formation and cyclicity of major Appalachian unconformities and associated stratigraphic sequences, *in* J. M. Dennison, F. R. Ettensohn, eds., Tectonic and eustatic controls on sedimentary cycles: SEPM Concepts in Sedimentology and Paleontology 4, 217–242.

Gardner, G. H. F., L. W. Gardner, and A. R. Gregory, 1974, Formation velocity and

density – the diagnostic basics for stratigraphic traps: Geophysics, **39**, 770-780.

Gaiser, J., A. Chaveste, M. Edrich, T. Rebec, and R. Verm, 2011, Seismic anisotropy of the Marcellus shale: Feasibility study for fracture characterization: Presented at the CSEG CSPR CWLS Convention.

Hardage, B., M. deAngelo, and D. Sava, 2011, Marcellus shale geophysics: Presented at the RPSEA Meeting.

Ivanov, J., R. D. Miller, and G. Tsoflias, 2008, Some practical aspects of MASW analysis and processing: 21st EEGS Symposium on the Application of Geophysics to Engineering and Environmental Problems, 1186-1198.

Khan, S. D., R. R. Stewart, M. Otoum, and L. Chang, 2013, A geophysical investigation of the active Hockley Fault System near Houston, Texas: Geophysics, **78**, no. 4, B177-B185.

Koesoemadinata, A., G. El-Kaseeh, N. Banik, J. Dai, M. Egan, A. Gonzalez, and K. Tamulonis, 2011, Seismic reservoir characterization in Marcellus shale: 81st Annual International Meeting, SEG, Expanded Abstracts, 3700-3704.

Kring, D. A., 2007, Guidebook to the geology of Barringer meteorite crater, Arizona (a.k.a. Meteor crater): 70th Annual Meeting of the Meteoritical Society, Lunar and Planetary Institute contribution 1355.

Li, A., and R. S. Detrick, 2003, Azimuthal anisotropy and phase velocity beneath Iceland: implication for plume-ridge interaction: Earth and Planetary Science Letters, **214,** 153-165.

Li, A., and R. S. Detrick, 2006, Seismic structure of Iceland from Rayleigh wave inversions and geodynamic implications: Earth and Planetary Science Letters, **241,** 901-912.

Lin, C. C., C. C. Chang, and T. S. Chang, 2004, The use of MASW method in the assessment of soil liquefaction potential: Soil Dynamics and Earthquake Engineering, **24**, 689-698.

Liner, C., 2012, Elements of seismic dispersion: A somewhat practical guide to frequency-dependent phenomena: Distinguished Instructor Series, No. 15, SEG.

Luo, Y., J. Xia, J. Liu, Y. Xu, and Q. Liu, 2009, Research on the middle-of-receiver-

spread assumption of the MASW method: Soil Dynamics and Earthquake Engineering, **29**, 71-79.

Luo, Y., J. Xia, Y. Xu, C. Zeng, R. D. Miller, and Q. Liu, 2009, Dipping-interface mapping using mode-separated Rayleigh waves: Pure and Applied Geophysics, **166**, 353-374.

Mallick, S., and L. N. Frazer, 1987, Practical aspects of reflectivity modeling: Geophysics, **52**, 1355-1364.

Manning, P. M., 2007, Techniques to enhance the accuracy and efficiency of finite-difference modelling for the propagation of elastic waves: Ph. D. thesis, The University of Calgary.

Mazur, M. J., R. R. Stewart, and A. R. Hildebrand, 2000, The seismic signature of meteorite impact craters: CSEG Recorder, **25**, 10-16.

Melosh, H. J., 1989, Impact Cratering: A Geologic Process: Oxford University Press.

Menke, W., 2012, Geophysical data analysis: Discrete inverse theory: Academic Press.

Miller, S. L. M., and R. R. Stewart, 1990, Effects of lithology, porosity and shaliness on P- and S-wave velocities from sonic logs: Canadian Journal of Exploration Geophysics, **26**, 94–103.

Mukherjee, T., and R. R. Stewart, 2013, Geophysical study of a structurally complex near-Surface, Beartooth Mountains, Montana: Rocky Mountain Geology (submitted 2013).

Nazarian, S., K. H. Stokoe II, and W. R. Hudson, 1983, Use of spectral analysis of surface waves method for determination of moduli and thicknesses of pavement systems: Transport. Res. Record No. **930**, 38–45.

Otoum, M. A., 2011, An integrated geophysical investigation to map the Hockley active fault in northwest Harris county: M. S. thesis, University of Houston.

Park, C. B., R. D. Miller, and J. Xia, 1998, Imaging dispersion curves of surface waves: 68th Annual International Meeting, SEG, Expanded Abstracts, 1377–1380.

Park, C. B., R. D. Miller, and J. Xia, 1999, Multichannel analysis of surface waves: Geophysics, **64**, 800–808, doi:10.1190/1.1444590.

Park, C. B., R. D. Miller, and J. Xia, 2001, Offset and resolution of dispersion curve in multichannel analysis of surface waves (MASW): Proceedings of the Symposium on the Application of Geophysics to Engineering and Environmental Problems, SSM4-SSM4.

Park, C. B., and N. Ryden, 2007, Offset selective dispersion imaging: Proceedings of the Symposium on the Application of Geophysics to Engineering and Environmental Problems, 910-915.

Park., C. B., 2011, Imaging Dispersion of MASW Data – Full vs. Selective Offset Scheme: Journal of Environmental and Engineering Geophysics, **16** (1), 13-23.

Potter, C. C., and R. R. Stewart, 1998, Density predictions using V_P and V_S sonic logs: Consortium for Research in Elastic Wave Exploration Seismology, Research Report, Ch. 10.

Pratt, R. G., C. Shin, and G. J. Hicks, 1998, Gauss-Newton and full Newton methods in frequency-space seismic waveform inversion: Geophysical Journal International, **133**, 341-362.

Roddy, D. J., J. M. Boyce, G. W. Colton, and A. L. Dial, Jr., 1975, Meteor crater, Arizona, rim drilling and thickness, structural uplift, diameter, depth, volume, and mass-balance calculations: Proceedings of the 6th Lunar Science Conference, 2621–2644.

Roy, S., and R. R. Stewart, 2012, Near-surface seismic investigation of Barringer (Meteor) Crater, Arizona: Journal of Environmental and Engineering Geophysics, **17**, 117-127.

Roy, S., R. R. Stewart and K. Al Dulaijan, 2010, S-wave velocity and statics from ground-roll inversion, The Leading Edge, **29**, 1250–1257.

Roy, S., R. R. Stewart, and A. Turolski, 2012, Near-surface geophysical imaging of Barringer (Meteor) Crater, Arizona: 82nd Annual International Meeting, SEG, Expanded Abstracts, 1-5.

Ryden, N., C. B. Park, P. Ulriksen, and R. D. Miller, 2004, Multimodal approach to seismic pavement testing: Journal of Geotechnical and Geoenvironmental Engineering, **130**, 636-645.

Salvador, A., 1991, Decade of North American Geology, Gulf of Mexico Basin: The Geological Society of America.

Sen, M., 2012, Full Waveform Inversion: Continuing Education Courses, 82nd Annual International Meeting, SEG.

Sheriff, R. E., and L. P. Geldart, 1985, Exploration Seismology I: History, Theory, and Data Acquisition: Cambridge University Press.

Shoemaker, E. M., 1960, Penetration mechanics of high velocity meteorites, illustrated by Meteor crater, Arizona: 21st International Geological Congress, 418-434.

Shoemaker, E. M., 1987, Meteor Crater, Arizona: Geological Society of America Centennial Field Guide - Rocky Mountain Section, 399-404.

Shoemaker, E. M., and S. W. Kieffer, 1974, Guidebook to the geology of Meteor crater, Arizona: 37th Annual Meeting, Meteoritical Society, 66, Reprinted in 1988.

Simons, F. J., R. D. Van Der Hilst, J. P. Montagner, and A. Zielhuis, 2002, Multimode Rayleigh wave inversion for heterogeneity and azimuthal anisotropy of the Australian upper mantle: Geophysical Journal International, **151**, 738-754.

Socco, L. V., D. Boiero, S. Foti, and R. Wisén, 2009, Laterally constrained inversion of ground roll from seismic reflection records: Geophysics, **74**, no. 6, G35-G45.

Socco, L. V., S. Foti, and D. Boiero, 2010, Surface-wave analysis for building near-surface velocity models – Established approaches and new perspectives: Geophysics, **75**, no. 5, 75A83-75A102.

Stewart, R. S., 1983, Vertical seismic profiling: The one-dimensional forward and inverse problems: Ph. D. thesis, Massachusetts Institute of Technology.

Stewart, R. R., N. Dyaur, B. Omoboya, J. J. S. de Figueiredo, M. Willis, and S. Sil, 2013, Physical modeling of anisotropic domains: Ultrasonic imaging of laser-etched fractures in glass: Geophysics, **78**, D11-D19.

Stokoe II, K. H. and S. Nazarian, 1983, Effectiveness of ground improvement from spectral analysis of surface waves: 8th Euro. Conf. on Soil Mech. and Found. Engin. Proceedings.

Strobbia, C., 2003, Surface wave methods: Acquisition, processing and inversion: Ph. D. thesis, Politec-nico di Torino, Italy.

Turolski, A., 2013, Near-surface geophysical imaging of complex structures: Meteor Crater, AZ and Jemez Pueblo, NM: M. S. thesis, University of Houston.

U.S. Energy Information Administration (EIA), updated May 9, 2011, http://www.eia.gov/

USGS, http://astrogeology.usgs.gov/site/map

Virieux, J., and S. Operto, 2009, An overview of full-waveform inversion in exploration geophysics: Geophysics, **74**, no. 6, WCC1-WCC26.

Wisén, R., D. Boiero, M. Maraschini, and L. V. Socco, 2010, Shear wave velocity model from surface wave analysis-a field case example: 72nd Conference and Exhibition, EAGE, Extended Abstracts, M045.

Wyllie, M. R. J., A. R. Gregory, and W. Gardner, 1956, Elastic wave velocities in heterogeneous and porous media: Geophysics, **21**, 41-70.

Xia, J., R. D. Miller, and C. B. Park, 1999, Estimation of near-surface shear-wave velocity by inversion of Rayleigh waves: Geophysics, **6**4, 691–700, doi:10.1190/1.1444578.

Xia, J., R. D. Miller, C. B. Park, and J. Ivanov, 2001, Feasibility of determining *Q* of near-surface materials from Rayleigh waves: 71st Annual International Meeting, SEG, Expanded Abstracts, 1381-1384.

Xia, J., R. D. Miller, C. B. Park, and G. Tian, 2003, Inversion of high frequency surface waves with fundamental and higher modes: Journal of Applied Geophysics, **52,** 45-57.